Wrinkling and Sagging of Viscous Sheets

by

Jeremy Alan Teichman

B.S. Mechanical Engineering and Computer Science
Yale University, 1996
S.M. Mechanical Engineering
Massachusetts Institute of Technology, 1998

Submitted to the Department of Mechanical Engineering
in partial fulfillment of the requirements for the degree of

Doctor of Philosophy in Mechanical Engineering

at the

MASSACHUSETTS INSTITUTE OF TECHNOLOGY

June 2002

Author .....
Department of Mechanical Engineering
May 20, 2002

Certified by .....
L. Mahadevan
Associate Professor of Mechanical Engineering
Thesis Supervisor

Accepted by .....
Ain Sonin
Professor of Mechanical Engineering
Graduate Officer

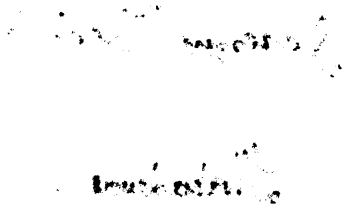

Wrinkling and Sagging of Viscous Sheets

by

Jeremy Alan Teichman

Submitted to the Department of Mechanical Engineering
on May 20, 2002, in partial fulfillment of the
requirements for the degree of
Doctor of Philosophy in Mechanical Engineering

Abstract

This thesis explores the wrinkling and sagging behavior of thin viscous Newtonian sheets and filaments motivated by analogous scenarios in elasticity. These problems involve dynamic free boundaries and geometric nonlinearities but use simple physics. The first problem examined concerns an annular viscous sheet subjected to torsional shearing which consequently develops spiral wrinkles. Examination of the behavior of this system leads to a scaling of the Stokes equations for zero Reynolds number flow resulting in a reduced order mathematical model for the evolution of the sheet that includes the effects of gravity and surface tension. Linear stability analysis yields the most unstable modes for wrinkling of the sheet and their associated growth rates at onset which agree with experimental observations. In the limit of a narrow annular gap, the problem reduces to that of a sheared rectilinear sheet. Interestingly, this Couette problem shows instabilities even in the zero Reynolds number limit.

The second problem examined concerns the sagging of a horizontal viscida (fluid filament) under the influence of gravity. Resistance of the viscida to bending controls the initial phase of deformation, while resistance to stretching begins to play a principal role in later stages. At very late times the process resembles droplet break-off from two thin filaments.

Thesis Supervisor: L. Mahadevan
Title: Associate Professor of Mechanical Engineering

Acknowledgments

My gratitude goes to Professor Gareth McKinley for providing me with laboratory and office space, funding, the apparatus and other equipment for my experiments, and for all of his time, helpful advice, and guidance as well as for serving on my committee and as an advisor. Many thanks to S. Chaieb for designing the experimental apparatus and to S. Chaieb and M. Carnascialli for preliminary experiments that preceded this study. Thanks also to Professors John Bush and C.C. Mei for helpful discussions and input on this endeavor and for serving on my thesis committee, and to Professor John Bush in particular for his careful editing of this document. Most especially, thanks to Professor L. Mahadevan for taking me on as a student, for guiding me, teaching me, advising me, debating me, arguing with me, and helping me.

Many people outside of my direct research advisors and collaborators deserve mention. First, I would like to thank my former advisor Professor Tony Patera for advising me during the first year of my Ph.D. and for ensuring that I remained on the right path. My colleagues have endured lengthy explanations of my various research difficulties, sometimes when all I really needed was to tell my idea to someone else to help me figure it out myself. They have given me encouragement and good camaraderie over the years and made my time in the Fluid Mechanics Laboratory a fun and memorable experience. For that and for their friendship, my gratitude goes especially to Darryl Overby, Jonathan Rothstein, Pirouz Kavehpour, Chris Hartemink, Carlos Hidrovo, and Karen Bottom. Thanks to Mark Bathe for helping me with ADINA.

Thank you to my close friends and roommates, Peter Sperber, David Matsa, Michael Kress, Cory Welt, Christian Brebbia, Raphi Schorr, Mike Rader, Michael Merdinger, Meyer Potashman, Adam Szpiro, Naomi Korn, Becky Malamud, Michele Harris, Wendy Smith, Jo Ilfeld, Melissa Lerman, Stephanie Cooper, and Leesa Eichner, who have listened to me complain, patiently listened while I tried to explain my work, shared in my excitement when things went well, and believed in me and encouraged me during more trying times. Thank you to my mother and father for always supporting me and rooting for me, for their steadfast enthusiasm and faith in me. A special thanks to Leah Friedman for making this last year of traveling to England, finishing up, and writing my thesis, which would otherwise have been a very lonely time, bearable and even fun.

In addition to my family and friends who have helped me through the years, I have been extremely fortunate to have had a number of wonderful teachers and mentors who have inspired and encouraged me and excited me about learning. I would like to particularly thank Thelma Farber, Helen Raucher, J.R. LeBlanc, Robert Ledbetter, Malcolm Boshier, Frederick Beiser, Leslie Smith, Terry Hesse, Jay Pastine, and Jules Enig.

In pursuing this thesis, J. Teichman was supported by a National Science Foundation Graduate Fellowship and by a grant from the Office of Naval Research. This material is based upon work supported under a National Science Foundation Graduate Research Fellowship. Any opinions, findings, conclusions or recommendations expressed in this publication are those of the author and do not necessarily reflect the views of the National Science Foundation.

Contents

List of Figures

List of Tables

List of Symbols

x,y,z	Fixed Cartesian coordinates
$\hat{x}$,$\hat{y}$,$\hat{z}$	Dimensionless fixed Cartesian coordinates
r,θ	Cylindrical polar coordinates
ξ	Transformed r coordinate
x',y',z'	Non-orthogonal curvilinear coordinate directions
$\vec{x}'$,$\vec{y}'$,$\vec{z}'$	Non-orthogonal curvilinear unit vectors
t	Time
$\hat{t}$	Dimensionless time
s	Lagrangian arc-length coordinate
$\bar{s}$	Eulerian arc-length coordinate
H	Center surface displacement
h	Sheet thickness
u	x-component of velocity or depth-averaged r-component of velocity
$\bar{u}$	Depth-averaged x-component of velocity
v	y-component of velocity or depth-averaged θ-component of velocity
$\bar{v}$	Depth-averaged y-component of velocity
w	z-component of velocity
$\vec{u}$	Velocity vector (u, v, w)
$\hat{u}$,$\hat{v}$,$\hat{w}$	Dimensionless Cartesian velocity components
P	Pressure
$\hat{P}$	Dimensionless pressure
$\underline{\underline{I}}$	Second order isotropic tensor
$\underline{\underline{\sigma}}$	Stress tensor with components σ_{ij}
T_{11}	Depth-integrated σ_{11}
T_{12}	Depth-integrated σ_{12}
T_{22}	Depth-integrated σ_{22}
Q_x	Depth-integrated σ_{13}
Q_y	Depth-integrated σ_{23}
$\dot{\gamma}$	Shear strain rate
μ	Shear viscosity
Re	Reynolds number
γ^+,γ^-	Surface tension on upper and lower sheet surfaces
γ_W	Water-air surface tension
γ_W^d	Portion of water-air surface tension generated by dispersion forces
γ_H	Hydrocarbon-air surface tension
γ_{WH}	Water-hydrocarbon interfacial surface tension
κ	Mean curvature
ρ	Density
g	Acceleration due to gravity
U	Characteristic velocity scale or shear velocity
L	Characteristic length scale or viscida length
ϵ	Slenderness ratio h/L

B	Half-width
D	Bending stiffness
Γ	Dimensionless surface tension parameter
G	Dimensionless gravity parameter or shear modulus in elastic equations
G_2	Dimensionless gravity to dimensionless growth rate ratio
Γ_2	Dimensionless surface tension to dimensionless growth rate ratio
E	Young's modulus
ν	Poisson's ratio
$\vec{T}$	Traction
$\vec{n}$	Outward unit normal
R_i	Inner radius
R_o	Outer radius
n	Aspect ratio
m	Azimuthal wavenumber
k	x-direction (length-wise) wavenumber
λ	y or r direction (width-wise) wavenumber or stretch
σ	Growth rate
S	Shear force per unit length or shear strain rate to growth rate ratio
f	Mode shape
A	Shear strain rate or area
w	Weight per unit length
θ	Angle of inclination
T	Tension
N	Shear force
ξ, η	Principal axes coordinates
β	Tension line angle

Chapter 1

Introduction

Most of us typically associate buckling phenomena such as folding, wrinkling, and coiling with solid media. It comes as no surprise then that such behavior has been observed in elastic fluids. However, it has long been known that similar geometric wonders can also be found in the world of Newtonian viscous fluids. One need look no further than the kitchen to watch the beautifully regular ribbon folding of batter pouring into a pan or honey coiling onto a piece of toast. For those less inclined to culinary pursuits, many shampoos fold nicely when squeezed into the palm.

Instabilities associated with slender members such as thin films and filaments fall under two main classifications. In the first, sinuous, also known as anti-symmetric, folding, or buckling, the two opposite surfaces of the member move in unison following the center line or center surface of the member. In the second, varicose, also known as symmetric or pinch-and-swell, the resulting structure resembles a string of sausages with alternating thinner and thicker regions, and the two opposite surfaces move in mirror images of one another while the center line or center surface experiences no displacement. Figure 1-1 illustrates an example of each type of instability. Surface tension often drives the formation of varicose instabilities, and varicose instabilities are therefore principally associated with fluids rather than solids. This thesis focuses on the formation of sinuous type structures in viscous Newtonian fluids and the interaction or competition between bending and stretching that gives rise to them.

Fluid buckling phenomena are not confined to the realm of novelties and have drawn a considerable amount of scientific attention. In materials processing, many

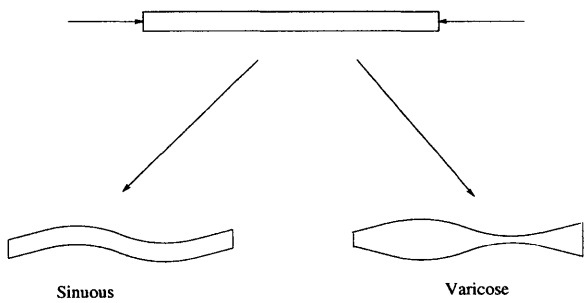

Figure 1-1: Two modes of slender member instability

of the processes involve highly viscous filaments, films, and sheets manipulated in a wide variety of ways from spinning of fibers to manufacture of transparency films and plastic bags. An understanding of the instabilities present in these configurations and how to avoid or harness them is highly desirable. In geophysics, rock folding is often explained using mechanisms of viscous folding on very long time scales. Much work has been done on rock folding in two dimensions, but folding in three dimensions has not been equally well explored [14]. The reduced dimension equations shown here could help explain many of the rock folding phenomena exhibiting variations in three dimensions. Additional applications exist in manufacturing processes involving sheets and films of molten glass, metal, plastic, food etc. Of course, in these cases the presence of phase change or temperature variation complicates matters because viscosity may acquire spatial variation.

The existence in fluids of what are thought of as primarily elastic behaviors comes as no surprise; in fact, one ought to expect it. James Clerk Maxwell [19] wrote,

> What is required to alter the form of a soft solid is a sufficient force and this, when applied, produces its effect at once. In the case of a viscous fluid it is 'time' which is required, and if enough time is given, the very smallest force will produce a sensible effect.

Following the ideas of Stokes, Lord Rayleigh, in The Theory of Sound, established a formal analogy between the behaviors of a bulk elastic medium and a bulk Newtonian viscous medium [29]. He demonstrated that the expression for the volumetric energy dissipation rate in a fluid differs from the expression for the energy density in an elastic solid only by a time derivative. The governing equations for the two media should, thus, be of the same form with the exception of an additional time derivative in the viscous medium (see Table 1.1). Though Lord Rayleigh's analogy concerned behavior

Static Elasticity	**Low Reynolds Number Flows**
Displacement	Velocity
Strain	Strain Rate
Shear and Bulk Modulus	Shear and Bulk Viscosity

Table 1.1: Stokes-Rayleigh Analogy

in the bulk, his results should extend to the slender geometries of thin films with little modification. The primary difference between a bulk medium and a slender geometry lies in the presence of free surfaces which introduce surface tension forces into the problem. For high capillary number scenarios where viscous forces dominate surface tension forces, the analogy should hold very closely. In the spirit of the analogy, this thesis examines three viscous problems with close elastic analogs.

The first such problem is that of an annular sheet subjected to shearing in its plane and the consequent evolution of spiral wrinkles in the sheet (Figure 1-2). If an annular viscous film floating upon a relatively inviscid fluid is sheared by rotating the inner cylinder of the annulus, at low shear rates, the film remains flat. However, when the angular velocity of the inner cylinder is increased beyond a critical value, spiral

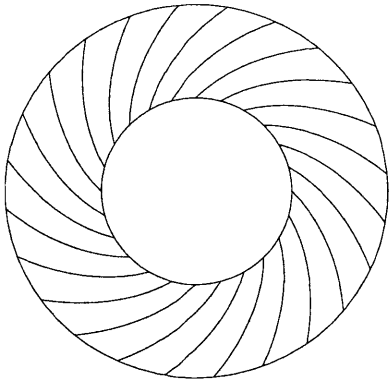

Figure 1-2: Sheared annular sheet

wrinkles develop in the film. The wavelength of these wrinkles is large compared to the thickness of the film. The number of wrinkles depends on the geometry of the annulus as does the angular velocity of the inner cylinder necessary to provoke the wrinkling. In 1924, W.R. Dean explored elastic instabilities of a sheared annular plate [11]. By formulating and analyzing the governing equations of the plate, Dean calculated the shape assumed by the plate when subjected to shear forces on its edges exceeding some critical buckling load. In doing so, he calculated the shear load necessary to cause deformations with different azimuthal wavenumbers as a function of the geometry of the annulus as characterized by the ratio of outer to inner radius. As he argued, for a given geometry, the only important distortion of the plate is the one that results under the minimum external loading. His results characterize the dependence of the various possible plate distortions upon geometry and shear loading.

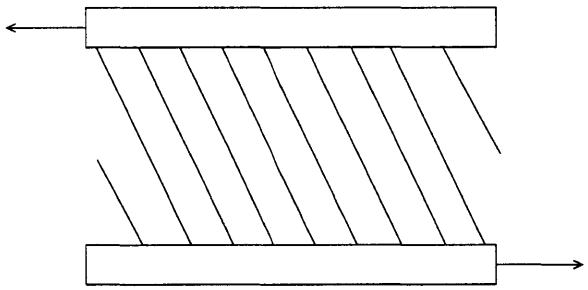

Figure 1-3: Sheared rectilinear sheet

The second problem can be thought of as a limiting case of the first. Consider a Couette geometry in which a thin film of finite width and infinite length is sheared by the two width-wise bounding walls (Figure 1-3 shows one section of such a scenario). This represents the limit of the annular case as the radius of the annulus approaches infinity while the gap remains constant. The sheared sheet will develop wrinkles as illustrated in the sketch. Southwell and Skan investigated the instabilities of a sheared elastic strip in 1924 and calculated the conditions for and modes of deformation [28].

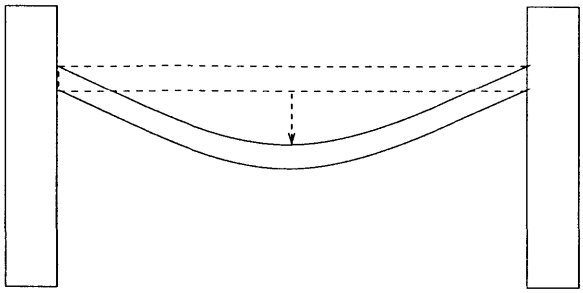

Figure 1-4: Viscous catenary

The third problem is the viscous catenary. If a viscous filament (viscida) spans the gap between two solid wall and sags under its own weight (Figure 1-4), it will form a viscous catenary, the viscous analog of an elastic filament hanging freely from its two endpoints. The original catenary problem concerned an inextensible chain hanging from its two endpoints and was solved by Leibniz, Huygens, and Johann Bernoulli in 1691 [20]. Love considered the elastic catenary problem including bending and stretching stiffnesses of the filament [17].

1.1 Prior studies

1.1.1 General viscous buckling

Viscous (Newtonian) buckling has been studied in various contexts over the last half century. In the early part of the twentieth century, geologists examined the possibility of modeling certain behaviors of the earth's crust as elastic buckling phenomena in work attributed to Smoluchowski [21]. By the late 1950s, geologists considered that viscous buckling could present a better model. Typical viscosities of the rocks involved in geological analysis range from about $10^{16} - 10^{21} Pa \cdot s$ [6]. Biot examined the two-dimensional folding of a viscous layer embedded in a less viscous medium and subjected to layer-parallel compression. Biot utilized a similarity between elastic and viscous governing equations to develop expressions for the critical load and wavelength of the instability for a variety of combinations of types of media including viscous, elastic, and viscoelastic. For a viscous fluid, he found that the critical load necessary to excite the buckling is zero, the wavelength of buckling normalized by the layer thickness is proportional to the cube root of the ratio of the layer viscosity to the ambient viscosity, and the wavelength of buckling does not depend on the magnitude of loading [4]. Biot's results would suggest that as the ambient viscosity becomes negligible compared to the layer viscosity, the most unstable wavelength will grow longer without bound. The system size would, of course, limit the wavelength, so that in a two-dimensional case of layer-parallel compression of a viscous film on a comparatively inviscid substrate, Biot's results predict buckling with a wavelength equal to twice the system size. In 1963, Ramberg proposed that the appropriate boundary condition for the interface between the layer and the ambient medium should be a welded condition rather than the free-slip condition used by Biot, thus

incorporating the effects of layer-parallel shear. The resulting model predicts shorter wavelength folds than does Biot's model, but in the limit of comparatively vanishing ambient viscosity, it also predicts a wavelength equal to twice the system span [21]. In 1959, Biot examined the effects of gravity producing a buoyant force in opposition to buckling of a viscous layer floating atop a less viscous and more dense substrate and subjected to layer-parallel compression. He found that the influence of gravity produces a dependence of the buckling wavelength on the applied compressive stress so that a finite wavelength exists for the maximally growing mode even as the viscosity of the substrate tends to zero [5]. Ramberg and Stephansson, in 1964, also examined the effects of gravity in this scenario. They found that gravity produces a non-zero critical stress required to buckle the layer faster than the concomitant thickening effect. At stresses below the critical threshold for buckling, layer thickening occurs on a faster time scale than folding. Their results argued against Newtonian viscous buckling as a mechanism for the formation of large crustal depressions [22]. In 1968, Chapple analytically and computationally explored the effects of finite fold amplitude on the buckling of a viscous layer and suggested that wavelength selection only occurs at small amplitude after which the mode of buckling does not change. He then explored the shape evolution of the finite amplitude folds [9]. Also in 1968, Sherwin and Chapple performed experimental studies to verify Biot's folding theory. They developed a modified theory for scenarios with small viscosity ratios where shortening of the layer plays a key role in addition to folding [25]. Johnson and Fletcher's 1994 monograph on viscous buckling outlines a wide range of problems considered in geology and geophysics [14].

In 1969, G.I. Taylor made a series of observations and comments on the buckling of viscous filaments and sheets [30]. In the 1970s, Buckmaster, Nachman, and Ting explored the buckling of a viscida (a viscous filament) from a mathematical perspective and looked at what effects might play important roles and how the various effects and properties scaled [8] [7]. In 1988, Benjamin and Mullin attempted to explain some of Taylor's experiments by examining short wavelength instabilities in the shearing of a viscous sheet [3]. In 1987, Bejan published a review article on buckling flows focusing primarily on instabilities where inertia plays an initiating role [2]. In 1996, Howell, building on scaling arguments made by Buckmaster, Nachman, and Ting, developed a series of equations describing the evolution of a buckling sheet of viscous Newtonian fluid [12]. In the last few years, a number of particular viscous buckling phenomena have been explained. In 1997, Tuck, Stokes, and Schwartz examined the slumping of a viscous bridge similar to the catenary problem considered here. They considered the very short time behavior of the bridge and used finite elements to study its subsequent evolution. In 1998, Mahadevan, Samuel, and Ryu looked at the coiling of a viscous filament impinging on a flat surface under the influence of gravity [18]. In 2000, Skorobogatiy and Mahadevan examined the analogous problem of the folding of a viscous sheet impinging on a flat surface under the influence of gravity [27]. Also in 2000, da Silveira, Chaieb, and Mahadevan investigated the wrinkling of a ruptured viscous bubble collapsing under its own weight [26]. In 2000, Kumar and Graham examined the behavior of a non-Newtonian fluid sheet drawn radially inwards and wanted to understand the consequent crumpling of the sheet [15]. They make only

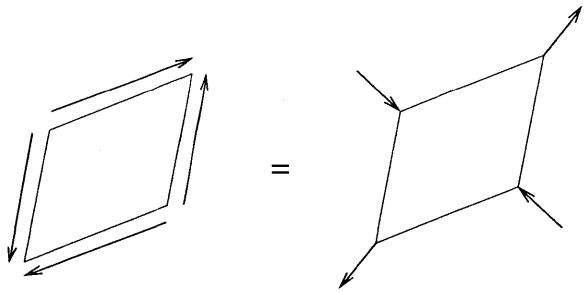

Figure 1-5: Equivalence of shear to tension plus compression

very brief reference to the Newtonian case. In 2001, Ribe carried out a formal reduction to derive asymptotic equations for sheets of high curvature and analyzed film blowing and a couple of other high curvature scenarios [24]. This brief history is by no means comprehensive, but is merely intended to provide an idea of the evolution and current interest in viscous buckling problems. The current study provides the first quantitative explanation of a truly two-dimensional buckling problem in viscous sheets.

1.1.2 Annular sheet buckling

G.I. Taylor, who presented Dean's 1924 paper and Biot's 1957 paper to the Royal Society, first documented a wrinkling effect similar to Dean's in a viscous annular sheet, though he made no reference to the elastic analogy or to Dean's or Biot's study [30]. Taylor floated a layer of golden syrup a few centimeters thick on top of carbon tetrachloride in a cylindrical container with a cylindrical stirring rod placed from above into the center of the container. Taylor noted that when the stirring rod rotated about its axis, spiral ripples appeared on the syrup's surface radiating outward from the rotating rod. Taylor declared that this effect was most likely related to buckling because the wrinkling initiated across lines of maximum compressive stresses (The layer was subjected to pure shear, but pure shear is equivalent to a combination of tension and compression at right angles to one another along a set of directions rotated forty-five degrees relative to the direction of shearing as shown in Figure 1-5.). He did not offer a quantitative explanation. In 1988, Benjamin and Mullin further examined the instability observed by Taylor and quantitatively analyzed the instability for the case of a rectangular geometry in which the shear strain rate is uniform across the fluid sheet [3]. The effect observed by Taylor and examined by Benjamin and Mullin concerned ripples with azimuthal wavelengths shorter than the thickness of the sheet and thus differed from that explored by Dean. Dean examined distortions with azimuthal wave lengths much longer than the thickness of the plate. Also, Benjamin and Mullin ignored the effects of shear strain rate variation over the annular gap width, thus effectively converting it into a rectilinear geometry. In 1999, following a suggestion by L. Mahadevan, Chaieb and Carnascialli performed some preliminary qualitative experiments depicted in Figure 1-6 that suggested that there is indeed a long wavelength analog of the Dean problem for a thin viscous sheet.

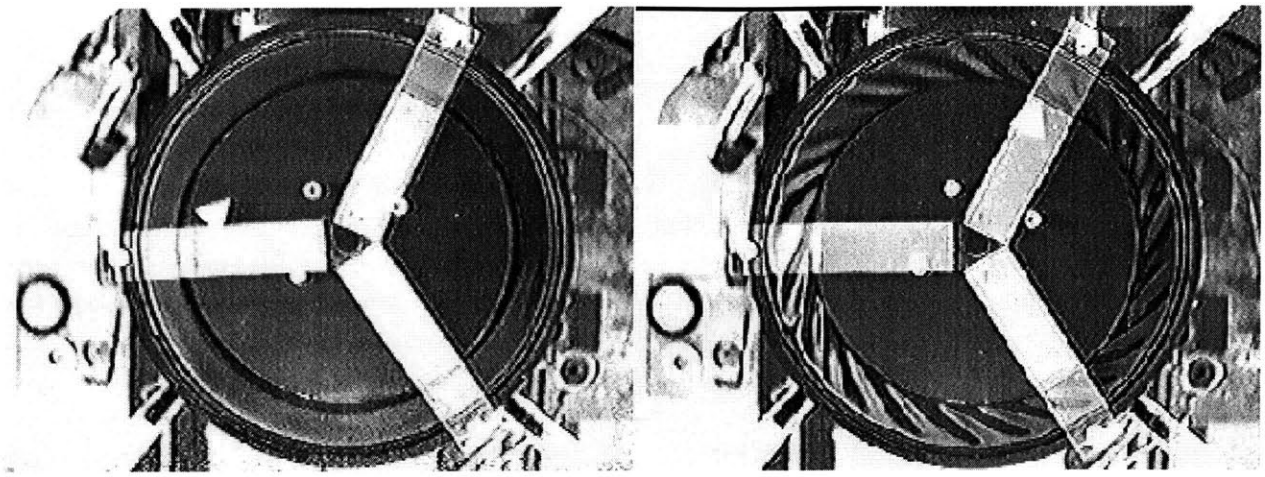

Figure 1-6: Viscous experiment analogous to Dean's: In the figure on the left, the inner cylinder is rotating counter-clockwise at less than the critical angular velocity, Ω_C, so the surface is undisturbed. In the figure on the right, the inner cylinder is rotating faster than the critical angular velocity, and the viscous layer wrinkles in a very regular fashion. The fluid shown is a variety of polybutene with a viscosity $\sim 140 Pa \cdot s$; the diameter of the inner cylinder is $\sim 10cm$; the gap width is $\sim 2cm$; and the rate of rotation is $\sim 0.5 rad/s$.

This thesis concerns an experimental, analytical, and numerical investigation of this instability and some related problems.

Chapter 2

Equations of motion: a physical derivation

This chapter describes the development of a series of reduced order equations describing the evolution of a thin sheet of an incompressible Newtonian fluid. The equations are derived from the Stokes equations for highly viscous flow using a scaling suggested by Buckmaster et al. [8] and partially following the method used by Howell [12] to derive a similar set of equations without gravity or surface tension which are accounted for in the model presented here. An abbreviated version of the derivation is presented here; for the full derivation, please see Appendix A. Once developed, the equations are physically interpreted and compared to the analogous Föppl-von Kármán equations from elasticity. Finally, I briefly explore the linear stability characteristics of the evolution equations for a simple case in order to set the stage for further discussion of more complicated scenarios in the chapters that follow.

2.1 Basic equations

Let us consider a thin sheet of an incompressible Newtonian fluid with a very large viscosity floating atop a fluid of higher density and comparatively vanishingly small viscosity and being sheared such that the Reynolds number, $\frac{\rho UL}{\mu} << 1$. The Stokes equations describe the behavior of such a fluid (here in Cartesian coordinates):

$$\nabla P = \mu \nabla^2 \vec{u}, \tag{2.1}$$

where P is the pressure, and $\vec{u}$ is the velocity vector, (u, v, w). The continuity equation ensures conservation of mass:

$$\nabla \cdot \vec{u} = 0. \tag{2.2}$$

The top and bottom of the sheet must obey a kinematic surface condition,

$$w|_{z=H\pm\frac{1}{2}h} = \frac{D}{Dt}(H \pm \frac{1}{2}h), \tag{2.3}$$

where H is the z-coordinate of the center surface of the sheet, and h is the thickness of the sheet. The top and bottom surfaces must also satisfy a dynamic traction condition. Tractions on the surfaces of the layer result from ambient pressure and surface tension of the interfaces. The ambient pressure in the air above the fluid sheet can, without loss of generality, be considered zero. The ambient pressure below will be determined by hydrostatic pressure variations in the underlying fluid, $P^- = \rho^- gH$, where ρ^- is the density of the underlying fluid and g is acceleration due to gravity. Because of the extremely high viscosity ratio (in the cases considered here, $\mu/\mu^- \sim 10^5$), viscous forces in the underlying fluid can be considered negligible. The free surface condition can be expressed as

$$\underline{\underline{\sigma}} \cdot \vec{n} = \vec{T}, \tag{2.4}$$

where $\underline{\underline{\sigma}}$ is the stress tensor,

$$\underline{\underline{\sigma}} = -P\underline{\underline{I}} + \mu(\nabla\vec{u}^T + \nabla\vec{u}), \tag{2.5}$$

$\vec{n}$ is the unit outward normal to the surface,

$$\vec{n} = [-(H_x \pm \frac{1}{2}h_x), -(H_y \pm \frac{1}{2}h_y), 1]^T, \tag{2.6}$$

$\vec{T}$ is the traction on the surface, and $\underline{\underline{I}}$ is the isotropic tensor. The lateral edges of the sheet satisfy a no-slip condition so that the velocity $\vec{u}$ matches the velocity of the walls.

One could question whether or not inertial forces in the underlying fluid could affect the viscous sheet. Characteristic inertial pressures in the underlying fluid scale as $\rho^- U^2$. Characteristic stresses generated within the viscous sheet scale as $\mu U/L$. Since the characteristic velocities in the two fluids are of the same order, their ratio is a Reynolds number based on the underlying fluid's density and the sheet's viscosity, $Re = \rho^- UL/\mu$. For characteristic values of the parameters considered here ($\mu \sim 10^2 Pa \cdot s$, $L \sim 10^{-2}m$, $\rho^- \sim 10^3 kg/m^3$, $U \sim 10^{-2}m/s$), $Re \sim 10^{-3}$, so inertial forces in the underlying fluid should not play a role in the sheet's behavior. One could also question whether capillary-gravity waves generated by the ripples could affect the behavior of the sheet. If such a wave dissipates almost entirely over a length scale much smaller than the wavelength of the ripples, it will have a negligible effect on the behavior of the sheet. The quotient of the Reynolds number and the square-root of the Froude number, $Fr \equiv U^2/gL$, provides a rough approximation of the attenuation factor per wavelength travel [16]. For the characteristic values of the parameters considered here, $Re/\sqrt{Fr} < 10^{-1}$, so the effects of capillary-gravity waves can safely be neglected.

2.2 Asymptotic scaling

Following Buckmaster, Nachman, and Ting[8], we can scale the variables in the equation in a manner consistent with buckling type motion to generate an equation wherein all of the scaled variables are of the same order. The scaled variables are indicated by hats, and the scaling utilizes a characteristic in-plane length-scale of the sheet, L, a characteristic out-of-plane velocity, U, and a slenderness ratio, ϵ, characterizing the ratio of the thickness of the sheet to L, where $\epsilon << 1$. The variables scale as follows:

$$\begin{array}{llll} x = \hat{x}L, & y = \hat{y}L, & z = \hat{z}\epsilon L, & P = \hat{P}\mu\epsilon\frac{U}{L}, \\ u = \hat{u}\epsilon U, & v = \hat{v}\epsilon U, & w = \hat{w}U, & t = \hat{t}\epsilon\frac{L}{U}, \\ H = \hat{H}\epsilon L, & h = \hat{h}\epsilon L. & & \end{array} \tag{2.7}$$

This scaling should be contrasted with the scaling of lubrication theory typically employed in a slender geometry. In lubrication theory, motion perpendicular to the sheet is slower than motion in the plane of the sheet by an order of ϵ. In buckling type motion, for displacements of the order of the thickness of the sheet, motion within the plane of the sheet is an order of ϵ slower than motion perpendicular to the sheet.

Howell [12] demonstrated that by plugging these scaled variables into the governing equations and representing the scaled variables in perturbation series (e.g. $\hat{u} = \hat{u}^{(0)} + \epsilon^2\hat{u}^{(1)} + \epsilon^4\hat{u}^{(2)} \cdots$) the equations could be solved order by order to generate a set of equations describing the evolution of the geometry of the sheet. This chapter demonstrates that the final equations arrived at by Howell can be derived in a more physically intuitive manner by solving the leading order equations and balancing forces and moments in the sheet. Ribe [24] illustrates a similar physically motivated derivation for one-dimensional, initially curved sheets.

2.3 Asymptotics

Since all variables now considered are scaled, the hat notation will be dropped for convenience. Employing the scaling in the governing equations and boundary conditions and solving for the leading order values of the field variables leads to the following (see Appendix A):

$$h_t = 0, \tag{2.8}$$

i.e. there is no varicose (symmetric) distortion of the sheet, and the thickness remains constant everywhere. As a consequence,

$$w(x, y, t) = H_t, \tag{2.9}$$

the fluid velocity perpendicular to the sheet everywhere follows the local center surface. It immediately follows that

$$u = \overline{u} + (H - z)H_{tx}, \tag{2.10}$$

$$v = \overline{v} + (H - z)H_{ty}, \tag{2.11}$$

where $\overline{u}$ and $\overline{v}$ are the depth-averaged in-plane velocities.

$$P = -2(u_x + v_y). \tag{2.12}$$

2.4 Depth-averaged equilibrium

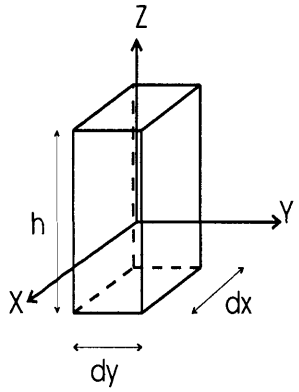

Figure 2-1: Unit fluid element

Now the leading order balances of forces and balances of moments on a small element of the sheet (see Figure 2-1) relate the leading order quantities in a series of reduced order governing equations for the evolution of the sheet:

$$T_{11} \equiv 4(\overline{u}_x + H_x H_{tx})h + 2(\overline{v}_y + H_y H_{ty})h \tag{2.13}$$

$$T_{12} \equiv (\overline{u}_y + H_y H_{tx})h + (\overline{v}_x + H_x H_{ty})h \tag{2.14}$$

$$T_{22} \equiv 4(\overline{v}_y + H_y H_{ty})h + 2(\overline{u}_x + H_x H_{tx})h \tag{2.15}$$

$$\frac{\partial T_{11}}{\partial x} + \frac{\partial T_{12}}{\partial y} = 0 \tag{2.16}$$

$$\frac{\partial T_{12}}{\partial x} + \frac{\partial T_{22}}{\partial y} = 0 \tag{2.17}$$

$$H_{xx}T_{11} + 2H_{xy}T_{12} + H_{yy}T_{22} - \frac{GH}{3\epsilon^2} + \frac{\Gamma}{3\epsilon^2}\nabla^2 H = \frac{1}{3}h^3\nabla^4 H_t, \tag{2.18}$$

where

$$G \equiv 3\frac{\rho^- g L^2}{\mu U}, \tag{2.19}$$

$$\Gamma \equiv 3\frac{\gamma^+ + \gamma^-}{\mu U}, \tag{2.20}$$

and $\gamma^{\pm}$ is the surface tension at the upper/lower interface. For the experiments discussed in Chapter 3, characteristic values are $G \sim 10^{-1}$ and $\Gamma \sim 10^{-2}$ for $\rho \sim 10^3 kg/m^3$, $L \sim 10^{-2}m$, $\mu \sim 10^2 Pa{\cdot}s$, $U \sim 10^{-1}m/s$, and $(\gamma^+ + \gamma^-) \sim 10^{-1}N/m$. T_{11}, T_{22}, and T_{12} refer to the depth-integrated normal stresses in the x and y directions

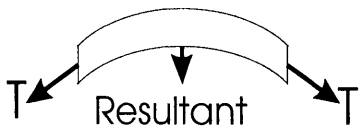

Figure 2-2: Out-of-plane load due to tension

and the depth-integrated shear stress respectively. The Laplacian and biharmonic operators are strictly planar, $\nabla^2 \equiv \frac{\partial^2}{\partial x^2} + \frac{\partial^2}{\partial y^2}$ and $\nabla^4 \equiv \frac{\partial^4}{\partial x^4} + 2\frac{\partial^4}{\partial x^2 \partial y^2} + \frac{\partial^4}{\partial y^4}$. (2.16) and (2.17) express force equilibrium in the x and y directions respectively, and (2.18) expresses force equilibrium in the z-direction. In dimensional form,

$$T_{11} \equiv 4\mu(\overline{u}_x + H_x H_{tx})h + 2\mu(\overline{v}_y + H_y H_{ty})h, \tag{2.21}$$

$$T_{12} \equiv \mu(\overline{u}_y + H_y H_{tx})h + \mu(\overline{v}_x + H_x H_{ty})h, \tag{2.22}$$

$$T_{22} \equiv 4\mu(\overline{v}_y + H_y H_{ty})h + 2\mu(\overline{u}_x + H_x H_{tx})h, \tag{2.23}$$

(2.16) and (2.17) remain unchanged, and

$$H_{xx}T_{11} + 2H_{xy}T_{12} + H_{yy}T_{22} - \rho g H + (\gamma^+ + \gamma^-)\nabla^2 H = \frac{1}{3}\mu h^3 \nabla^4 H_t. \tag{2.24}$$

To summarize, the first three terms on the left hand side of (2.18) (e.g. $H_{xx}T_{11}$) represent contributions to out-of-plane motion from in-plane stresses as illustrated in Figure 2-2. These terms provide both driving and mitigating forces for deformation; the compressive stresses drive the buckling, while the tensile stresses oppose it. The portions of these terms linear in H (e.g. $4\bar{u}_x h H_{xx}$) represent stress contributions due to gradients in the in-plane velocity field; the nonlinear portions (e.g. $4hH_x H_{tx} H_{xx}$) represent the effects of stretching of the sheet. The right hand side expresses the bending response ($\nabla^4 H_t$) with a resistance proportional to the rate of change of curvature. The gravity term (GH) tends to damp out all wavelength deformations of the sheet; however, its relative magnitude is larger for long wavelength modes. The surface tension term ($\Gamma\nabla^2 H$), which is proportional to the mean curvature of the sheet, also acts to damp out all wavelength modes and most strongly affects those with the highest curvature.

2.5 Elastic analogy

For comparison, let us examine the equation utilized by Dean to describe the out-of-plane displacement of an elastic plate:

$$D\nabla^4 H - \frac{\partial}{\partial x}\left(T_{11}\frac{\partial H}{\partial x}\right) - \frac{\partial}{\partial y}\left(T_{22}\frac{\partial H}{\partial y}\right) - \frac{\partial}{\partial x}\left(T_{12}\frac{\partial H}{\partial y}\right) - \frac{\partial}{\partial y}\left(T_{12}\frac{\partial H}{\partial x}\right) = 0, \tag{2.25}$$

where D is the torsional rigidity of the plate, and the variables from this thesis replace Dean's equivalent variables. Timoshenko provides an expression for D [31],

$$D \equiv \frac{Eh^3}{12(1-\nu^2)}, \tag{2.26}$$

where E is the Young's Modulus of the material, and ν is the Poisson's Ratio of the material. For comparison to the incompressible viscous case, let us consider an incompressible solid, $\nu = 1/2$. Also, let us replace the Young's Modulus with the shear modulus of the elastic material [10],

$$G = \frac{E}{2(1+\nu)} = \frac{E}{3}. \tag{2.27}$$

(2.16) and (2.17) apply to the plate as well [31] and can be used to simplify (2.25) to

$$H_{xx}T_{11} + 2H_{xy}T_{12} + H_{yy}T_{22} = \frac{1}{3}Gh^3\nabla^4 H. \tag{2.28}$$

Dean does not present the in-plane equations and only reveals the linear terms in the in-plane stresses. The full equations for the in-plane stresses in the elastic case are given by the Föppl-von Kármán equations [17], presented here in the notation of this thesis,

$$\frac{\partial T_{11}}{\partial x} + \frac{\partial T_{12}}{\partial y} = 0 \tag{2.29}$$

$$\frac{\partial T_{12}}{\partial x} + \frac{\partial T_{22}}{\partial y} = 0 \tag{2.30}$$

where

$$T_{11} \equiv 4G(\overline{u}_x + \frac{1}{2}H_x^2)h + 2G(\overline{v}_y + \frac{1}{2}H_y^2)h \tag{2.31}$$

$$T_{12} \equiv G(\overline{u}_y + \frac{1}{2}H_yH_x)h + G(\overline{v}_x + \frac{1}{2}H_xH_y)h \tag{2.32}$$

$$T_{22} \equiv 4G(\overline{v}_y + \frac{1}{2}H_y^2)h + 2G(\overline{u}_x + \frac{1}{2}H_x^2)h. \tag{2.33}$$

In keeping with the Stokes-Rayleigh analogy, (2.28)-(2.30) are the exact equivalent of (2.16), (2.17), and (2.24).

2.6 Folding of a planar viscous sheet subjected to layer-parallel compression

In order to understand the stability behavior of a viscous sheet in the presence of gravity and surface tension, it is instructive to think about the planar case of a folding sheet with no variation in the y-direction where the folding results from a constant compressive force in the x-direction. Such a sheet obeys the following dimensionless

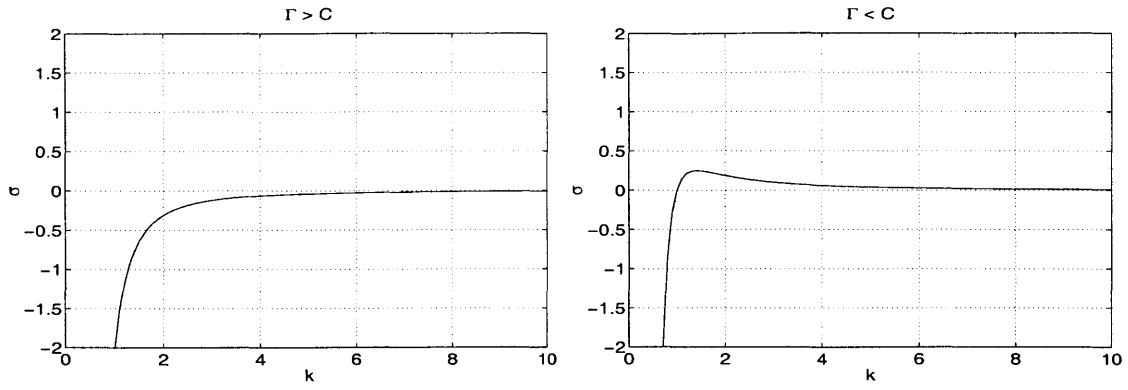

Figure 2-3: Characteristic dispersion relations for folding of a viscous sheet subjected to unidirectional compression, on the left for a stable sheet and on the right for an unstable sheet. The axis scales are arbitrary.

evolution equation:

$$H_{xxxxt} = (\Gamma - C)H_{xx} - GH, \tag{2.34}$$

where C characterizes the magnitude of the compressive stresses in the sheet. If the solution takes the form

$$H(x,t) = e^{\sigma t}\cos kx, \tag{2.35}$$

then

$$\sigma = \frac{C-\Gamma}{k^2} - \frac{G}{k^4}. \tag{2.36}$$

A mode will grow if $\sigma > 0$. For long enough waves (small k), gravity will always overpower the compression and surface tension to damp the waves. For short enough waves (large k), gravity does not affect the growth, and stability is strictly determined by the relative strengths of compression and surface tension. For $C < \Gamma$, the system is always stable because all modes are stable, but the decay rate approaches zero as k increases without bound. For $C > \Gamma$, the system is unstable because there are stable and unstable modes, and there is a maximally growing mode. At high wave numbers, the growth rates decay like $1/k^2$ for increasing k, and at low wave numbers, the growth rates decay like $-1/k^4$ for decreasing k. As C approaches Γ from above, the most unstable wavenumber increases without bound. However, since the governing equations were derived under the assumption that the wavelength is large compared to the thickness of the sheet, the previous conclusion is only valid when the predicted wavenumber is smaller than $2\pi/h$. The condition of marginal stability occurs when one mode is neutrally stable and all others are stable. The marginal stability conditions are degenerate in a respect because there is no set of parameters for which only one finite wavenumber is neutrally stable and all others are stable. Figure 2-3 shows the dispersion relation for the two cases. Increasing the relative strength of gravity increases the wavenumber of the maximally growing mode as does increasing the relative strength of surface tension.

In the absence of surface tension, this theory predicts that the most rapidly grow-

ing mode will have a dimensional wavenumber of

$$k = \sqrt{\frac{2\rho g}{Ph}}, \tag{2.37}$$

where P is the compressive stress in the sheet. This result matches exactly with Biot's results [5].

Chapter 3

Spiral wrinkling of a torsionally sheared viscous film

Let us now consider an annular sheet of an incompressible Newtonian fluid with a very large viscosity floating atop a fluid of higher density and comparatively vanishingly small viscosity and being sheared by rotation of the inner cylinder of the annulus (as illustrated in Figure 3-1) such that the Reynolds number of the flow around the annulus is vanishingly small. This is the analog of the Dean problem with the addition of gravitational and capillary forces (The case without gravity or surface tension is considered in Appendix C.). Here, linear stability analysis is employed to explore the susceptibility of the sheet to small perturbations from its planar form. In the real world, infinitesimal perturbations are always present, so the small amplitude analysis presented here will elucidate the stability behavior and early evolution of the sheet as it diverges from its initially planar form. In particular, linear stability analysis will reveal the minimum shear rate necessary to create an unstable state in the sheet as well as the rate and mode of departure into a deformed shape.

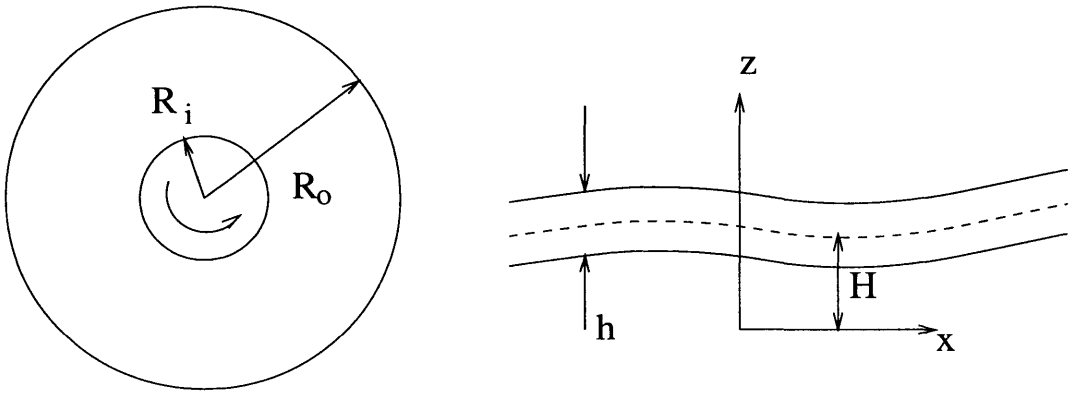

Figure 3-1: Schematic of scenario: plan view on left and partial section on right.

3.1 Linear stability

To examine the case of a sheared annular viscous sheet, let us write (2.16), (2.17), and (2.18) in cylindrical polar coordinates (r, θ, z), where u and v now represent the r and θ components of the depth-averaged in-plane velocity respectively:

$$4u_{rr} + \frac{3}{r}v_{r\theta} + \frac{1}{r^2}u_{\theta\theta} + \frac{4}{r}u_r - \frac{5}{r^2}v_\theta - \frac{4}{r^2}u + 4H_{tr}H_{rr} + \frac{2}{r}H_{tr}H_r + \frac{1}{r^2}H_{tr}H_{\theta\theta} - \frac{6}{r^3}H_{t\theta}H_\theta + \frac{3}{r^2}H_{t\theta}H_{r\theta} + 4H_{trr}H_r + \frac{3}{r^2}H_{tr\theta}H_\theta + \frac{1}{r^2}H_{t\theta\theta}H_r = 0, \quad (3.1)$$

$$v_{rr} + \frac{3}{r}u_{r\theta} + \frac{4}{r^2}v_{\theta\theta} + \frac{1}{r}v_r + \frac{5}{r^2}u_\theta - \frac{1}{r^2}v + \frac{1}{r^2}H_{tr}H_\theta + \frac{3}{r}H_{tr}H_{r\theta} + \frac{1}{r}H_{t\theta}H_{rr} + \frac{1}{r^2}H_{t\theta}H_r + \frac{4}{r^3}H_{t\theta}H_{\theta\theta} + \frac{1}{r}H_{trr}H_\theta + \frac{3}{r}H_{tr\theta}H_r + \frac{4}{r^3}H_{t\theta\theta}H_\theta = 0, \quad (3.2)$$

$$H_{rr}\left[4u_r + \frac{2}{r}v_\theta + \frac{2}{r}u + 4H_rH_{tr} + \frac{2}{r^2}H_\theta H_{t\theta}\right] + \left(\frac{1}{r}H_{r\theta} - \frac{1}{r^2}H_\theta\right)\left[2v_r + \frac{2}{r}u_\theta - \frac{2}{r}v + \frac{2}{r}H_\theta H_{tr}\right] + \left(\frac{1}{r^2}H_{\theta\theta} + \frac{1}{r}H_r\right)\left[2u_r + \frac{4}{r}v_\theta + \frac{4}{r}u + 2H_rH_{tr} + \frac{2}{r^2}H_\theta H_{t\theta}\right] + \frac{2}{r^4}H_{\theta\theta}H_\theta H_{t\theta} + \frac{2}{r^2}H_{r\theta}H_rH_{t\theta} - \frac{GH}{3\epsilon^2 h} + \frac{\Gamma\nabla^2 H}{3\epsilon^2 h} = \frac{1}{3}h^2\nabla^4 H_t, \quad (3.3)$$

where H is subject to clamped boundary conditions on the inner and outer cylinder walls,

$$H(R_i, \theta, t) = H(R_o, \theta, t) = 0, \left.\frac{\partial H}{\partial r}\right|_{r=R_i} = \left.\frac{\partial H}{\partial r}\right|_{r=R_o} = 0, \quad (3.4)$$

and the in-plane velocities are subject to no-slip conditions at the walls,

$$u(R_i, \theta, t) = u(R_o, \theta, t) = 0, \quad v(R_i, \theta, t) = v_i, \quad v(R_o, \theta, t) = v_o, \quad (3.5)$$

where the two cylinders of the annulus rotate relative to one another with an relative angular velocity Ω so that

$$\frac{v_o}{R_o} = \frac{v_i}{R_i} - \Omega. \quad (3.6)$$

Linear stability analysis allows examination of the conditions under which the sheet will deviate from its flat configuration. The equations of motion, linearized about a base solution of $H(r, \theta, t) = 0$ for small variations, become

$$4u_{rr} + \frac{3}{r}v_{r\theta} + \frac{1}{r^2}u_{\theta\theta} + \frac{4}{r}u_r - \frac{5}{r^2}v_\theta - \frac{4}{r^2}u = 0, \quad (3.7)$$

$$v_{rr} + \frac{3}{r}u_{r\theta} + \frac{4}{r^2}v_{\theta\theta} + \frac{1}{r}v_r + \frac{5}{r^2}u_\theta - \frac{1}{r^2}v = 0, \quad (3.8)$$

$$H_{rr}\left[4u_r+\frac{2}{r}v_\theta+\frac{2}{r}u\right]+\left(\frac{1}{r}H_{r\theta}-\frac{1}{r^2}H_\theta\right)\left[2v_r+\frac{2}{r}u_\theta-\frac{2}{r}v\right]+$$
$$\left(\frac{1}{r^2}H_{\theta\theta}+\frac{1}{r}H_r\right)\left[2u_r+\frac{4}{r}v_\theta+\frac{4}{r}u\right]-\frac{GH}{3\epsilon^2 h}+\frac{\Gamma\nabla^2 H}{3\epsilon^2 h}=\frac{1}{3}h^2\nabla^4 H_t. \tag{3.9}$$

(3.7) and (3.8) are decoupled from (3.9). Assuming radial symmetry, derivatives with respect to θ vanish, and the general solutions to (3.7) and (3.8) are

$$u=c_1 r+\frac{c_2}{r}, \tag{3.10}$$

$$v=c_3 r+\frac{c_4}{r}. \tag{3.11}$$

The only u satisfying the radial no-slip conditions of (3.5) on the lateral edges of the sheet is $u(r,\theta,t)=0$. The azimuthal velocities of the two boundaries determine the constants c_3 and c_4. The motion controlled by c_3 is a solid body rotation of the fluid which has no effect in the inertia-free scenario considered here, so for simplicity and without loss of generality, let us set $c_3=0$ and examine azimuthal velocities of the form $v=\frac{A}{r}$,

$$A=\frac{\Omega R_o^2 R_i^2}{R_o^2-R_i^2}. \tag{3.12}$$

Substituting these results into (3.9) yields

$$\frac{12Ah}{r^3}\left(\frac{H_\theta}{r}-H_{r\theta}\right)-\frac{GH}{\epsilon^2}+\frac{\Gamma\nabla^2 H}{\epsilon^2}=h^3\nabla^4 H_t \tag{3.13}$$

subject to (3.4). Let us consider disturbances from the base solution of the form

$$H(r,\theta,t)=\Re\left\{f(r)e^{\sigma t+im\theta}\right\} \tag{3.14}$$

with azimuthal wavenumber m and complex growth rate σ which, when substituted into (3.13), leads to the following stability equation:

$$\frac{d^4 f}{dr^4}+\frac{2}{r}\frac{d^3 f}{dr^3}-\left(\frac{2m^2+1}{r^2}+\Gamma_2\right)\frac{d^2 f}{dr^2}+\left(\frac{2m^2+iSm+1}{r^2}-\frac{\Gamma_2}{r}\right)\frac{df}{dr}+$$
$$\left(\frac{m^4-4m^2-iSm}{r^4}-G_2+\Gamma_2\frac{m^2}{r^2}\right)f=0, \tag{3.15}$$

where $S\equiv\frac{12A}{h^2\sigma}$ characterizes the ratio of the shear strain rate to the perturbation growth rate, $f(r)$ is subject to clamped conditions at $r=R_i$ and $r=R_o$, $G_2\equiv\frac{G}{\epsilon^2 h^3\sigma}$, and $\Gamma_2\equiv\frac{\Gamma}{\epsilon^2 h^3\sigma}$. In Section D.1, I show that σ is purely real.

Due to the difficulty of solving (3.15) analytically, I have investigated the behavior of the system by numerically solving the linearized sheet evolution equation, (3.13), using a variety of methods which serve to support and validate each other. Appendix F contains a detailed discussion of the numerical methods. The primary approach was a spectral collocation method suggested by Trefethen [32]. By solving

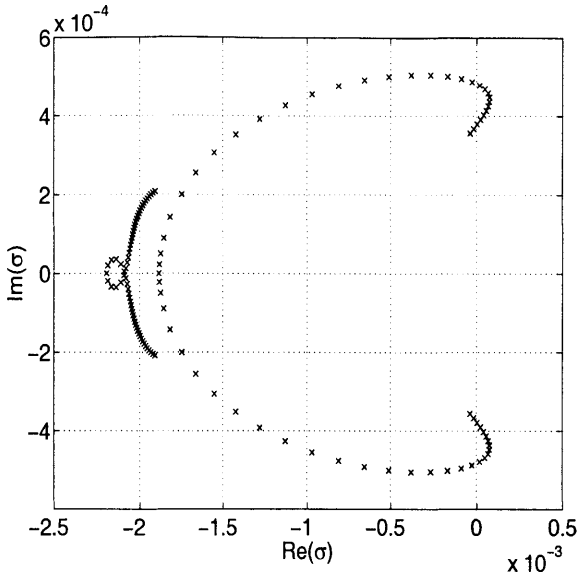

Figure 3-2: Eigenvalue spectrum just below the stability threshold for an annulus with $R_i/R_o = 0.457$. σ in the plot is the normalized growth rate of the instability expressed as the growth rate divided by the characteristic time scale, ϵ^2/Ω.

for the eigenvalues of the discrete equation, the growth and decay properties of all modes of deformation can be observed. In this manner, the conditions for marginal stability can be extracted by seeking the shear rate at which one eigenmode first acquires a positive growth rate while the remainder retain negative growth rates. At these conditions, disturbances with the form of the eigenmode in question will grow, while all other modes will decay. Thus, the eigenmode singled out by this method represents the most unstable mode of the system and ought to be the mode manifest in the physical system as the stability threshold is crossed. Figure 3-2 depicts the eigenvalue spectrum just below the stability threshold for one size annulus. The presence of nonzero imaginary components of the eigenvalues is an artifact of the discretization and, even for the discrete representation, does not present a significant effect because the azimuthal wave speeds of the ripples corresponding to the calculated imaginary components of the eigenvalues represent wave motion on a far slower time scale than the characteristic time scale for ripple growth. The shape of the most unstable mode for the same annulus is shown in Figure 3-3. The circles in Figure 3-5 display the predictions of linear stability theory. The same computational methods accurately reproduced the results of Appendix C when gravity and surface tension were neglected, serving as a check of the numerical scheme.

3.2 Experimental results

Using the apparatus pictured in Figure 3-4 a series of experiments were performed. The apparatus consists of a cylindrical trough of 6.56" inner diameter and a series of interchangeable center pieces, each with a different outer diameter. The center pieces

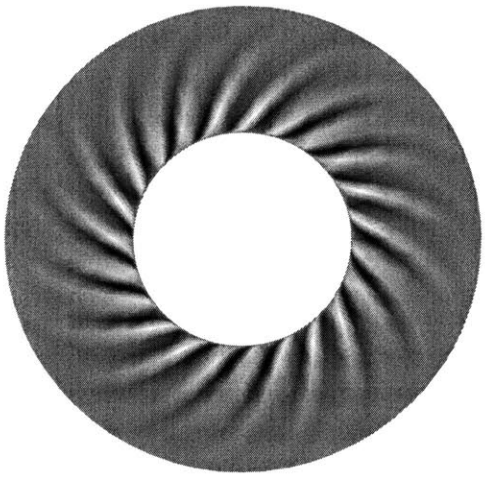

Figure 3-3: Most unstable mode shape for annulus with $R_i/R_o = 0.457$.

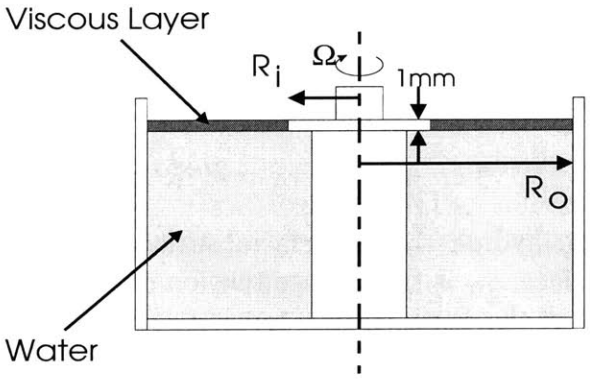

Figure 3-4: Experimental Apparatus

attach to a motor spindle protruding through the center of the bottom of the trough. Each center piece has a lip, 1mm thick, with carefully machined sharp edges that protrudes from the central column. The sharp edges pin liquid interfaces and prevent liquid wetting one surface from wetting the orthogonal surface. For each experiment, water fills the annular gap between the outer wall of the trough and the center piece like a moat until it wets the bottom surface of the lip but not the vertical side surface. Next, some preheated experimental fluid (Amoco Indopol H300), which is less dense than water, is poured onto the surface of the water. It flows to form a viscous fluid layer of thickness 2mm. Because the capillary length ($\sqrt{\gamma/\rho g}$) of the fluid is less than 2mm, no holes in the layer form. No experiments are performed until the fluid has spread for twenty-four hours to ensure a uniform layer. During this time, the fluid also cools to room temperature. A controller operating the motor attached to the apparatus center piece allows an experimenter to vary and record the angular velocity, Ω, of the center piece.

In each experiment, the angular velocity at onset of wrinkling, Ω_C, and the number of wrinkles, m, were recorded. Starting from rest with an unperturbed surface, the angular velocity of the inner cylinder was slowly ramped up until the first ripples began to appear in the surface. The angular velocity at the time of onset was recorded from the motor controller. A video camera above the apparatus recorded the experiments, and the number of ripples present at onset was counted from the video tape. During a series of experiments with a single center piece, at least eight hours elapsed between experiments to ensure that no residual effects of the previous experiment remained in the viscous sheet.

The fluid used in these experiments was Amoco Indopol H-300, a form of polybutene with density $0.90 kg/m^3$ and surface tension $0.0213 N/m$. The density was measured using a balance and a container of known volume filled with the H-300. The container volume was measured using the same balance by recording the mass of water contained in the full vessel. The surface tension of the H-300 was measured using a platinum plate in a Kruss surface tensiometer. The surface tension of the water, measured using the same method, was $0.0716 N/m$. The surface tension between the Indopol H-300 and water can be calculated using Good-Fowkes model which for water-hydrocarbon interfaces suggests

$$\gamma_{WH} = \gamma_W + \gamma_H - 2(\gamma_W^d \gamma_H)^{\frac{1}{2}} \tag{3.16}$$

where γ_{WH} is the water-hydrocarbon interfacial surface tension, γ_W is the surface tension of water-air interface, γ_H is the surface tension of the hydrocarbon-air interface, and γ_W^d is the portion of the water surface tension generated by dispersion forces and is suggested to be approximately $0.0218 N/m^2$ [1]. The Good-Fowkes model predicts a water-H-300 interfacial surface tension of $0.050 N/m$. The shear viscosity of Indopol H-300, as measured using an AR-1000N Rheometer in a cone and plate configuration with a $4cm$ cone with a 4° angle of inclination, was $136.4 Pa \cdot s$. Based on a Maxwell fluid model and oscillatory rheometer tests with the AR-1000N, the relaxation time for this fluid $\tau_R < 0.001 s$. For such a fluid, the hydrodynamic forces generated by viscous stresses in the underlying water bath can safely be ignored as the charac-

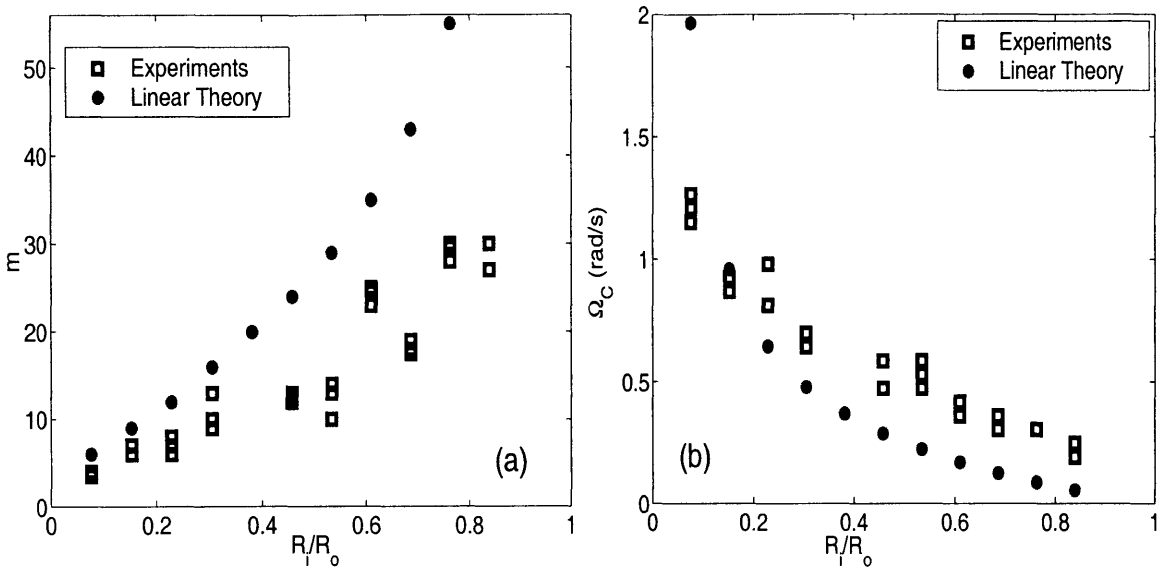

Figure 3-5: Results of experiments and predictions of linear stability theory for Indopol H-300. $m \equiv$ azimuthal wavenumber, $\Omega_C \equiv$ critical angular velocity.

teristic viscous stresses in the water are nearly 140,000 times smaller than those in the Indopol H-300 film. Also, because the relaxation time of the H-300, τ_R, is much shorter than the characteristic time scale in the experiments ($\tau \sim \epsilon L/U \sim 0.02s$), the Deborah number, $De = \tau_R/\tau << 1$, and any elastic effects in the fluid are negligible. A characteristic Bond number for the set up is $Bo \sim 100$ implying that gravity plays a more important role than capillarity here. A characteristic capillary number is $Ca \sim 100$ implying that surface tension effects are small compared to viscous effects.

Figure 3-5 depicts the results of the experiments as squares.

3.3 Discussion

In a series of experiments inspired by but qualitatively different from G.I. Taylor's observations [30], a long wavelength instability in a viscous Newtonian annular sheet subjected to shearing was noted. The instability is analogous to one explored by W.R. Dean [11] in the context of a sheared elastic sheet. These experiments have quantified the instability by determining the conditions for its occurrence and measuring the wavelength at onset. Linear stability analysis shows the critical shear rate for onset and the number of ripples as illustrated in Figure 3-5. The important effects that are included in this analysis are the damping effects of gravity and surface tension that produce a non-zero critical angular velocity for the onset of wrinkling of the sheet. A number of potential sources of error for the predictions exist. Since this theory is an asymptotic one in the limit of small thickness, any sheet of finite thickness might be expected to show small deviations. Second, in these experiments, though the angular velocity of the inner cylinder of the annulus was ramped up slowly, the angular velocity, nevertheless, was transient. No transient edge boundary effects were

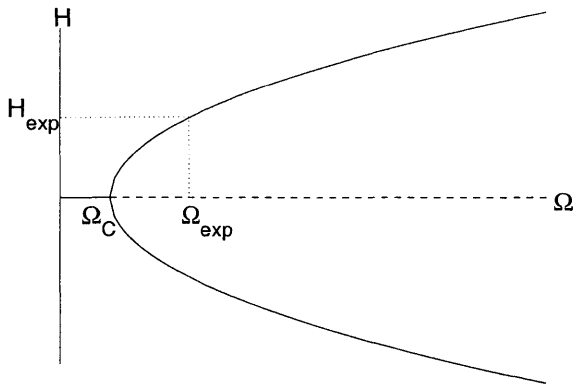

Figure 3-6: Schematic of supercritical pitchfork bifurcation. $\Omega_C \equiv$ critical angular velocity, $\Omega_{exp} \equiv$ angular velocity measured in experiment, $H_{exp} \equiv$ amplitude in experiment.

considered in this analysis. Third, and perhaps most significantly, if the instability is a supercritical pitchfork bifurcation, then the ripples will be infinitesimal at onset. Infinitesimal ripples are difficult to observe, and, therefore, the data recorded in these experiments corresponds necessarily to a regime slightly beyond the onset of the instability when the ripples have grown to be visible as schematically illustrated in Figure 3-6. Therefore, it follows that the number of ripples seen in the experiments might differ from that predicted for onset by the linear model. Although the model is only strictly valid for infinitesimal deviations from a flat sheet, for small amplitudes close to onset the model should remain a close approximation. To try to compare the experiment and theory differently, the experimental conditions (i.e. Ω_{exp}) were used in the model to evaluate the number of ripples. Figure 3-7 depicts the predictions of the linearized theory for what would occur at $\Omega = \Omega_{exp}$. The agreement is good. That $\Omega_{exp} > \Omega_C$ is supported by the data in Figure 3-5(b). The underestimation of the number of ripples at onset in Figure 3-5(a) can be understood using (2.36). The fastest growing mode is $k^* = \arg\max \sigma(k)$,

$$k^* = \sqrt{\frac{2G}{C - \Gamma}}. \tag{3.17}$$

When Ω goes up, C which is proportional to Ω goes up, and k^* goes down. Therefore, one should expect that for $\Omega_{exp} > \Omega_C$, $k^*_{exp} < k^*_C$ as supported by Figure 3-5(a).

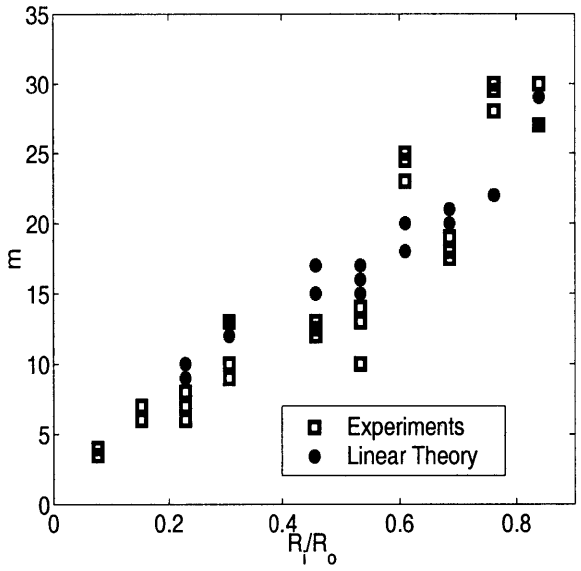

Figure 3-7: Results of experiments and predictions of linear theory for experimental conditions (Ω_{exp}) for Indopol H-300. $m \equiv$ azimuthal wavenumber.

Chapter 4

Buckling instability of a thin-layer plane Couette flow

Couette channel flow is stable at all shear rates. However, if, instead of a channel of infinite depth with no variation through the depth, the channel contains a thin sheet with free surfaces, the Couette flow becomes unstable to infinitesimal shear rates. Consider an infinitely long sheet of a viscous Newtonian fluid of finite width $2B$ and uniform thickness $h << B$ as shown in Figure 4-1. The surfaces of the sheet are free, and the edges are in contact with solid walls which shear the sheet by moving lengthwise with velocities $\pm U$ respectively.

4.1 Linear stability

For small out-of-plane displacements, the sheet is governed by the equations given in Section 2.4. The in-plane velocity field, $\bar{u} = Uy/B$ and $\bar{v} = 0$, satisfies the linearized in-plane force balances

$$4h\bar{u}_{xx} + 3h\bar{v}_{xy} + h\bar{u}_{yy} = 0 \tag{4.1}$$

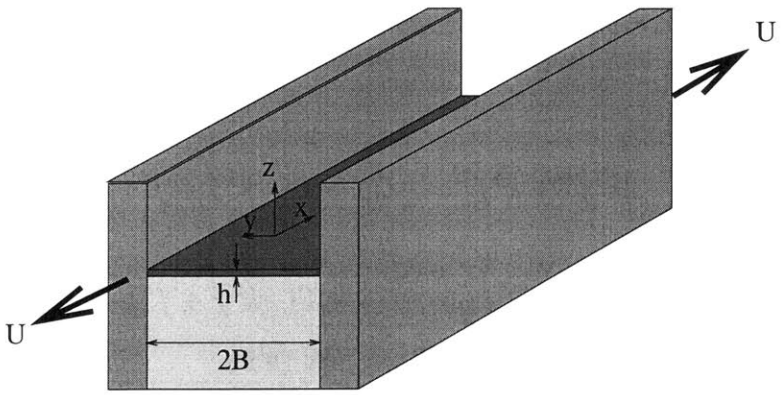

Figure 4-1: Schematic of system

and

$$4h\bar{v}_{yy} + 3h\bar{u}_{xy} + h\bar{v}_{xx} = 0. \tag{4.2}$$

The shear strain rate in the sheet is $\dot{\gamma} = U/B$. The behavior of the sheet is then governed by the equation

$$\frac{\mu h^3}{3}\nabla^4 H_t = (\gamma^+ + \gamma^-)\nabla^2 H - \rho g H + 2\mu h\dot{\gamma} H_{xy} \tag{4.3}$$

where $H(x, y, t)$ is the out-of-plane displacement of the sheet, the x-axis points along the length of the sheet, and the y-axis points across the width of the sheet. (4.3) can be nondimensionalized utilizing the following scaling:

$$x = \hat{x}B, \quad y = \hat{y}B, \quad H = \hat{H}\epsilon B, \quad h = \hat{h}\epsilon B, \quad t = \hat{t}\epsilon^2\frac{B}{U}, \tag{4.4}$$

where ϵ is the slenderness ratio, h/B. The resulting nondimensional equation, omitting hats, is

$$\nabla^4 H_t = \Gamma\nabla^2 H - GH + 6H_{xy}, \tag{4.5}$$

where $G \equiv \frac{3\rho g B^2}{\epsilon\mu U}$ and $\Gamma \equiv \frac{3(\gamma^+ + \gamma^-)}{\epsilon\mu U}$. The boundary conditions are

$$\begin{aligned} H(x, -B, t) = H(x, B, t) = 0, \quad & H_y(x, -B, t) = H_y(x, B, t) = 0, \\ u(x, \pm B, t) = \pm U, \quad & v(x, \pm B, t) = 0. \end{aligned} \tag{4.6}$$

Let us consider solutions to (4.5) of the form

$$H = \frac{1}{2}\left(f(y)e^{\sigma t + ikx} + \bar{f}(y)e^{\bar{\sigma}t - ikx}\right), \tag{4.7}$$

where $\bar{f}$ is the complex conjugate of f. In Section D.2, I show that σ is strictly real, so $\bar{\sigma} = \sigma$. Substituting (4.7) into (4.5) yields

$$\begin{aligned} &\sigma\left[e^{ikx}\left(f'''' - 2k^2 f'' + k^4 f\right) + e^{-ikx}\left(\bar{f}'''' - 2k^2\bar{f}'' + k^4\bar{f}\right)\right] = \\ &-G\left(fe^{ikf} + \bar{f}e^{-ikf}\right) + \Gamma\left(-k^2 fe^{ikx} + f''e^{ikx} - k^2\bar{f}e^{-ikx} + \bar{f}''e^{-ikx}\right) \\ &+6\left(ikf'e^{ikx} - ik\bar{f}'e^{-ikx}\right). \end{aligned} \tag{4.8}$$

e^{ikx} and e^{-ikx} are independent, so the terms multiplying each can be separated leading to two equations,

$$\sigma\left[f'''' - 2k^2 f'' + k^4 f\right] = -Gf + \Gamma(-k^2 f + f'') + 6ikf' \tag{4.9}$$

and

$$\sigma\left[\bar{f}'''' - 2k^2\bar{f}'' + k^4\bar{f}\right] = -G\bar{f} + \Gamma(-k^2\bar{f} + \bar{f}'') - 6ik\bar{f}'. \tag{4.10}$$

(4.10) is the conjugate of (4.9), so I will use just (4.9),

$$f'''' - \left(2k^2 + \frac{\Gamma}{\sigma}\right)f'' - \frac{6ik}{\sigma}f' + \left(k^4 + \frac{\Gamma}{\sigma}k^2 + \frac{G}{\sigma}\right)f = 0 \tag{4.11}$$

subject to the boundary conditions

$$f(\pm 1) = 0 \quad f'(\pm 1) = 0. \tag{4.12}$$

For $\sigma \neq 0$, the general solution to (4.11) can be written as

$$f(y) = \sum_{j=1}^{4} C_j e^{i\lambda_j y}, \tag{4.13}$$

where the λ_j satisfy the characteristic equation of the differential equation,

$$\lambda^4 + \left(2k^2 + \frac{\Gamma}{\sigma}\right)\lambda^2 + \frac{6k}{\sigma}\lambda + k^4 + \frac{\Gamma}{\sigma}k^2 + \frac{G}{\sigma} = 0. \tag{4.14}$$

The boundary conditions can be written in matrix form as

$$\begin{bmatrix} e^{i\lambda_1} & e^{i\lambda_2} & e^{i\lambda_3} & e^{i\lambda_4} \\ e^{-i\lambda_1} & e^{-i\lambda_2} & e^{-i\lambda_3} & e^{-i\lambda_4} \\ i\lambda_1 e^{i\lambda_1} & i\lambda_2 e^{i\lambda_2} & i\lambda_3 e^{i\lambda_3} & i\lambda_4 e^{i\lambda_4} \\ -i\lambda_1 e^{-i\lambda_1} & -i\lambda_2 e^{-i\lambda_2} & -i\lambda_3 e^{-i\lambda_3} & -i\lambda_4 e^{-i\lambda_4} \end{bmatrix} \begin{bmatrix} C_1 \\ C_2 \\ C_3 \\ C_4 \end{bmatrix} = 0. \tag{4.15}$$

For nontrivial solutions, the matrix in (4.15) must be singular, so

$$\begin{vmatrix} e^{i\lambda_1} & e^{i\lambda_2} & e^{i\lambda_3} & e^{i\lambda_4} \\ e^{-i\lambda_1} & e^{-i\lambda_2} & e^{-i\lambda_3} & e^{-i\lambda_4} \\ i\lambda_1 e^{i\lambda_1} & i\lambda_2 e^{i\lambda_2} & i\lambda_3 e^{i\lambda_3} & i\lambda_4 e^{i\lambda_4} \\ -i\lambda_1 e^{-i\lambda_1} & -i\lambda_2 e^{-i\lambda_2} & -i\lambda_3 e^{-i\lambda_3} & -i\lambda_4 e^{-i\lambda_4} \end{vmatrix} = 0 \tag{4.16}$$

which can be rewritten as

$$\begin{vmatrix} \sin\lambda_1 & \sin\lambda_2 & \sin\lambda_3 & \sin\lambda_4 \\ \cos\lambda_1 & \cos\lambda_2 & \cos\lambda_3 & \cos\lambda_4 \\ \lambda_1\sin\lambda_1 & \lambda_2\sin\lambda_2 & \lambda_3\sin\lambda_3 & \lambda_4\sin\lambda_4 \\ \lambda_1\cos\lambda_1 & \lambda_2\cos\lambda_2 & \lambda_3\cos\lambda_3 & \lambda_4\cos\lambda_4 \end{vmatrix} = 0 \tag{4.17}$$

which expands to

$$(\lambda_1-\lambda_2)(\lambda_3-\lambda_4)\sin(\lambda_1-\lambda_3)\sin(\lambda_2-\lambda_4) = (\lambda_1-\lambda_3)(\lambda_2-\lambda_4)\sin(\lambda_1-\lambda_2)\sin(\lambda_3-\lambda_4). \tag{4.18}$$

The growth rate, $\sigma(k)$, of a mode with wavenumber k is determined by the simultaneous solution of (4.14) and (4.18). The mode with the highest growth rate determines the shape of the viscous sheet at the onset of the instability.

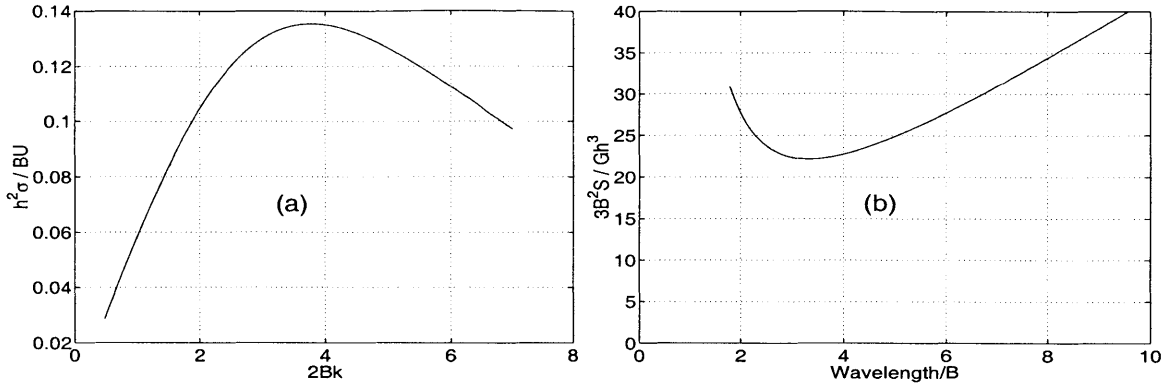

Figure 4-2: (a) Normalized growth rate $h^2\sigma/BU$ versus normalized wavenumber $2Bk$ relationship for a sheared rectilinear viscous sheet when $G = \Gamma = 0$. (b) Normalized critical shear force $3B^2S/Gh^3$ versus normalized wavelength relationship for a sheared rectilinear incompressible elastic sheet with no oscillations as analyzed by Southwell and Skan [28]. S is the shear force per unit length of the channel, and G is the shear modulus. If the viscous result is replotted in this fashion, exactly the same plot results with the y-axis relabeled $3BU/h^2\sigma = 3B^2S/\mu h^3\sigma$.

4.2 The limit $G = \Gamma = 0$

Considering first the absence of both gravity and surface tension, the governing differential equation for f, (4.11), reduces to

$$f'''' - 2k^2 f'' - \frac{6ik}{\sigma} f' + k^4 f = 0, \tag{4.19}$$

and (4.14) reduces to

$$\lambda^4 + 2k^2\lambda^2 + \frac{6k}{\sigma}\lambda + k^4 = 0. \tag{4.20}$$

It is immediately apparent that if $\sigma = 0$, the only solution is $f(y) = 0$ which is trivial; thus there is no condition of neutral stability. For $\sigma \neq 0$, (4.19) and (4.20) can be solved to yield the relationship of the mode wavenumber to the growth rate as shown in Figure 4-2(a). The maximum of the plot corresponds to the fastest growing mode. The fastest growing mode has a wavelength equal to $3.318B$, where B is the channel half-width. These data were generated by finding the eigenvalues and eigenmodes of the discretized evolution equation using a spectral collocation method suggested by Trefethen [32] and discussed in more detail in Appendix F.

This calculation is analogous to one performed by Southwell and Skan [28] for the stability of a flat elastic strip under shearing in a similar configuration. (4.19) and (4.20) arise in the elastic case as well with the shear strain rate divided by the growth rate, $6/\sigma$, replaced by the shear strain, 6, so that

$$f'''' - 2k^2 f'' - 6ikf' + k^4 f = 0 \tag{4.21}$$

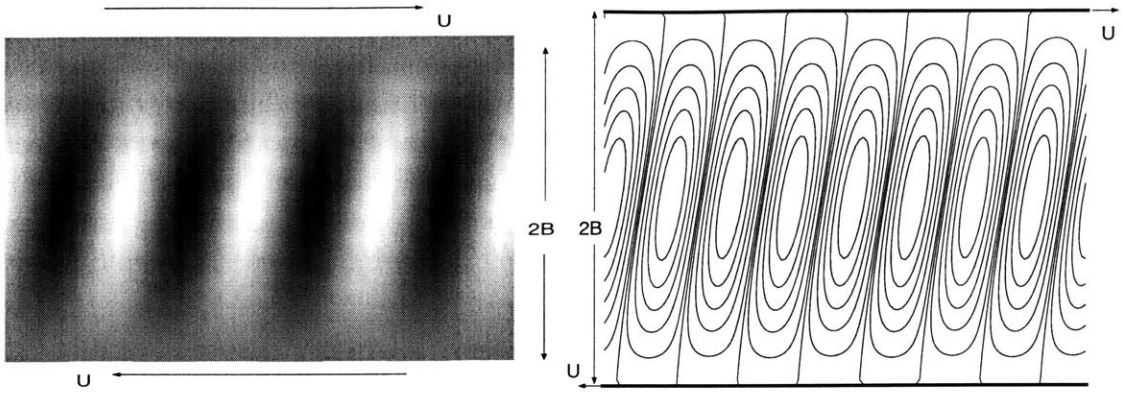

Figure 4-3: The most unstable mode shape.

and

$$\lambda^4 + 2k^2\lambda^2 + 6k\lambda + k^4 = 0. \tag{4.22}$$

To produce the same shear force, the viscous sheet is subjected to a shear strain rate whereas the elastic plate is subjected to a shear strain. Figure 4-2(b) shows the results of their calculations and equivalently the results in Figure 4-2(a) plotted in the same fashion as theirs. They too calculated a most unstable wavelength of $3.318B$. If the ordinate in Figure 4-2 is thought of in terms of strain rather than force, then for the elastic case $3B^2S/Gh^3 = 3BU/h^2$. Couched in this form, the elastic-viscous analogy is transparent with U in the elastic case (a displacement) replaced by U/σ in the viscous case (a velocity divided by a growth rate). Figure 4-3 depicts the mode shape of the fastest growing distortion of the strip.

4.3 The case $G \neq 0$, $\Gamma \neq 0$

The sheared viscous sheet behaves in a fashion similar to the compressed planar sheet discussed in Section 2.6, but an additional length scale is present, the channel width. The channel width sets a maximum wavelength in the y-direction. Also, the shearing generates tensile in addition to compressive forces. The general principles governing the stability are unchanged. If surface tension is strong enough relative to shear, the sheet will be stable to all wavelengths of disturbance. The stability threshold is governed by the sign of the minimum principal depth-integrated stress component. A negative minimum principal depth-integrated stress component indicates the presence of compressive forces in the sheet. The minimum principal depth-integrated stress component, T_{min}, takes the value [10]

$$T_{min} = \frac{T_{11} + T_{22}}{2} - \sqrt{T_{12}^2 + \left(\frac{T_{11} - T_{22}}{2}\right)^2}. \tag{4.23}$$

In this case, where in (2.24) $T_{12} = 3$ and, when the contribution due to surface tension is incorporated into the other depth-integrated stresses, $T_{11} = T_{22} = \Gamma$, $T_{min} = \Gamma - 3$. For $\Gamma > 3$, $T_{min} > 0$, so there are no compressive forces in the sheet, and the the

system is stable to all wavelengths of perturbation. When $\Gamma < 3$, $T_{min} < 0$, there are compressive forces in the sheet, and the system is unstable.

The term on the left-hand side of (4.5) representing bending plays a resistive rather than a restorative role and thus helps control the rate of growth or decay of the instability but not the presence or absence of stability itself. The stability criterion emerges strictly from the interplay between the terms on the right-hand side. Thinking once again in terms of principal depth-integrated stress components [10],

$$T_{max} = \frac{T_{11} + T_{22}}{2} + \sqrt{T_{12}^2 + \left(\frac{T_{11} - T_{22}}{2}\right)^2}. \tag{4.24}$$

In this case, $T_{max} = \Gamma + 3$. The wrinkles will form with their spines perpendicular to the principal direction of compression with its compression of magnitude T_{min} and along the principal direction of tension with its tension of magnitude T_{max}. The principal directions in this situation of shear plus isotropic tension will lie at forty-five degree angles to the shear, or forty-five degree angles to the walls of the channel. The wrinkles will assume the minimum possible curvature in the tensile direction corresponding to a wavelength of twice the span of the channel in the principal tensile direction, $4\sqrt{2}$ in nondimensional form.

Figure 4-4 shows the variation in the most unstable mode with G and Γ from results computed using the same numerical scheme as in Section 4.2 and described in Appendix F. Similarly, Figure 4-5 shows how the dispersion relation depends on the variations in G and Γ. For a film of Indopol H-300 on water as used in the annular experiments, with $h = 2mm$ and $B = 2cm$, this model predicts the stability threshold corresponding to $\Gamma = 3$ to occur when $U = 0.52cm/s$, a value on par with the shear velocities found in the annular experiments at small gap widths.

4.4 Discussion

This chapter explored the linear stability of a sheared viscous strip analogous to that examined by Southwell and Skan for a sheared elastic strip. Computation confirmed that the most unstable mode for the viscous strip (that which grows most quickly) in the absence of gravity and surface tension corresponds to the most unstable mode for the elastic strip (that which appears at the lowest imposed shear stress). In the elastic case, a finite shear stress is required to excite the instability. The viscous strip is unstable at all magnitudes of imposed shear stress, but a single mode of deformation emerges due to the differences in growth rates of the various possible modes. For a given imposed shear stress, one mode will grow faster than all of the others. The presence of gravity and surface tension leads to a finite threshold for the appearance of the instability. Surface tension produces the threshold. Shearing insufficient to overcome surface tension will yield no departure from the planar form of the sheet. Only when the shearing exceeds the restoring tensile effect of surface tension do wrinkles appear in the sheet. Gravity contributes to the existence of a cutoff wavenumber below which no perturbations can grow. The combination of gravity and surface tension generates a situation where for a given shear stress above the threshold value, all perturba-

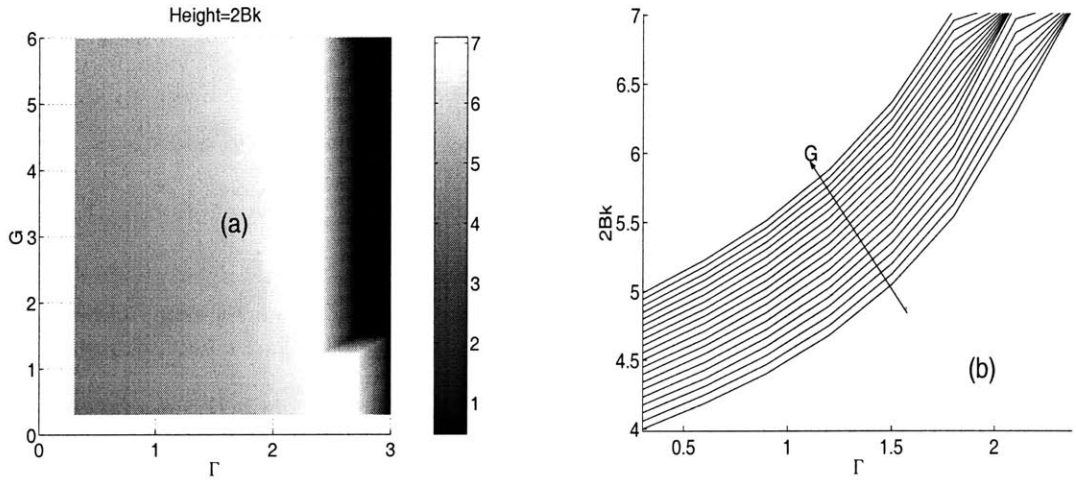

Figure 4-4: Variation of the most unstable normalized wavenumber $2Bk$ with gravity and surface tension parameters, $G \equiv \frac{3\rho g B^2}{\epsilon\mu U}$, $\Gamma \equiv \frac{3(\gamma^+ + \gamma -)}{\epsilon\mu U}$. The same data are presented in (a) as a shaded contour in which the dark area on the right represents the region of stability and the height of the surface represents the most unstable wavenumber and presented in (b) as a series of curves with varying values of G. In the plot on the right, the curves of constant G are shown at intervals of 0.3 in G.

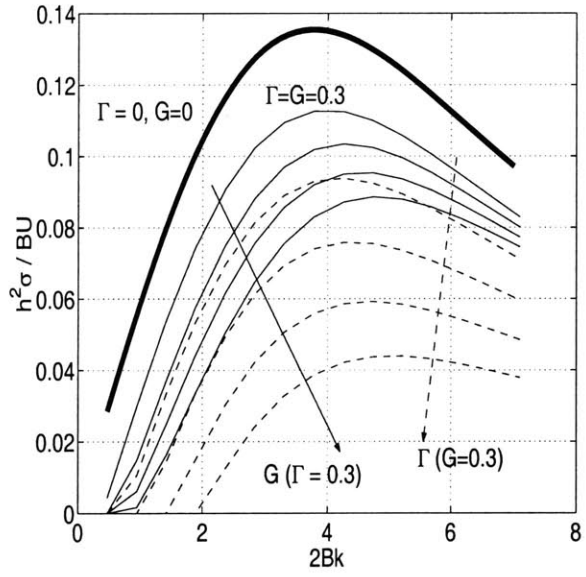

Figure 4-5: Dispersion relation. Family of curves showing normalized growth rate versus normalized wave number for varying $G \equiv \frac{3\rho g B^2}{\epsilon\mu U}$ and $\Gamma \equiv \frac{3(\gamma^+ + \gamma -)}{\epsilon\mu U}$. The top curve is for zero gravity and surface tension. The next curve represents $\Gamma = G = 0.3$. The dashed curves then represent a progression of increasing Γ in steps of 0.3. The solid curves represent a progression of increasing G in steps of 1.2.

tions with wavenumbers above the cutoff wavenumber will grow, and one will grow faster than all of the others. Computations reveal the quantitative relationship between gravity, surface tension, shear stress, geometry, perturbation wavenumber, and growth rate and pinpoint the most unstable mode. The calculated stability threshold is of the same order exhibited by the annular experiments for narrow gaps.

Chapter 5

Nonlinear effects: amplitude of the instability

5.1 Introduction

When a sheet of viscous Newtonian fluid is sheared, it develops wrinkles above a critical shear rate. The wrinkles grow to a point, and then their amplitude saturates. In experiments with an annular configuration, the wrinkles have been observed to travel around the annulus with a wave speed between the speed of the inner cylinder and the speed of the outer cylinder. The equations and boundary conditions are sensitive only to the relative rates of rotation of the two cylinders and not to the absolute rates of rotation. The same holds true for the rectilinear case; only the relative velocities of the walls matter. Here I consider what the equations governing the sheet predict in the way of saturation. Let us consider a frame of reference in which the wrinkles have a wave speed of zero at saturation. In this frame of reference, at saturation

$$\frac{\partial H}{\partial t} = 0. \tag{5.1}$$

This chapter examines a number of possibilities regarding the nature and governing equations of the saturation of the instability. First, the original equations of Section 2.4 are examined and it is argued that they do not predict saturation. Next, a natural progression of new scalings is considered leading to a scaling of the equations allowing saturation to occur. Finally, an order of magnitude argument for the amplitude of the ripples at saturation is derived from the scaled equations.

A scaling for the amplitude at saturation seems to present itself immediately out of even the two-dimensional equations:

$$DH_{xxxxt} = (T_{11} + \Gamma)H_{xx} - \rho g H \tag{5.2}$$

$$T_{11} = 4\mu h[\bar{u}_x + H_x H_{xt}]. \tag{5.3}$$

At saturation, the dominant balance is

$$T_{11}H_{xx} \sim \rho g H \tag{5.4}$$

or

$$\mu h \frac{U}{L}\frac{H}{\lambda^2} \sim \rho g H. \tag{5.5}$$

If at saturation, as experiments suggest, $H \sim L \sim \lambda$,

$$H \sim \sqrt[3]{\frac{\mu U h}{\rho g}}. \tag{5.6}$$

It shall be seen that this very scaling eventually emerges, but it does not constitute a consistent picture of the model without modifications to the formulation.

5.2 Saturation occurs when $H > h$

At saturation, the equations remaining from (2.21)-(2.24) are linear so that no saturation is predicted by the original equations. That the original equations do not predict saturation comes as no surprise since the conditions at saturation violate at least one of the premises of their derivation. The original equations evolved from the Stokes equations by way of an assumption $u \sim \epsilon w$. At saturation, w arises solely from a coupling of u to H_x. The original scaling also suggested that $H \sim h$ and that therefore $H_x \sim \epsilon$. This would suggest that w, far from being $O(u/\epsilon)$, would in fact be $O(\epsilon u)$.

Let us consider a rescaling of the equations appropriate for saturated wrinkles with amplitudes of the order of the thickness of the sheet.

$$\begin{array}{llllll} u \sim U, & v \sim U, & w \sim \epsilon U, & P \sim \mu\frac{U}{L} & & \\ h \sim \epsilon L, & H \sim \epsilon L, & x \sim L, & y \sim L, & z \sim \epsilon L. & \end{array} \tag{5.7}$$

This scaling is the one used in lubrication theory. Appendix E contains the details of the derivation. The resulting governing equations in terms of leading order variables are

$$T_{11} \equiv \mu(4\bar{u}_x + 2\bar{v}_y)h, \tag{5.8}$$

$$T_{22} \equiv \mu(4\bar{v}_y + 2\bar{u}_x)h, \tag{5.9}$$

$$T_{12} \equiv \mu(\bar{u}_y + \bar{v}_x)h, \tag{5.10}$$

$$\frac{\partial T_{11}}{\partial x} + \frac{\partial T_{12}}{\partial y} = 0, \tag{5.11}$$

$$\frac{\partial T_{12}}{\partial x} + \frac{\partial T_{22}}{\partial y} = 0, \tag{5.12}$$

and

$$H_{xx}T_{11} + 2H_{xy}T_{12} + H_{yy}T_{22} = \rho g H \tag{5.13}$$

which are linear in H and thus cannot model saturation because they contain no amplitude information. This result suggests that saturation does not occur while the amplitude of the wrinkles remains of the order of the thickness of the sheet. To understand saturation, we must consider wrinkles with slopes of order unity.

5.3 A new scaling for the amplitude saturation

At large displacements of the viscous sheet ($H_x \sim H_y \sim 1$), derivatives with respect to the fixed Cartesian coordinates, x and y, cannot be considered small compared to derivatives in the z-direction because for $H_x \sim 1$, a small change of position in a direction parallel to the original plane of the sheet entails a similarly sized change of position through the depth of the sheet. Thus, the separation of scales used in the original scaling becomes invalid at large displacements, and derivatives with respect to the x and y directions have magnitudes on the same order as derivatives in the z-direction. The logic underlying the original separation of scales remains valid: changes occurring through the depth of the sheet are expected to happen over a distance on the order of the thickness of the sheet, while changes along the span of the sheet are expected to occur over distances proportional to the in-plane dimensions of the sheet. This separation of scales in the problem can be recovered in the equations through the utilization of sheet-centered non-orthogonal curvilinear coordinates. The detailed derivation of the scaling argument can be found in Appendix E.

Let x', y', and z' be the sheet-centered curvilinear coordinates, where $\vec{z}'$ points in the original $\vec{z}$ direction; $\vec{x}'$ points along the sheet center-surface in the original $x-z$ plane; and $\vec{y}'$ points along the sheet center-surface in the original $y-z$ plane (see Figure 5-1). Let the origin of the (x',y',z') system lie on the sheet center-surface.

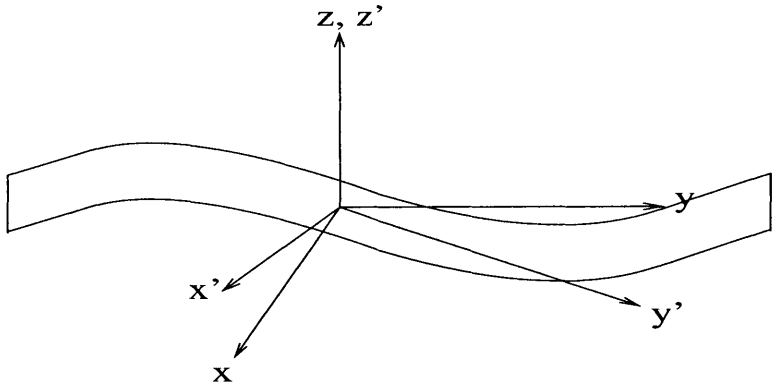

Figure 5-1: Original fixed and new curvilinear axes shown with the $y-z$ plane cross-section of the sheet.

Once again, at saturation, with the displacement of the sheet constant, w will result from coupling between u and H_x. With slopes of $O(1)$, $w \sim u$. Let us retain expression of the velocities in the original fixed orthogonal coordinate system. The following scaling is suggested by this model:

$$\begin{array}{lll} u \sim U, & v \sim U, & w \sim U, \\ x \sim x' \sim L, & y \sim y' \sim L, & z' \sim \epsilon L, \\ z \sim L, & H \sim L, & h \sim \epsilon L, \\ P \sim \mu \frac{U}{L} & \frac{\partial}{\partial x'} \sim \frac{\partial}{\partial y'} \sim \frac{1}{L}, & \frac{\partial}{\partial z'} \sim \frac{1}{\epsilon L}, \end{array} \tag{5.14}$$

and for quantities without z-dependence

$$\frac{\partial}{\partial x} \sim \frac{\partial}{\partial y} \sim \frac{1}{L}. \tag{5.15}$$

Under this scaling the resulting governing equations for the sheet are as follows (where all terms are leading order quantities unless explicitly noted):

$$u = \bar{u} \tag{5.16}$$

$$v = \bar{v} \tag{5.17}$$

$$w = H_t + \bar{u}H_x + \bar{v}H_y \tag{5.18}$$

$$P = 2\mu\left(\bar{u}_x + \bar{v}_y\right) - \mu\frac{D}{Dt}\left[\ln\left(1 + H_x^2 + H_y^2\right)\right] \tag{5.19}$$

$$u^{(1)} = \bar{u}^{(1)} + z' f_6(x, y, t) \tag{5.20}$$

$$v^{(1)} = \bar{v}^{(1)} + z' f_7(x, y, t) \tag{5.21}$$

$$f_6 \equiv \frac{H_x(2\bar{u}_x + \bar{v}_y) + H_y\bar{u}_y + H_x\frac{D}{Dt}\left[\ln\left(1 + H_x^2 + H_y^2\right)\right] - \frac{DH_x}{Dt}}{1 + H_x^2 + H_y^2} \tag{5.22}$$

$$f_7 \equiv \frac{H_y(\bar{u}_x + 2\bar{v}_y) + H_x\bar{v}_x + H_y\frac{D}{Dt}\left[\ln\left(1 + H_x^2 + H_y^2\right)\right] - \frac{DH_y}{Dt}}{1 + H_x^2 + H_y^2} \tag{5.23}$$

$$\frac{\partial T_{11}}{\partial x} + \frac{\partial T_{12}}{\partial y} = 0 \tag{5.24}$$

$$\frac{\partial T_{12}}{\partial x} + \frac{\partial T_{22}}{\partial y} = 0 \tag{5.25}$$

$$\frac{H_{xx}T_{11} + 2H_{xy}T_{12} + H_{yy}T_{22}}{1 + H_x^2 + H_y^2} - \rho g H + 2(\gamma^+ + \gamma^-)\kappa = 0 \tag{5.26}$$

$$T_{11} \equiv [2\mu\bar{u}_x - P - 2\mu H_x f_6]h \tag{5.27}$$

$$T_{22} \equiv [2\mu\bar{v}_y - P - 2\mu H_y f_7]h \tag{5.28}$$

$$T_{12} \equiv \mu[\bar{u}_y + \bar{v}_x - H_y f_6 - H_x f_7]h. \tag{5.29}$$

$$2\kappa \equiv \frac{(1 + H_y^2)H_{xx} - 2H_x H_y H_{xy} + (1 + H_x^2)H_{yy}}{(1 + H_x^2 + H_y^2)^{3/2}} \tag{5.30}$$

Thinking about the rectilinear sheet being sheared by two parallel walls a distance $2L$ apart moving in opposite directions, each with speed U, call H the amplitude of the wrinkles and λ their wavelength. Noting that gravity has a much more significant effect than capillarity for reasonable experimental values of the parameters, for $H \sim \lambda \sim L$, the following scaling emerges:

$$H \sim \sqrt[3]{\frac{\mu U h}{\rho g}}. \tag{5.31}$$

As expected, increasing the restoring forces in the form of ρ and g decreases the amplitude; increasing the driving force in the form of U increases the amplitude; and, increasing either μ or h will increase amplitude because, for a given U, the viscous forces are proportional to μ and h. For reasonable values of the parameters, $\mu \sim 10^3 Pa \cdot s$, $U \sim 10^{-2} m/s$, $h \sim 10^{-3} m$, and $\rho \sim 10^3 kg/m^3$, the scaling predicts $H \sim 10^{-2} m$ a result quite in keeping with experimental observations.

Chapter 6

The viscous catenary

6.1 Introduction

The term catenary describes the form of a chain hanging between two points and is in fact derived from the Latin word for chain [13]. In 1691, Leibniz, Huygens, and Johann Bernoulli became the first to discover the equation of the catenary in response to a challenge set forth by Johann's older brother, Jacob Bernoulli. Huygens coined the term in a 1690 letter to Leibniz discussing the topic [20]. This chapter explores the behavior of the viscous catenary. If a filament of an incompressible highly viscous fluid forms a bridge across the gap between two solid vertical walls, it will sag under the influence of gravity. The scaling of the variables for this scenario matches that leading up to the governing equations presented in Section 2.4, the viscous analog of the Föppl-von Kármán equations, and thus the same equations should govern the behavior of the viscous bridge for moderate displacements.

Consider the case of an initially axisymmetric filament shown schematically in Figure 6-1. $s = x \equiv$ the arc-length coordinate of unstretched filament (Lagrangian). $\bar{s}(s,t) \equiv$ the arc-length coordinate of stretched filament (Eulerian). $\theta(s,t) \equiv$ the angle of inclination of the viscida. $H(s,t) \equiv$ the vertical displacement. $A(s,t) \equiv$ the cross-sectional area. $h(s,t) \equiv$ the diameter. $U(s,t) \equiv$ local filament velocity

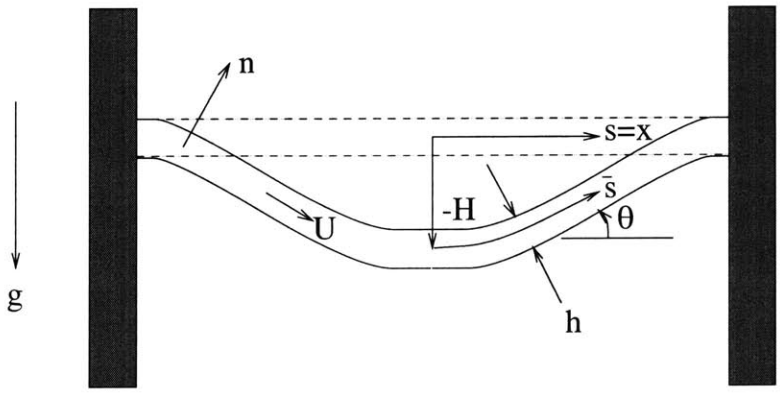

Figure 6-1: Schematic of viscous catenary with relevant variables

tangential to centerline.

$$U = \frac{\partial \bar{s}}{\partial t} \tag{6.1}$$

The tension, $T(s,t)$, is given by

$$T = 3\mu A\dot{\epsilon} = 3\mu A\frac{\partial U(\bar{s},t)}{\partial \bar{s}}, \tag{6.2}$$

where the extensional or Trouton viscosity of the viscida is 3μ. The filament stretch, $\lambda(s,t)$, is

$$\lambda(s,t) = \frac{\partial \bar{s}(s,t)}{\partial s} \tag{6.3}$$

and can be used to express the other quantities in terms of Lagrangian coordinates only:

$$\frac{\partial U(\bar{s},t)}{\partial \bar{s}} = \frac{\partial U(s,t)}{\partial s}\lambda^{-1} \tag{6.4}$$

$$\frac{\partial U(s,t)}{\partial s} = \frac{\partial^2 \bar{s}(s,t)}{\partial s \partial t} = \lambda_t. \tag{6.5}$$

For an incompressible fluid filament, the differential conservation of mass equation can be written as

$$\frac{\partial}{\partial t}(A\lambda) = 0. \tag{6.6}$$

Since the filament is initially unstretched, corresponding to $\lambda = 1$, initially and for all time, $A\lambda = A_0$. The tension can now be written as

$$T(s,t) = 3\mu A\frac{\lambda_t}{\lambda} = 3\mu A\frac{\partial \ln \lambda}{\partial t}. \tag{6.7}$$

6.2 Derivation of governing equations

Love [17] considered the elastic analog to this problem accounting for both bending stiffness and shear forces in addition to tensile forces. Following Love's derivation, the equilibrium of forces and moments can be expressed as

$$\sum F_s = 0 = T_s - w\sin\theta - N\theta_s, \tag{6.8}$$

$$\sum F_n = 0 = T\theta_s - w\cos\theta - N_s, \tag{6.9}$$

and

$$\sum M = 0 = D\theta_{sst} + N, \tag{6.10}$$

where s and n are the local tangent and normal to the center-line respectively, $T(s,t)$ and $N(s,t)$ are the tension and shear force, w is the weight per unit length of the undeformed viscida, $\rho g A\lambda = \rho g A_0$, and $D \equiv 3\mu I$ is the bending stiffness, where $I = 3\pi\mu h^4/64$ is the area moment of inertia of the viscida cross-section, so $D = 3\pi\mu h^4/64$. (6.8), (6.9), and (6.10) are subject to the following boundary conditions: θ must be

an odd function about the midpoint of the span and

$$\theta(s_{wall}, t) = 0. \tag{6.11}$$

Combining (6.8), (6.9), and (6.10) to eliminate T and N yields

$$-w\left(2\sin\theta + \frac{\theta_{ss}\cos\theta}{\theta_s^2}\right) + D\left[\frac{\partial}{\partial s}\left(\frac{\theta_{ssst}}{\theta_s}\right) + \theta_s\theta_{sst}\right] = 0. \tag{6.12}$$

Multiplying (6.12) by $\cos\theta$ and integrating with respect to s yields

$$D\left(\frac{\theta_{ssst}\cos\theta}{\theta_s} + \theta_{sst}\sin\theta\right) + \frac{w\cos^2\theta}{\theta_s} = f_1(t), \tag{6.13}$$

where $f_1(t) = T$ at any point where $\theta = 0$ by comparison to (6.9) and (6.10). Multiplying by $\frac{\theta_s}{\cos^2\theta}$ and integrating again yields

$$D\theta_{sst}\sec\theta + ws = f_1(t)\tan\theta + f_2(t). \tag{6.14}$$

θ is an odd function about the midpoint of the span, so if we measure s from the midpoint, $f_2(t) = 0$ because $\theta_{sst}(0,t) = 0$. Also because θ is odd, $\theta(0,t) = 0$, so $f_1(t) = T(0,t)$ and

$$D\theta_{sst}\sec\theta + ws = T(0,t)\tan\theta \tag{6.15}$$

subject to the boundary conditions

$$\theta(0,t) = 0, \quad \theta(\pm L/2, t) = 0, \tag{6.16}$$

where L is the undeformed length of the filament which satisfies the initial condition $\theta(s,0) = 0$. Then (6.15) and (6.16) describe the evolution of the centerline of the sagging filament once the tension, $T(0,t)$, is known.

As the viscous filament sags, tension arises naturally, and Section 2.4 can be useful. For moderate deflections, the following equations which are analogous to (2.18), (2.16), (2.8), and (2.21) are valid:

$$DH_{xxxxt} = TH_{xx} - w, \tag{6.17}$$

$$\frac{\partial T}{\partial x} = 0, \tag{6.18}$$

and

$$\frac{\partial A}{\partial t} = 0, \tag{6.19}$$

where

$$T(x,t) \equiv 3\mu A[U_x + H_x H_{tx}]. \tag{6.20}$$

Integrating (6.18) yields

$$T(x,t) = T(t) = 3\mu A[U_x + H_x H_{tx}]. \tag{6.21}$$

Integrating (6.17) with this information yields

$$DH_{xxxt} = TH_x - wx + f(t). \tag{6.22}$$

By symmetry, H_{xxxt} and H_x must vanish at $x = 0$ (the midpoint of the viscida), so $f(t) = 0$, and

$$DH_{xxxt} = TH_x - wx \tag{6.23}$$

which is exactly equivalent to (6.15) with $\theta = H_x$ and $x = s$. Integrating (6.21) over half the length of the viscida and noting that $U(x = 0) = 0$ by symmetry and $U(x = L/2) = 0$ because no fluid penetrates the stationary wall leads to

$$T(t) = \frac{6\mu A}{L} \int_0^{L/2} H_x H_{tx} dx, \tag{6.24}$$

where L is constant in this formulation, which can be rewritten as

$$T(t) = \frac{3\mu A}{L} \int_0^{L/2} \frac{\partial H_x^2}{\partial t} dx. \tag{6.25}$$

Combining (6.25) with (6.23) and taking $\theta \equiv H_x$ yields a single integro-differential equation for θ,

$$D\theta_{xxt} - \frac{3\mu A}{L}\theta \int_0^{L/2} \frac{\partial \theta^2}{\partial t} dx = -wx \tag{6.26}$$

with boundary conditions

$$\theta(x = 0) = \theta(x = L/2) = 0. \tag{6.27}$$

The first term in (6.26) represents resistance to bending

$$B \equiv D\theta_{xxt}. \tag{6.28}$$

The second term represents resistance to stretching

$$S \equiv \frac{3\mu A}{L}\theta \int_0^{L/2} \frac{\partial \theta^2}{\partial t} dx, \tag{6.29}$$

where the tension is written as

$$T(t) = 3\mu A \frac{2}{L} \int_0^{L/2} \frac{1}{2} \frac{\partial \theta^2}{\partial t} dx, \tag{6.30}$$

the product of the Trouton viscosity, the cross-sectional area, and the average rate of stretch. The right hand side of (6.26) corresponds to the weight of the filament.

(6.26) can be nondimensionalized using the following scaling:

$$\epsilon \equiv \frac{h}{L}, \quad \tilde{x} \equiv \frac{x}{L}, \quad \tilde{t} \equiv t\frac{2w}{3\pi\mu h}. \tag{6.31}$$

Dropping tildes, (6.26) may be rewritten as

$$\frac{1}{32}\epsilon^3\theta_{xxt} - \epsilon\theta\int_0^{1/2}\frac{1}{2}\frac{\partial\theta^2}{\partial t}dx = -x \tag{6.32}$$

subject to

$$\theta(0,t) = 0, \quad \theta(1/2,t) = 0, \tag{6.33}$$

where

$$B \equiv \frac{1}{32}\epsilon^3\theta_{xxt} \tag{6.34}$$

and

$$S \equiv \epsilon\theta\int_0^{1/2}\frac{1}{2}\frac{\partial\theta^2}{\partial t}dx. \tag{6.35}$$

6.3 Bending solution

If we consider the case where $\theta << 1$, then (6.32) simplifies to

$$\frac{1}{32}\epsilon^3\theta_{xxt} = -x \tag{6.36}$$

with boundary conditions

$$\theta(0,t) = 0, \quad \theta(1/2,t) = 0 \tag{6.37}$$

which can be integrated twice to form

$$\theta_t = -\frac{16\epsilon^3x^3}{3} + xf_3(t) + f_4(t). \tag{6.38}$$

Applying the boundary conditions yields

$$f_3(t) = \tfrac{4\epsilon^3}{3}, \quad f_4(t) = 0 \tag{6.39}$$

so that

$$\theta_t = -\frac{16\epsilon^3x^3}{3} + \frac{4\epsilon^3x}{3}. \tag{6.40}$$

Integrating with respect to time yields

$$\theta(x,t) = -\frac{16\epsilon^3x^3t}{3} + \frac{4\epsilon^3xt}{3}, \tag{6.41}$$

where the constant of integration vanishes because $\theta(x,0) = 0$. Another integration yields the displacement,

$$H(x,t) = \int_{-1/2}^{x}\sin\theta dx \approx \int_{-1/2}^{x}\theta dx = -\frac{4\epsilon^3t}{3}\left[\frac{1}{4} - x^2\right]^2. \tag{6.42}$$

Dimensionally,

$$\theta(x,t) = -\frac{wx^3t}{6D} + \frac{wL^2xt}{24D}, \tag{6.43}$$

and

$$H(x,t) = -\frac{wt}{24D}\left[\left(\frac{L}{2}\right)^2 - x^2\right]^2. \tag{6.44}$$

Trouton solved this problem in 1906 [33] for the rate of sag of a viscous bar resting on two supports separated by a gap with boundary conditions requiring that the internal moment vanish at the ends of the bar (equivalent to $\theta_{xt}(\pm L/2, t) = 0$). He found that the center-point of the bar sags at a rate of $\frac{5wL^4}{384D}$. For the boundary conditions presented here, the center-point of the bar sags at a rate of $\frac{wL^4}{384D}$, matching results produced by Tuck et al. [34].

6.4 Stretching solution

After the initial phase of deformation when bending resistance controls the slumping, stretching becomes significant. To estimate the time at which stretching begins to play a role, I compare the relative magnitudes of S and B in (6.32) using the bending solution, (6.41). Plugging (6.41) into (6.34) and (6.35) yields $B = -x$ and

$$S = -\frac{64t^2}{2835\epsilon^8}\left(x - 4x^3\right). \tag{6.45}$$

The effect of stretching becomes significant when S and B are of comparable magnitude,

$$-x \approx -\frac{64t^2}{2835\epsilon^8}\left(x - 4x^3\right). \tag{6.46}$$

This occurs when

$$t \approx \epsilon^4\sqrt{\frac{2835}{64(1-4x^2)}} \tag{6.47}$$

and happens earliest at $x = 0$ when

$$t \approx \epsilon^4\sqrt{\frac{2835}{64}} \tag{6.48}$$

Dimensionally,

$$t \sim \frac{\mu h^5}{wL^4} \tag{6.49}$$

so that for a filament with $L = 0.1m$, $h = 0.01m$, $\rho = 1000kg/m^3$, and $\mu = 1000Pa\cdot s$, stretching becomes significant when $t \sim 0.001s$.

In an ever shrinking boundary layer near the wall, bending resistance remains important, and the curvature of the viscida becomes high in order to conform to the zero slope boundary condition at the wall. The outer solution, where stretching is the dominant factor outside the confines of the boundary layer, can be closely

approximated by (6.32) without B,

$$\epsilon\theta \int_0^{1/2} \frac{1}{2}\frac{\partial\theta^2}{\partial t} dx = x. \tag{6.50}$$

The outer solution to (6.50) exists in the form

$$\theta = \sqrt[3]{\frac{72}{\epsilon}} x t^{1/3} \tag{6.51}$$

or, dimensionally,

$$\theta = \sqrt[3]{\frac{12w}{\mu A L^2}} x t^{1/3}. \tag{6.52}$$

In the stretching dominated regime, the viscida will sag at a rate proportional to $t^{1/3}$, much more slowly than in the bending dominated regime where the viscida sags at a rate proportional to t. In fact, (6.51) not only satisfies (6.50), it also satisfies (6.32) without the wall boundary condition and constitutes an outer solution to the problem. It must be matched to the inner solution corresponding to the bending dominated boundary layer near the wall.

6.4.1 Bending boundary layer

This section examines how the extent of the bending boundary layer near the wall changes with time. The viscida obeys (6.32). First note that the stretching term contains an integral spanning half of the length of the filament. The departure of the solution in the boundary layer from the outer solution will not produce a meaningful contribution to the integral because of the comparatively small size of the boundary layer. Thus, using the outer solution, (6.51), to evaluate the integral provides a good approximation resulting in the modified equation

$$\frac{1}{32}\epsilon^3 \theta_{xxt} - \sqrt[3]{\frac{\epsilon}{72}} t^{-1/3}\theta = -x. \tag{6.53}$$

Over the width of the boundary layer, θ changes rapidly from the outer solution value to zero, the value at the wall. Within the boundary layer, the bending term achieves the same order of magnitude as the forcing term, $-x$. After rewriting the bending term as

$$\frac{1}{32}\epsilon^3 \frac{\partial}{\partial t}\left(\theta_{xx}\right), \tag{6.54}$$

estimate

$$\theta_{xx} \sim \frac{\theta_{wall} - \theta_{outer}(x_{wall})}{\delta^2(t)}, \tag{6.55}$$

where $\delta(t)$ is the width of the boundary layer, $\theta_{wall} = 0$, and

$$\theta_{outer}(x_{wall}) = \frac{1}{2}\sqrt[3]{\frac{72}{\epsilon}} t^{1/3}. \tag{6.56}$$

Equating the magnitudes of the bending term and the forcing term yields

$$-\frac{1}{32}\epsilon^3\frac{\partial}{\partial t}\left(\frac{\theta_{outer}(x_{wall})}{\delta^2(t)}\right) \sim -\frac{1}{2} \tag{6.57}$$

or, on integrating with respect to time and substituting in (6.56),

$$\frac{1}{64}\sqrt[3]{\frac{72}{\epsilon}}\epsilon^3\left(\frac{t^{1/3}}{\delta^2(t)}\right) \sim \frac{t}{2} + C, \tag{6.58}$$

where C is an arbitrary constant which must vanish because as $t \to 0$, δ does not vanish, leaving $C \sim 0$. Dropping numerical prefactors and solving (6.58) for δ yields

$$\delta \sim \epsilon^{4/3}t^{-1/3} \tag{6.59}$$

or dimensionally

$$\delta \sim \left(\frac{\mu}{wL}\right)^{1/3} h^{5/3}t^{-1/3} \tag{6.60}$$

Thus the bending boundary layer should contract with time shrinking as $t^{-1/3}$. The analogous elastic bending boundary layer is present is Love's solution [17] with

$$\delta_{elastic} \sim \left(\frac{G}{wL}\right)^{1/3} h^{5/3}, \tag{6.61}$$

where G is the elastic shear modulus which has replaced μ/t in (6.60).

6.5 Breakdown of slender-body theory

The equations presented hitherto rely on the Trouton extensional viscosity and a simple bending stiffness. Both of these approximations require making the assumption that cross-sectional planes in the undeformed viscida remain planes in the deformed viscida. Both approximations are violated in a small region adjacent to the wall due to the no-slip velocity boundary condition on the wall that does not allow the wetted wall area to shrink as the viscida stretches. This assumption taken together with (6.6) would imply that λ always remains one at the wall which, together with (6.7), suggests that the tension at the wall will always be zero. In reality, the extensional viscosity becomes infinite at the wall allowing the presence of a finite tension with no reduction in area. An extensional viscosity boundary layer such as this one is considered by Stokes, Tuck, and Schwartz in their discussion of the pinch off of a falling viscous fluid drop [35]. They suggest that the extensional viscosity boundary layer extends from the wall a distance approximately equal to the thickness of the viscida and the effect falls off as $1/x^2$. They suggest the following "composite empirical expression" for the Trouton viscosity:

$$3\mu\left[1 + \frac{1}{32}\left(\frac{h}{x}\right)^2\right]. \tag{6.62}$$

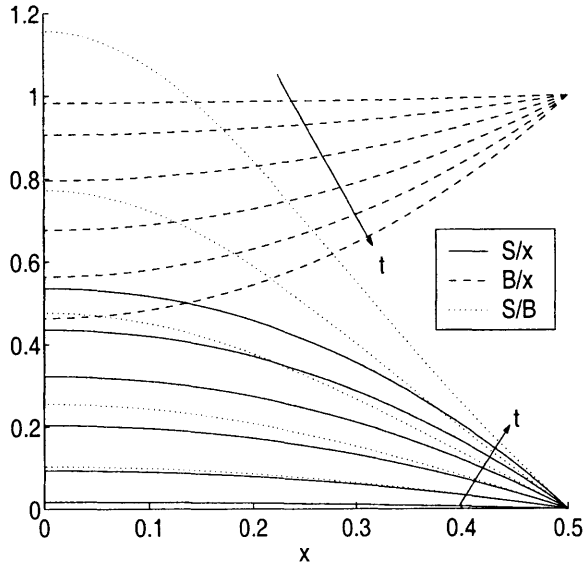

Figure 6-2: Relative importance of bending (B) and stretching (S) as defined by (6.34) and (6.35) at times just up to the emerging dominance of stretching. The curves represent time snapshots in increments of 2×10^{-7}. $\epsilon = 1/50$.

The analogous bending stiffness boundary layer will be of similar extent covering the region in which the cross-sectional planes of the viscida become curved during deformation. The effect of the bending stiffness boundary layer is incorporated through the boundary condition that requires the slope of the viscida to vanish at the wall.

6.6 Numerical solutions

To account for both bending and stretching, (6.32) can be solved using a spectral collocation method based on Chebyshev polynomials [32]. This solution confirms that at early times, the viscida sags at the bending controlled rate proportional to t and, at later times, at the slower stretching controlled rate proportional to $t^{1/3}$. The same solution shows that the boundary layer size shrinks at a rate proportional to $t^{-1/3}$. Appendix F elaborates on the details of the implementation of the numerical scheme.

Figure 6-2 illustrates the relative importance of B and S for $\epsilon = 1/50$. For this slenderness ratio, (6.48) predicts that bending will outstrip stretching for $t > 1.1 \times 10^{-6}$, an estimate very close to the results shown in Figure 6-2. Figure 6-3 shows the evolution of the viscida as stretching asserts itself. For $t < 10^{-7}$, the bending solution presents an accurate picture of the viscida.

Figure 6-4 shows the behavior of the viscida at later times after stretching has become dominant over most of the span. The stretching solution's exaggeration of the displacement stems largely from the gross over-estimation of the angle in the boundary layer as seen in the left-hand plot of Figure 6-4. However, Figure 6-5 shows that the growth rate of the full solution approaches the one-third power law growth rate of

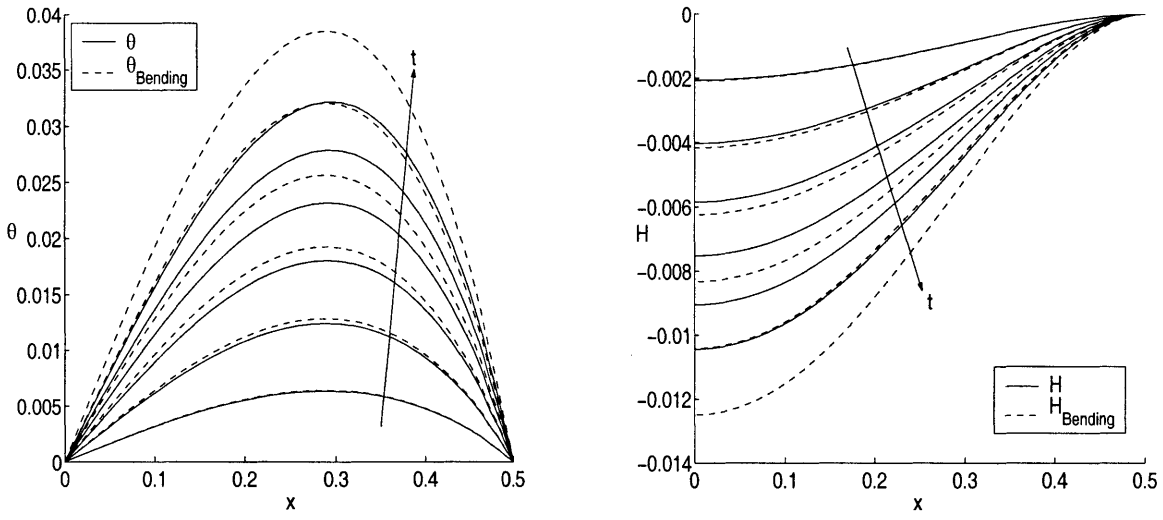

Figure 6-3: Evolution of the viscida just as stretching begins to emerge as a contributing factor. $\theta = H_x$ is the solution of (6.32). $\theta_{Bending}$ is given by (6.41), and $H_{Bending}$ is given by (6.42). The curves represent time snapshots in increments of 2×10^{-7}. $\epsilon = 1/50$.

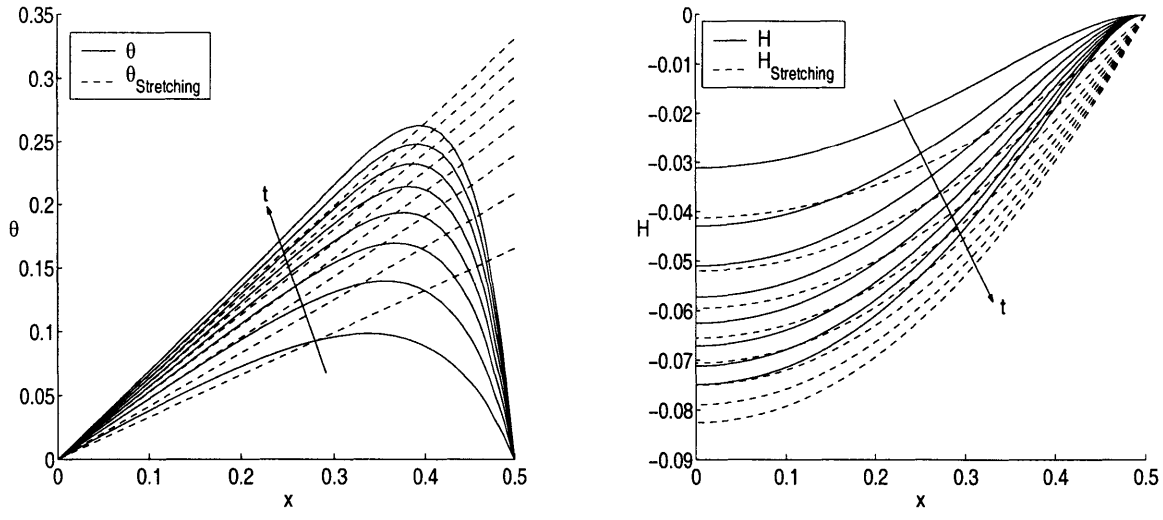

Figure 6-4: Evolution of the viscida after stretching has dominated bending over most of the filament. $\theta = H_x$ is the solution of (6.32). $\theta_{Stretching}$ is given by (6.51), and $H_{Stretching} = \int_{-1/2}^{x} \theta_{Stretching} dx$. The curves represent time snapshots in increments of 10^{-5}. $\epsilon = 1/50$.

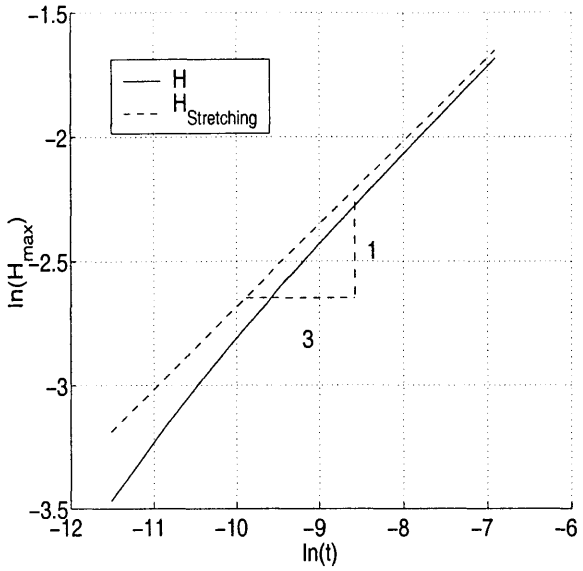

Figure 6-5: Sag of the viscida after stretching has dominated bending over most of the filament. $H_{max} = -H(0,t)$ is the maximum displacement of the viscida. $H_{Stretching} = \int_{-1/2}^{x} \theta_{Stretching} dx$, where $\theta_{Stretching}$ is given by (6.51). $\epsilon = 1/50$.

the stretching solution. Figure 6-6 contains a plot of the contraction of the bending boundary layer extent over time illustrating the $t^{-1/3}$ dependence predicted by (6.59). Figure 6-7 shows the dependence of the boundary layer size on the slenderness of the filament and confirms the $\epsilon^{4/3}$ dependence predicted by (6.59).

6.7 Late time behavior

At comparatively very large times, the viscida will pinch off in finite time from the extensional viscosity boundary region near the wall in much the manner suggested for droplet pinch off by Stokes et al. [35]. When the filament has sagged sufficiently, the portion of the filament extending from just outside of the bending boundary layer near the wall to some point a considerable way along the filament will hang nearly vertically with negligible curvature. The behavior of the filament at this stage follows the limit of (6.8) when $\theta \to \pi/2$ and $\theta_s \to 0$:

$$T_s = w \tag{6.63}$$

where

$$w = \rho g A_0(s). \tag{6.64}$$

Integrating (6.63) once from some point, s_1, near the bottom of the vertical region to an arbitrary point in the vertical region, s, leads to

$$T(s,t) = \rho g \int_{s_1}^{s} A_0(s) ds + f(t). \tag{6.65}$$

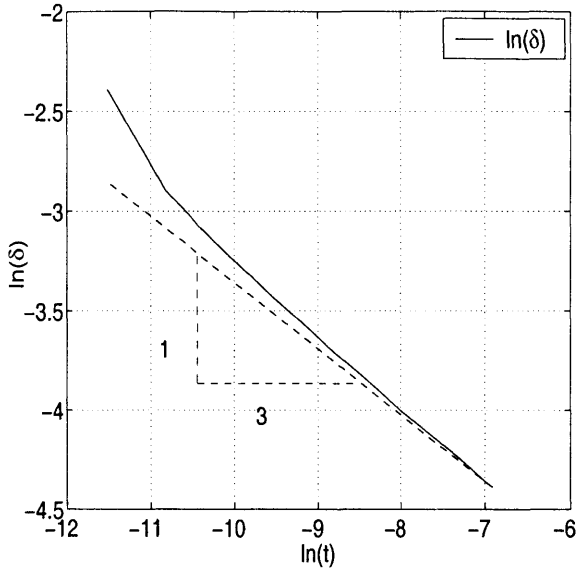

Figure 6-6: Time dependence of the bending boundary layer extent. The dashed line indicates a time dependence of $t^{-1/3}$. $\epsilon = 1/50$.

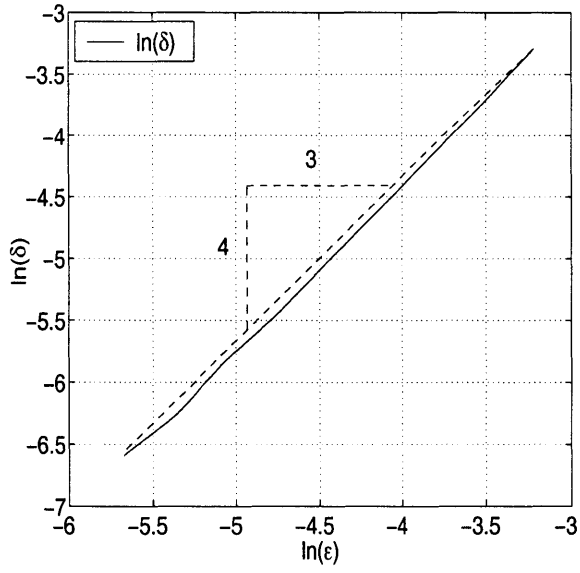

Figure 6-7: Variation of the bending boundary layer size with slenderness ratio at $t = 8 \times 10^{-4}$. The dashed line indicates a slenderness ratio dependence of $\epsilon^{4/3}$.

At $s = s_1$, $T = T(s_1, t)$, so $f(t) = T(s_1, t)$. At $s = s_1$, the tension must by symmetry support half the weight of the strand below s_1, so

$$T(s_1, t) = \rho g \int_0^{s_1} A_0(s) ds \tag{6.66}$$

and

$$T(s, t) = \rho g \int_0^{s} A_0(s) ds. \tag{6.67}$$

Utilizing the constitutive relation, (6.7), and noting that due to (6.6),

$$A\lambda_t = \frac{\partial}{\partial t}(A\lambda) - A_t\lambda = -A_t\lambda, \tag{6.68}$$

$$T(s, t) = -3\mu A_t(s, t) = \rho g \int_0^{s} A_0(s) ds. \tag{6.69}$$

Integrating in time yields

$$A(s, t) = -\frac{\rho g t}{3\mu} \int_0^{s} A_0(s) ds + f(s). \tag{6.70}$$

$A(s, 0) = A_0(s)$, so $f(s) = A_0(s)$ and

$$A(s, t) = -\frac{\rho g t}{3\mu} \int_0^{s} A_0(s) ds + A_0(s). \tag{6.71}$$

To determine when and where the viscida will break, set $A(s, t^*) = 0$ in (6.71):

$$t^*(s) = \frac{3\mu A_0(s)}{\rho g \int_0^s A_0(s)}. \tag{6.72}$$

The filament will break at the position $s = s^*$ that minimizes $t^*(s)$. These results are completely analogous to those of Stokes et al. [35]. The denominator of (6.72) strictly increases with increasing s. Thus, if $A_0(s)$ does not vary with s or decreases with s, the minimum t^* will occur just outside of the extensional viscosity boundary layer and wall region bending boundary layer at a distance $O(h)$ from the wall. Examination of (6.8) shows that from the time that stretching begins to dominate bending and therefore $N \approx 0$,

$$T_s = w \sin\theta. \tag{6.73}$$

This will occur during the time regime described by (6.26) during which the thickness of the filament experiences no appreciable change. Thus, to a good approximation, the filament enters the regime described by (6.73) with a uniform cross-sectional area. Since in the region $0 < s < L/2$, $0 < \theta < \pi/2$ and $w > 0$, $T_s > 0$. This means that the maximum tension will occur near the wall just outside of the bending boundary layer. Since the rate at which the viscida pinches down is proportional to the tension, (6.69), the viscida will slim most rapidly in the region near the wall during the entire time span from the uniform cross-sectional area filament to the nearly vertical filament.

Thus, in fact, $A_0(s)$ for the late-time problem will have a minimum near the wall, and the viscida will break there.

6.7.1 Exact outer solution for the stretching region

In the stretching region, even beyond the time for which the small angle approximation is valid, $N = 0$, and the following reduced forms of (6.8) and (6.9) govern the evolution of the viscida:

$$T_s = w \sin\theta \tag{6.74}$$

and

$$T\theta_s = w \cos\theta \tag{6.75}$$

subject to the constitutive equation

$$T = -3\mu A_t. \tag{6.76}$$

Substitution of (6.76) into (6.74) and (6.75) yields

$$-3\mu A_{st} = w \sin\theta \tag{6.77}$$

and

$$-3\mu A_t \theta_s = w \cos\theta. \tag{6.78}$$

(6.78) when multiplied by $\cos\theta$ can be rewritten as

$$-3\mu A_t \frac{d}{ds}(\sin\theta) = w(1 - \sin^2\theta). \tag{6.79}$$

Rearranging (6.77) as

$$-\frac{3\mu}{w} A_{st} = \sin\theta \tag{6.80}$$

and substituting into (6.79) yields

$$3\mu A_t \left[\frac{3\mu}{w} A_{sst}\right] = w\left[1 - \frac{9\mu^2}{w^2} A_{st}^2\right] \tag{6.81}$$

or

$$A_t A_{sst} + A_{st}^2 = \frac{w^2}{9\mu^2}. \tag{6.82}$$

(6.82) can be rewritten

$$\frac{\partial}{\partial s}(A_t A_{st}) = \frac{w^2}{9\mu^2} \tag{6.83}$$

and then integrated to form

$$A_t A_{st} = \frac{w^2 s}{9\mu^2} + f(t) \tag{6.84}$$

or

$$\frac{1}{2}\frac{\partial}{\partial s}\left(A_t^2\right) = \frac{w^2 s}{9\mu^2} + f(t). \tag{6.85}$$

At $s = 0$, $\frac{\partial}{\partial s}\left(A_t^2\right) = 0$ by symmetry. It follows that $f(t) = 0$ and

$$\frac{\partial}{\partial s}\left(A_t^2\right) = \frac{2w^2 s}{9\mu^2}. \tag{6.86}$$

Integrating (6.86) leads to

$$A_t^2 = \frac{w^2 s^2}{9\mu^2} + f_2(t) \tag{6.87}$$

or

$$A_t = -\sqrt{\frac{w^2 s^2}{9\mu^2} + f_2(t)}. \tag{6.88}$$

Differentiating shows

$$A_{st} = \frac{-\frac{w^2 s}{9\mu^2}}{\sqrt{\frac{w^2 s^2}{9\mu^2} + f_2(t)}}. \tag{6.89}$$

(6.89) taken together with (6.80) leads to

$$\sin\theta = \frac{\frac{ws}{3\mu}}{\sqrt{\frac{w^2 s^2}{9\mu^2} + f_2(t)}} \tag{6.90}$$

which represents the outer solution condition that must be matched to θ from the bending boundary layer solution. For this solution, it would not suffice to say that the slope of the filament near the wall is approximately $\pi/2$ since that would lead to $f_2(t) = 0$ and $\theta(s) = \pi/2$, and by symmetry, it must be the case that $\theta(0) = 0$.

6.8 Sagging of sheets

If one wishes to consider the sag of a planar sheet, the only changes lie in the Trouton viscosity which goes from 3μ to 4μ to account for the fact that no transverse stretching can occur in the planar case, the moment of inertia which goes from $\frac{\pi h^4}{64}$ to $\frac{h^3}{12}$ (keeping in mind that planar quantities are per unit length in the direction of uniformity), and A which goes from $\frac{\pi}{4}h^2$ to h.

Chapter 7

Conclusion

In the spirit of the analogy between the behavior of viscous Newtonian fluids and static Hookean solids formalized by Stokes and Rayleigh for bulk materials, this thesis explored extensions of the analogy to slender bodies such as filaments and films of viscous fluids. Slender viscous bodies have not been nearly as well explored as their elastic brethren. Interest was spurred in the late 1950s and 1960s by geological applications and soon spread to the general fluid mechanics community. Flows involving slender viscous bodies have drawn great interest recently because they commonly arise in manufacturing processes.

This thesis has striven to explore these fascinating fluid phenomena in the context of their elastic analogs. The principal difference between slender viscous bodies and their elastic counterparts is the presence of significant surface tension in fluids. In order to explore the analogy, this work considers viscous scenarios with and without important surface tension effects. The general equations for the evolution of a folding viscous sheet are developed from the Stokes equations for highly viscous fluid flow following the example of Buckmaster et al. [8] and Howell [12]. The two-dimensional case of layer-parallel compression is considered in order to shed light on the general stability behavior of the equations.

The thesis focused on three particular problems, wrinkling of a sheared annular film, wrinkling of a sheared rectilinear film, and sagging of a horizontal filament. Though many viscous folding problems have been considered over the years, the first two problems in this thesis represent the first truly three-dimensional viscous folding problems solved. All three of these scenarios exhibit very complex nonlinear behavior even though the material properties are perfectly linear and no inertia is considered. The complexities arise from the geometries which contain multiple length scales and dynamic free boundaries.

The elastic analog to the annular problem was studied by Dean in 1924 [11]. Dean clamped an elastic sheet in an annular geometry and investigated the instability of the sheet under pure shear. Experiments were performed for the case of viscous annular sheet shearing in order to quantify the behavior of the system and serve as a validation of the model equations and their predictions of the critical shear rate for wrinkling and the most unstable number of ripples as well as the resulting mode shape. In Chapter 3, the experiments are described in detail. The most unstable

modes, as expressed by the experimental sheet deformations, compared well, but not perfectly, with the results of linear stability theory which predicts that the instability arises in a supercritical pitchfork bifurcation in which the amplitude at true onset is zero. Due to the difficulty of measuring very small deviations in the shape of the sheet, the instability is only observed when the amplitude becomes detectably large. The experimental data can only characterize this regime slightly beyond onset. Utilizing the linear theory (which is only strictly valid for infinitesimal amplitudes but represents a close approximation for small amplitudes at which nonlinear effects remain small) to model the regime measured in the experiments showed excellent agreement between theory and experiment. These results represent the first successful model for a three-dimensional long wavelength instability in a viscous sheet.

The same model is applied in Chapter 4 to the rectilinear Couette geometry which can be considered a limiting case of the annular geometry in which the radius of the annulus is very large compared to the gap width. Southwell and Skan considered this limiting case of the elastic problem in 1924 [28], the same year that Dean published his annular study [11]. In contrast to standard planar Couette channel flow which is stable for all shear rates, the presence of the free surfaces and slender geometry in this scenario renders the flow unstable even to infinitesimal shear rates. The instability to infinitesimal shear rates, exhibited by the annular sheet as well, may at first seem to be at odds with the analogy since the corresponding elastic problems show finite critical shear stresses necessary to produce the instability. The nature of the viscous instability is, in fact, perfectly in harmony with the analogy. The analogy specifies that displacements in the elastic medium be replaced by velocities in the viscous one. An elastic sheets is stable below the critical shear rate because its bending stiffness provides resistance to folding that prevents the deformation from occurring. In a viscous sheet, the same bending stiffness provides resistance to *rates* of deformation and, hence, does not hold the sheet in its planar shape, but slows the deviation instead. Linear stability analysis of the viscous sheet equations yielded the dispersion relation and the most unstable mode. It should be noted that in contrast to layer-parallel compression, the rectilinear and annular sheared sheets are not subject to thickening at small amplitudes of deformation due to the balance of tension and compression resulting from shear; hence, the concerns of thickening taking place faster than folding [22] do not apply to these scenarios.

The elastic analog to the third problem, the sagging filament, dates back to the end of the seventeenth century when Jacob Bernoulli issued a challenge to find the shape of a chain hung between two points. His brother Johann, together with Leibniz and Huygens, solved for the resulting form [20]. Love considered the effects of elastic stretching of the filament as well as its bending stiffness [17]. Here I have examined the viscous catenary problem incorporating bending and stretching as Love did. This is the inverse of the other two problems considered. In the case of the catenary, the primary forcing is out-of-plane, and in-plane forces result. In the sheared sheet, in-plane forces led to out-of-plane forces and folding. The observation that the equations developed with the sheared sheets in mind were derived utilizing a velocity scaling that was strictly kinematic allowed them to be applied to the sagging viscida as well despite the reversal of the dynamic causality. The behavior of the viscous catenary was

explored through three regimes of development. As an initially horizontal filament begins to sag, resistance to bending governs the development. Once appreciable deformation has occurred, naturally arising tensile stresses become important and resistance to stretching then controls the evolving shape of the viscida except in bending boundary layers near the wall where bending remains important in an ever shrinking region. At very late times, the behavior of the filament resembles droplet pinch-off from two necks.

These three problems serve as an emphatic assertion that the viscous-elastic analogy holds in slender members just as it does in the bulk. In each of these three problems, not only do the shapes of the deformed viscous filaments and sheets share all of the characteristics of their elastic counterparts; the forces present in each set of scenarios also match. The only differences arise due to capillary forces and the replacement of strains with strain rates as required by the analogy. There is no shortage of well examined plate, shell, and beam problems in elasticity. The elasticity literature should provide a well endowed mine of analogous viscous problems to examine in the future.

Appendix A

Derivation of model equations

The Stokes equations describe the behavior of a fluid in the limit of vanishingly small Reynolds number (here in Cartesian coordinates):

$$P_x = \mu(u_{xx} + u_{yy} + u_{zz}), \tag{A.1}$$
$$P_y = \mu(v_{xx} + v_{yy} + v_{zz}), \tag{A.2}$$
$$P_z = \mu(w_{xx} + w_{yy} + w_{zz}), \tag{A.3}$$

where P is the pressure, and u, v, and w are the velocity components in the x, y, and z directions. The continuity equation ensures conservation of mass:

$$u_x + v_y + w_z = 0. \tag{A.4}$$

The top and bottom of the sheet must obey a kinematic surface condition,

$$w|_{z=H\pm\frac{1}{2}h} = \frac{D}{Dt}(H \pm \frac{1}{2}h) = H_t \pm \frac{1}{2}h_t + (H_x \pm \frac{1}{2}h_x)u + (H_y \pm \frac{1}{2}h_y)v, \tag{A.5}$$

where H is the z-coordinate of the center surface of the sheet, and h is the thickness of the sheet. The top and bottom surfaces must also satisfy a dynamic traction condition. The tractions on the surfaces of the layer are a result of ambient pressure and surface tensions of the interfaces. The ambient pressure in the air above the fluid sheet can, without loss of generality, be considered zero. The ambient pressure below will be determined by hydrostatic pressure variations in the underlying fluid, $P^- = \rho^- gH$, where ρ^- is the density of the underlying fluid, and g is acceleration due to gravity. The free surface condition can be expressed as

$$\underline{\underline{\sigma}} \cdot \vec{n} = \vec{T}, \tag{A.6}$$

where $\underline{\underline{\sigma}}$ is the stress tensor,

$$\underline{\underline{\sigma}} = \begin{pmatrix} -P + 2\mu u_x & \mu(u_y + v_x) & \mu(u_z + w_x) \\ \mu(u_y + v_x) & -P + 2\mu v_y & \mu(v_z + w_y) \\ \mu(u_z + w_x) & \mu(v_z + w_y) & -P + 2\mu w_z \end{pmatrix}, \tag{A.7}$$

$\vec{n}$ is an outward normal to the surface,

$$\vec{n} = \pm[-(H_x \pm \frac{1}{2}h_x), -(H_y \pm \frac{1}{2}h_y), 1]^T, \tag{A.8}$$

and $\vec{T}$ is the traction on the surface. The edges of the sheet satisfy a no-slip condition so that the velocities u, v, and w match the velocity of the walls.

Following Buckmaster, Nachman, and Ting[8], the variables in the equation can be scaled in a manner consistent with buckling type motion to generate an equation wherein all of the scaled variables are of the same order. The scaled variables are indicated by hats, and the scaling utilizes a characteristic in-plane length-scale of the sheet, L, a characteristic out-of-plane velocity, U, and a slenderness ratio, ϵ, characterizing the ratio of the thickness of the sheet to L, where $\epsilon << 1$. The variables scale as follows:

$$\begin{array}{lll} x = \hat{x}L, & y = \hat{y}L, & z = \hat{z}\epsilon L, \\ u = \hat{u}\epsilon U, & v = \hat{v}\epsilon U, & w = \hat{w}U, \\ P = \hat{P}\mu\epsilon\frac{U}{L}, & & t = \hat{t}\epsilon\frac{L}{U}. \end{array} \tag{A.9}$$

Howell [12] demonstrated that by plugging these scaled variables into the governing equations and representing the scaled variables in perturbation series (e.g. $\hat{u} = \hat{u}^{(0)} + \epsilon^2\hat{u}^{(1)} + \epsilon^4\hat{u}^{(2)}\cdots$), the equations could be solved order by order to generate a set of equations describing the evolution of the geometry of the sheet. What follows demonstrates that the final equations arrived at by Howell can be derived in a more physically intuitive manner by solving the leading order equations and balancing forces and moments in the sheet. Ribe [24] does a similar physically motivated derivation for one-dimensional initially curved sheets.

Since all variables now considered are scaled, the hat notation will be dropped for convenience. The scaled equations and boundary conditions follow:

Continuity:

$$\epsilon^2 u_x + \epsilon^2 v_y + w_z = 0, \tag{A.10}$$

Stokes:

$$\epsilon^2 P_x = \epsilon^2 u_{xx} + \epsilon^2 u_{yy} + u_{zz}, \tag{A.11}$$

$$\epsilon^2 P_y = \epsilon^2 v_{xx} + \epsilon^2 v_{yy} + v_{zz}, \tag{A.12}$$

$$\epsilon^2 P_z = \epsilon^2 w_{xx} + \epsilon^2 w_{yy} + w_{zz}, \tag{A.13}$$

Kinematic surface condition at $z = H \pm \frac{1}{2}h$:

$$w|_{z=H\pm\frac{1}{2}h} = H_t \pm \frac{1}{2}h_t + \epsilon^2(H_x \pm \frac{1}{2}h_x)u + \epsilon^2(H_y \pm \frac{1}{2}h_y)v, \tag{A.14}$$

Traction surface condition at $z = H \pm \frac{1}{2}h$:

$$\epsilon^2(-P + 2u_x)(H_x + \frac{1}{2}h_x) + \epsilon^2(u_y + v_x)(H_y + \frac{1}{2}h_y) - (u_z + w_x) =$$

$$\epsilon^2\frac{\Gamma^+}{3}\nabla^2(H+\frac{1}{2}h)(H_x+\frac{1}{2}h_x), \tag{A.15}$$

$$\epsilon^2(-P+2u_x)(H_x-\frac{1}{2}h_x)+\epsilon^2(u_y+v_x)(H_y-\frac{1}{2}h_y)-(u_z+w_x)=$$
$$-\epsilon^2\frac{\Gamma^-}{3}\nabla^2(H-\frac{1}{2}h)(H_x-\frac{1}{2}h_x)+\epsilon^2\frac{G}{3}H(H_x-\frac{1}{2}h_x), \tag{A.16}$$

$$\epsilon^2(u_y+v_x)(H_x+\frac{1}{2}h_x)+\epsilon^2(-P+2v_y)(H_y+\frac{1}{2}h_y)-(v_z+w_y)=$$
$$\epsilon^2\frac{\Gamma^+}{3}\nabla^2(H+\frac{1}{2}h)(H_y+\frac{1}{2}h_y), \tag{A.17}$$

$$\epsilon^2(u_y+v_x)(H_x-\frac{1}{2}h_x)+\epsilon^2(-P+2v_y)(H_y-\frac{1}{2}h_y)-(v_z+w_y)=$$
$$-\epsilon^2\frac{\Gamma^-}{3}\nabla^2(H-\frac{1}{2}h)(H_y-\frac{1}{2}h_y)+\epsilon^2\frac{G}{3}H(H_y-\frac{1}{2}h_y), \tag{A.18}$$

$$\epsilon^2(u_z+w_x)(H_x+\frac{1}{2}h_x)+\epsilon^2(v_z+w_y)(H_y+\frac{1}{2}h_y)-(-\epsilon^2P+2w_z)=$$
$$-\epsilon^2\frac{\Gamma^+}{3}\nabla^2(H+\frac{1}{2}h), \tag{A.19}$$

$$\epsilon^2(u_z+w_x)(H_x-\frac{1}{2}h_x)+\epsilon^2(v_z+w_y)(H_y-\frac{1}{2}h_y)-(-\epsilon^2P+2w_z)=$$
$$\epsilon^2\frac{\Gamma^-}{3}\nabla^2(H-\frac{1}{2}h)-\epsilon^2\frac{G}{3}H, \tag{A.20}$$

where

$$G\equiv 3\frac{\rho^- gL^2}{\mu U} \tag{A.21}$$

and

$$\Gamma^\pm\equiv 3\frac{\gamma^\pm}{\mu U}. \tag{A.22}$$

Consider each of the variables in the equations and boundary conditions to be represented by a perturbation series in the small parameter, ϵ^2, so that

$$u = u^{(0)}+\epsilon^2u^{(1)}+\epsilon^4u^{(2)}\cdots, \tag{A.23}$$
$$v = v^{(0)}+\epsilon^2v^{(1)}+\epsilon^4v^{(2)}\cdots, \tag{A.24}$$
$$w = w^{(0)}+\epsilon^2w^{(1)}+\epsilon^4w^{(2)}\cdots, \tag{A.25}$$
$$P = P^{(0)}+\epsilon^2P^{(1)}+\epsilon^4P^{(2)}\cdots, \tag{A.26}$$
$$H = H^{(0)}+\epsilon^2H^{(1)}+\epsilon^4H^{(2)}\cdots, \tag{A.27}$$
$$h = h^{(0)}+\epsilon^2h^{(1)}+\epsilon^4h^{(2)}\cdots. \tag{A.28}$$

Substitute the perturbation series representations of the variables into the equations and boundary conditions. Since $\epsilon << 1$, the terms proportional to ϵ^2 are much smaller than the other terms in the equations and to leading order can be ignored (Equivalently, equate all terms of $O(\epsilon^0)$). Thus, the leading order governing equations and boundary conditions follow:

Continuity:

$$w_z^{(0)} = 0 \tag{A.29}$$

Stokes:

$$u_{zz}^{(0)} = 0 \tag{A.30}$$
$$v_{zz}^{(0)} = 0 \tag{A.31}$$
$$w_{zz}^{(0)} = 0 \tag{A.32}$$

Kinematic surface condition at $z = H \pm \frac{1}{2}h$:

$$w^{(0)}\Big|_{z=H\pm\frac{1}{2}h} = H_t^{(0)} \pm \frac{1}{2}h_t^{(0)} \tag{A.33}$$

Traction surface condition at $z = H \pm \frac{1}{2}h$:

$$(u_z^{(0)} + w_x^{(0)})\Big|_{z=H\pm\frac{1}{2}h} = 0 \tag{A.34}$$
$$(v_z^{(0)} + w_y^{(0)})\Big|_{z=H\pm\frac{1}{2}h} = 0 \tag{A.35}$$
$$w_z^{(0)}\Big|_{z=H\pm\frac{1}{2}h} = 0. \tag{A.36}$$

(A.29) shows that w depends only upon x,y, and t. This result combined with the kinematic surface condition demonstrates that

$$h_t^{(0)} = 0 \tag{A.37}$$

and

$$w^{(0)}(x, y, t) = H_t^{(0)}. \tag{A.38}$$

(A.30) and (A.31) show that neither $u_z^{(0)}$ nor $v_z^{(0)}$ depends on z. The dynamic boundary conditions, (A.34) and (A.35), then show that

$$u_z^{(0)} = -H_{tx}^{(0)} \tag{A.39}$$
$$v_z^{(0)} = -H_{ty}^{(0)}. \tag{A.40}$$

Integrating (A.39) and (A.40) with respect to z gives

$$u^{(0)} = -zH_{tx}^{(0)} + f_1(x, y, t) \tag{A.41}$$
$$v^{(0)} = -zH_{ty}^{(0)} + f_2(x, y, t). \tag{A.42}$$

Let us define two new variables, $\bar{u}$ and $\bar{v}$, as the depth-averaged velocities in the x and y directions, respectively.

$$\bar{u}(x, y, t) \equiv \frac{1}{h}\int_{H-\frac{1}{2}h}^{H+\frac{1}{2}h} u^{(0)} dz$$

$$= -H^{(0)}H^{(0)}_{tx} + f_1(x,y,t) \tag{A.43}$$

$$f_1(x,y,t) = \bar{u} + H^{(0)}H^{(0)}_{tx} \tag{A.44}$$

$$u^{(0)} = \bar{u} + (H^{(0)} - z)H^{(0)}_{tx} \tag{A.45}$$

$$\bar{v}(x,y,t) \equiv \frac{1}{h}\int_{H-\frac{1}{2}h}^{H+\frac{1}{2}h} v^{(0)}dz$$

$$= -H^{(0)}H^{(0)}_{ty} + f_2(x,y,t) \tag{A.46}$$

$$f_2(x,y,t) = \bar{v} + H^{(0)}H^{(0)}_{ty} \tag{A.47}$$

$$v^{(0)} = \bar{v} + (H^{(0)} - z)H^{(0)}_{ty}. \tag{A.48}$$

Now, in order to evaluate the pressure, let us examine the order ϵ^2 correction to the equations. All terms proportional to ϵ^4 or higher powers of ϵ can be ignored as small compared to the remaining terms. The resulting set of equations has terms proportional to ϵ^2 and terms with no dependence on ϵ. The terms with no ϵ dependence cancel out because they satisfy the leading order equations. Dividing the remaining equations by ϵ^2 and assuming that G and $\Gamma^{\pm}$ are small compared to unity yields, among others, the following equations and boundary condition:

$$w^{(1)}_z = -u^{(0)}_x - v^{(0)}_y \tag{A.49}$$

$$w^{(1)}_{zz} = -w^{(0)}_{xx} - w^{(0)}_{yy} + P^{(0)}_z \tag{A.50}$$

$$2w^{(1)}_z\Big|_{z=H\pm\frac{1}{2}h} = P^{(0)} + (u^{(0)}_z + w^{(0)}_x)(H^{(0)}_x \pm \frac{1}{2}h^{(0)}_x) + (v^{(0)}_z + w^{(0)}_y)(H^{(0)}_y \pm \frac{1}{2}h^{(0)}_y). \tag{A.51}$$

Substituting (A.49) into (A.50), using the known expressions for the leading order velocities, (A.45) and (A.48), and solving for $P^{(0)}_z$ yields

$$P^{(0)}_z = 2(H^{(0)}_{txx} + H^{(0)}_{tyy}). \tag{A.52}$$

Integrating (A.52) with respect to z leads to

$$P^{(0)} = 2(H^{(0)}_{txx} + H^{(0)}_{tyy})z + f_3(x,y,t). \tag{A.53}$$

Applying the boundary condition, (A.51), as well as (A.34) and (A.35), yields an expression for the pressure,

$$P^{(0)} = -2(u^{(0)}_x + v^{(0)}_y). \tag{A.54}$$

Let us now consider leading order balances of forces and balances of moments on a small element of the sheet (see Figure 2-1). When $Re = 0$ as considered here, inertia plays no role and the forces and the moments must each sum to zero. First let us consider balance of forces in the x-direction.

$$\sum F_x = 0 \tag{A.55}$$

$$0 = dydx\frac{\partial}{\partial x}\left[\int_{H-\frac{1}{2}h}^{H+\frac{1}{2}h} dz\sigma_{xx}\right] + dxdy\frac{\partial}{\partial y}\left[\int_{H-\frac{1}{2}h}^{H+\frac{1}{2}h} dz\sigma_{xy}\right] \tag{A.56}$$

or

$$\begin{aligned}\Rightarrow 0 \;=\; & \frac{\partial}{\partial x}[4(\bar{u}_x + H_x^{(0)}H_{tx}^{(0)})h^{(0)} + 2(\bar{v}_y + H_y^{(0)}H_{ty}^{(0)})h^{(0)}] + \\ & \frac{\partial}{\partial y}[(\bar{u}_y + H_y^{(0)}H_{tx}^{(0)})h^{(0)} + (\bar{v}_x + H_x^{(0)}H_{ty}^{(0)})h^{(0)}]\end{aligned} \tag{A.57}$$

which can be rewritten as

$$T_{11} \equiv 4(\bar{u}_x + H_x^{(0)}H_{tx}^{(0)})h^{(0)} + 2(\bar{v}_y + H_y^{(0)}H_{ty}^{(0)})h^{(0)} \tag{A.58}$$

$$T_{12} \equiv (\bar{u}_y + H_y^{(0)}H_{tx}^{(0)})h^{(0)} + (\bar{v}_x + H_x^{(0)}H_{ty}^{(0)})h^{(0)} \tag{A.59}$$

$$\frac{\partial T_{11}}{\partial x} + \frac{\partial T_{12}}{\partial y} = 0. \tag{A.60}$$

By the same argument, summing the forces in the y-direction yields

$$\sum F_y = 0 \tag{A.61}$$

$$\begin{aligned}0 \;=\; & \frac{\partial}{\partial y}[4(\bar{v}_y + H_y^{(0)}H_{ty}^{(0)})h^{(0)} + 2(\bar{u}_x + H_x^{(0)}H_{tx}^{(0)})h^{(0)}] + \\ & \frac{\partial}{\partial x}[(\bar{v}_x + H_x^{(0)}H_{ty}^{(0)})h^{(0)} + (\bar{u}_y + H_y^{(0)}H_{tx}^{(0)})h^{(0)}].\end{aligned} \tag{A.62}$$

$$T_{22} \equiv 4(\bar{v}_y + H_y^{(0)}H_{ty}^{(0)})h^{(0)} + 2(\bar{u}_x + H_x^{(0)}H_{tx}^{(0)})h^{(0)} \tag{A.63}$$

$$\frac{\partial T_{12}}{\partial x} + \frac{\partial T_{22}}{\partial y} = 0. \tag{A.64}$$

Now, summing the forces in the z-direction leads to the following relations (the leading order contributions are identically zero, so higher order terms have been included):

$$\sum F_z = 0 \tag{A.65}$$

$$\begin{aligned}0 = dydx\frac{\partial}{\partial x}\left[\int_{H-\frac{1}{2}h}^{H+\frac{1}{2}h} dz\sigma_{xz}\right] + dxdy\frac{\partial}{\partial y}\left[\int_{H-\frac{1}{2}h}^{H+\frac{1}{2}h} dz\sigma_{yz}\right] - dxdy\frac{G}{3}H^{(0)} + \\ dxdy\frac{\Gamma^+}{3}\nabla^2(H^{(0)} + \frac{1}{2}h^{(0)}) + dxdy\frac{\Gamma^-}{3}\nabla^2(H^{(0)} - \frac{1}{2}h^{(0)})\end{aligned} \tag{A.66}$$

where

$$Q_x \equiv \int_{H-\frac{1}{2}h}^{H+\frac{1}{2}h} dz\sigma_{xz} \tag{A.67}$$

$$Q_y \equiv \int_{H-\frac{1}{2}h}^{H+\frac{1}{2}h} dz\sigma_{yz} \tag{A.68}$$

which can be rewritten as

$$\frac{\partial Q_x}{\partial x} + \frac{\partial Q_y}{\partial y} = \frac{G}{3}H^{(0)} - \frac{\Gamma^+}{3}\nabla^2(H^{(0)} + \frac{1}{2}h^{(0)}) - \frac{\Gamma^-}{3}\nabla^2(H^{(0)} - \frac{1}{2}h^{(0)}). \tag{A.69}$$

Balancing moments about the y-axis,

$$\sum M_y = 0 \tag{A.70}$$

$$0 = dydx\frac{\partial}{\partial x}\left[\int_{H-\frac{1}{2}h}^{H+\frac{1}{2}h} dzz\sigma_{xx}\right] + dxdy\frac{\partial}{\partial y}\left[\int_{H-\frac{1}{2}h}^{H+\frac{1}{2}h} dzz\sigma_{xy}\right] - dydx\frac{Q_x}{\epsilon^2} \tag{A.71}$$

$$\begin{aligned}
\Rightarrow 0 \;=\; & \frac{\partial}{\partial x}\left[\int_{H-\frac{1}{2}h}^{H+\frac{1}{2}h} dzz(4\bar{u}_x + 4H_x^{(0)}H_{tx}^{(0)}) + 4z(H^{(0)} - z)H_{txx}^{(0)} + \right. \\
& \left. z(2\bar{v}_y + 2H_y^{(0)}H_{ty}^{(0)}) + 2z(H^{(0)} - z)H_{tyy}^{(0)}\right] + \\
& \frac{\partial}{\partial y}\left[\int_{H-\frac{1}{2}h}^{H+\frac{1}{2}h} dzz(\bar{u}_y + H_y^{(0)}H_{tx}^{(0)}) + z(H^{(0)} - z)H_{txy}^{(0)} + \right. \\
& \left. z(\bar{v}_x + H_x^{(0)}H_{ty}^{(0)}) + z(H^{(0)} - z)H_{txy}^{(0)} - \frac{Q_x}{\epsilon^2}\right]
\end{aligned} \tag{A.72}$$

$$\Rightarrow 0 = \frac{\partial}{\partial x}\left[H^{(0)}T_{11} - \frac{1}{3}{h^{(0)}}^3 H_{txx}^{(0)} - \frac{1}{6}{h^{(0)}}^3 H_{tyy}^{(0)}\right] + \frac{\partial}{\partial y}\left[H^{(0)}T_{12} - \frac{1}{6}{h^{(0)}}^3 H_{txy}^{(0)}\right] - \frac{Q_x}{\epsilon^2}. \tag{A.73}$$

Similarly,

$$\sum M_x = 0 \tag{A.74}$$

$$\Rightarrow 0 = \frac{\partial}{\partial y}\left[H^{(0)}T_{22} - \frac{1}{3}{h^{(0)}}^3 H_{tyy}^{(0)} - \frac{1}{6}{h^{(0)}}^3 H_{txx}^{(0)}\right] + \frac{\partial}{\partial x}\left[H^{(0)}T_{12} - \frac{1}{6}{h^{(0)}}^3 H_{txy}^{(0)}\right] - \frac{Q_y}{\epsilon^2}. \tag{A.75}$$

Finally, differentiating (A.75) with respect to y, differentiating (A.73) with respect to x, and adding the results gives

$$\begin{aligned}
0 \;=\; & \frac{\partial^2}{\partial x^2}\left[H^{(0)}T_{11} - \frac{1}{3}{h^{(0)}}^3 H_{txx}^{(0)} - \frac{1}{6}{h^{(0)}}^3 H_{tyy}^{(0)}\right] + \\
& \frac{\partial^2}{\partial y^2}\left[H^{(0)}T_{22} - \frac{1}{3}{h^{(0)}}^3 H_{tyy}^{(0)} - \frac{1}{6}{h^{(0)}}^3 H_{txx}^{(0)}\right] + \\
& 2\frac{\partial^2}{\partial x \partial y}\left[H^{(0)}T_{12} - \frac{1}{6}{h^{(0)}}^3 H_{txy}^{(0)}\right] - \epsilon^{-2}\left(\frac{\partial Q_x}{\partial x} + \frac{\partial Q_y}{\partial y}\right),
\end{aligned} \tag{A.76}$$

where the last terms can be rewritten using (A.69). Eliminating terms using (A.60), (A.64), (A.69) and rearranging terms leads to

$$H_{xx}^{(0)}T_{11} + 2H_{xy}^{(0)}T_{12} + H_{yy}^{(0)}T_{22} - \tfrac{GH^{(0)}}{3\epsilon^2} +$$

$$\frac{\Gamma^+}{3\epsilon^2}\nabla^2(H^{(0)}+\tfrac{1}{2}h^{(0)})+\frac{\Gamma^-}{3\epsilon^2}\nabla^2(H^{(0)}-\tfrac{1}{2}h^{(0)})=$$
$$\frac{\partial^2}{\partial x^2}\left[\tfrac{1}{3}{h^{(0)}}^3H^{(0)}_{txx}+\tfrac{1}{6}{h^{(0)}}^3H^{(0)}_{tyy}\right]+\frac{\partial^2}{\partial y^2}\left[\tfrac{1}{3}{h^{(0)}}^3H^{(0)}_{tyy}+\tfrac{1}{6}{h^{(0)}}^3H^{(0)}_{txx}\right]+$$
$$\frac{\partial^2}{\partial x\partial y}\left[\tfrac{1}{3}{h^{(0)}}^3H^{(0)}_{txy}\right]. \tag{A.77}$$

A sheet with initially uniform thickness, $h^{(0)}_x = h^{(0)}_y = 0$, will always remain uniformly thick because $h^{(0)}_t = 0$. Therefore,

$$H^{(0)}_{xx}T_{11}+2H^{(0)}_{xy}T_{12}+H^{(0)}_{yy}T_{22}-\frac{GH^{(0)}}{3\epsilon^2}+\frac{\Gamma}{3\epsilon^2}\nabla^2H^{(0)}=\frac{1}{3}{h^{(0)}}^3\nabla^4H^{(0)}_t, \tag{A.78}$$

where $\Gamma \equiv 3\frac{\gamma^+ + \gamma^-}{\mu U}$.

In general, in this thesis the superscript '(0)' is omitted, and all quantities of unspecified order are assumed to be leading order quantities.

Appendix B

Confirmation of pressure scaling in original theory

To confirm the pressure scaling in the theory for small displacements of a viscous sheet, let us examine the effect of considering larger pressures. In the original scaling at onset

$$\begin{array}{llll} x \sim L, & y \sim L, & z \sim \epsilon L, & P \sim \mu\epsilon\frac{U}{L}, \\ u \sim \epsilon U, & v \sim \epsilon U, & w \sim U, & t \sim \epsilon\frac{L}{U}. \end{array} \tag{B.1}$$

What if pressure is $O(\epsilon^{-2})$?

$$P \sim \mu\frac{U}{\epsilon^2 L} \tag{B.2}$$

From the leading order continuity equation

$$w_z^{(0)} = 0. \tag{B.3}$$

The kinematic boundary condition at leading order requires

$$w^{(0)} = H_t^{(0)}. \tag{B.4}$$

z-direction conservation of momentum requires at leading order that

$$P_z^{(0)} = \mu w_{zz}^{(0)} = 0. \tag{B.5}$$

The z-direction dynamic boundary condition to leading order states

$$P^{(0)} = 0. \tag{B.6}$$

Therefore, $P^{(0)}(x, y, z, t) = 0$, and P cannot be $O(\epsilon^{-2})$.

What if pressure is $O(\epsilon^{-1})$?

$$P \sim \mu\frac{U}{\epsilon L} \tag{B.7}$$

From leading order continuity

$$w_z^{(0)} = 0. \tag{B.8}$$

The leading order kinematic boundary condition requires

$$w^{(0)} = H_t^{(0)}. \tag{B.9}$$

At $O(\epsilon)$, the continuity equation requires

$$w_z^{(1)} = 0. \tag{B.10}$$

At $O(\epsilon)$, z-direction conservation of momentum requires

$$P_z^{(0)} = \mu w_{zz}^{(1)} = 0. \tag{B.11}$$

The leading order z-direction dynamic boundary condition states

$$P^{(0)} = 2\mu w_z^{(1)} = 0. \tag{B.12}$$

Therefore, $P^{(0)}(x, y, z, t) = 0$ and P cannot be $O(\epsilon^{-1})$.

The original scaling, $P \sim \mu \frac{U}{L}$, follows.

Appendix C

Sheared annular sheet with $G = \Gamma = 0$

W.R. Dean performed his calculations in the absence of gravity and surface tension [11]. In order to fully illustrate the analogy of the viscous results of this thesis to his elastic analysis, this appendix presents the predictions of the viscous analysis with $G = \Gamma = 0$. The evolution equation for the sheet, (2.18), in cylindrical coordinates becomes

$$\begin{aligned}
&H_{rr}\left[4u_r + \frac{2}{r}v_\theta + \frac{2}{r}u + 4H_rH_{tr} + \frac{2}{r^2}H_\theta H_{t\theta}\right] \\
&+2\left(\frac{H_{r\theta}}{r} - \frac{H_\theta}{r^2}\right)\left[v_r + \frac{1}{r}u_\theta - \frac{1}{r}v + \frac{1}{r}H_\theta H_{tr}\right] \\
&+\left(\frac{H_{\theta\theta}}{r^2} + \frac{H_r}{r}\right)\left[2u_r + \frac{4}{r}v_\theta + \frac{4}{r}u + 2H_rH_{tr} + \frac{2}{r^2}H_\theta H_{t\theta}\right] \\
&+\frac{2}{r^4}H_{\theta\theta}H_\theta H_{t\theta} + \frac{2}{r^2}H_{r\theta}H_rH_{t\theta} = \frac{1}{3}h^2\nabla^4 H_t. \qquad \text{(C.1)}
\end{aligned}$$

Because the in-plane stress balances do not change, the base solutions for the in-plane velocities, (A.45) and (A.48), also remains unchanged. Linearizing (C.1) about a base state of $H = 0$, and examining solutions of the form $H = e^{\sigma t + im\theta}f(r)$ results in a linear stability equation highly simplified by the absence of the gravity and surface tension terms,

$$\frac{d^4f}{dr^4} + \frac{2}{r}\frac{d^3f}{dr^3} - \frac{2m^2+1}{r^2}\frac{d^2f}{dr^2} + \frac{2m^2+iSm+1}{r^2}\frac{df}{dr} + \frac{m^4-4m^2-iSm}{r^4}f = 0 \qquad \text{(C.2)}$$

subject to boundary conditions at the inner and outer radii of the annulus, $r = R_i$ and $r = R_o$,

$$f(R_i) = f(R_o) = f'(R_i) = f'(R_o) = 0. \qquad \text{(C.3)}$$

Converting from independent variable r to $\xi \equiv \ln r$ transforms the stability equation, (C.2), into one with constant coefficients,

$$\frac{d^4 f}{d\xi^4} - 4\frac{d^3 f}{d\xi^3} + (4 - 2m^2)\frac{d^2 f}{d\xi^2} + (4m^2 + iSm)\frac{df}{d\xi} + (m^4 - 4m^2 - iSm)f = 0 \quad \text{(C.4)}$$

subject to clamped conditions at $\xi = \ln R_i$ and $\xi = \ln R_o$. The general solution to (C.4) can be written as

$$f(\xi) = A_1 e^{\lambda_1 \xi} + A_2 e^{\lambda_2 \xi} + A_3 e^{\lambda_3 \xi} + A_4 e^{\lambda_4 \xi}, \quad \text{(C.5)}$$

where the λ_i are the solutions to the characteristic polynomial of the stability equation,

$$\lambda^4 - 4\lambda^3 + (4 - 2m^2)\lambda^2 + (4m^2 + iSm)\lambda + (m^4 - 4m^2 - iSm) = 0. \quad \text{(C.6)}$$

The boundary conditions (C.3) can be written as

$$\begin{pmatrix} R_i^{\lambda_1} & R_i^{\lambda_2} & R_i^{\lambda_3} & R_i^{\lambda_4} \\ \lambda_1 R_i^{\lambda_1} & \lambda_2 R_i^{\lambda_2} & \lambda_3 R_i^{\lambda_3} & \lambda_4 R_i^{\lambda_4} \\ R_o^{\lambda_1} & R_o^{\lambda_2} & R_o^{\lambda_3} & R_o^{\lambda_4} \\ \lambda_1 R_o^{\lambda_1} & \lambda_2 R_o^{\lambda_2} & \lambda_3 R_o^{\lambda_3} & \lambda_4 R_o^{\lambda_4} \end{pmatrix} \begin{pmatrix} A_1 \\ A_2 \\ A_3 \\ A_4 \end{pmatrix} = \begin{pmatrix} 0 \\ 0 \\ 0 \\ 0 \end{pmatrix}. \quad \text{(C.7)}$$

Introducing a new parameter, $n \equiv \frac{R_o}{R_i}$, and performing some simplifications, the condition for the existence of nontrivial solutions can be written as

$$\begin{vmatrix} 1 & 1 & 1 & 1 \\ \lambda_1 & \lambda_2 & \lambda_3 & \lambda_4 \\ n^{\lambda_1} & n^{\lambda_2} & n^{\lambda_3} & n^{\lambda_4} \\ \lambda_1 n^{\lambda_1} & \lambda_2 n^{\lambda_2} & \lambda_3 n^{\lambda_3} & \lambda_4 n^{\lambda_4} \end{vmatrix} = 0. \quad \text{(C.8)}$$

Solving (C.6) and (C.8) numerically reveals the relationship between aspect ratio and S for each azimuthal wavenumber as depicted in Figure C-1(a) (Appendix F briefly discusses the numerical method employed.). $\sigma \in \Re$ as proved in Section D.1, so the instability does not migrate around the annulus. The stability plot is identical to Dean's stability plot for the elastic case. The only difference lies in the definition of S, $S \equiv \dot{\gamma}/\sigma$. In Dean's graph, the lower envelope of the family of curves dictates the mode number of the observed instability for each aspect ratio because the lowest curve represents the deformation that occurs for the smallest load. For the viscous case, the plot is better presented using $\sigma^* \equiv \frac{1}{S} = \sigma/\dot{\gamma}$ (Figure C-1(b)) where the upper envelope represents the observed instability because the highest curve for a given aspect ratio belongs to the deformation with the highest growth rate for a given load.

The results of the linear stability analysis reveal that infinitesimal disturbances of any azimuthal wavenumber in the out-of-plane displacement of the sheet will grow exponentially in time for any non-zero shear rate. The system is thus always unstable. The wave number dependent growth rates of the disturbances determine the particular

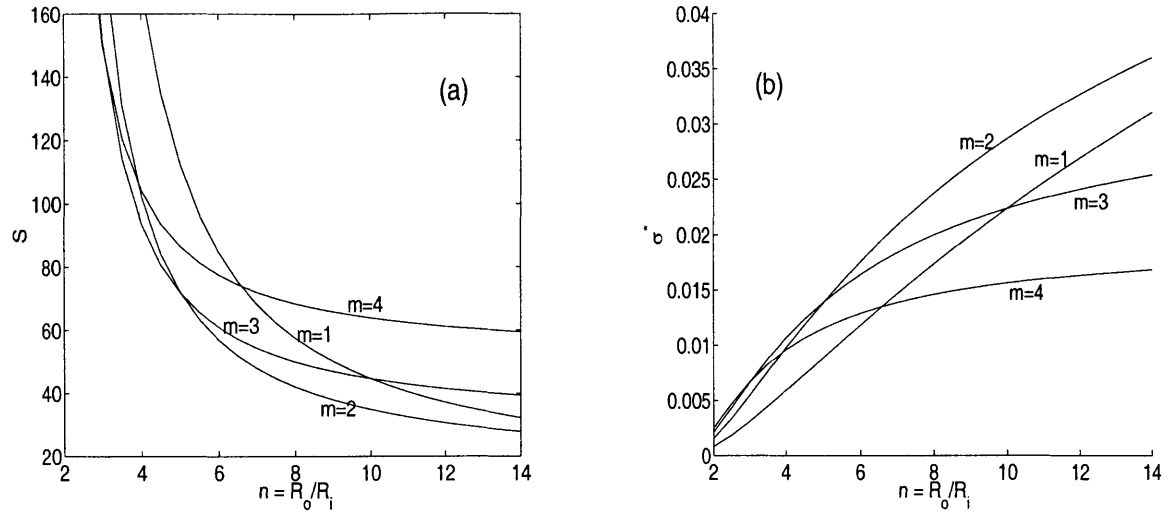

Figure C-1: (a) Viscous stability plot for $S = \dot{\gamma}/\sigma$ or Dean's elastic stability plot for $S = \gamma$. (b) Conventional stability plot with $\sigma^* = \sigma/\dot{\gamma}$.

number of observed wrinkles in a given sheet. The fastest growing disturbance which corresponds to the most unstable mode will rapidly dominate the geometry of the sheet. The envelope of the curves in the stability plot represents this set of most unstable modes as a function of the system aspect ratio.

These results ignore the effects of gravity and surface tension both of which stabilize the sheet with regard to the instability considered. Gravity most strongly damps longer wavelength ripples, and surface tension most strongly damps shorter wavelength ripples. Each effect, though, will act to some degree on all perturbation wavelengths. Therefore, the presence of these stabilizing phenomena creates a situation where a state of neutral stability exists for a non-zero forcing of the system. Stronger forcing than that in the neutral case will generate wrinkles in the sheet, weaker forcing will generate none.

Appendix D

Proof that the instability is a pitchfork bifurcation with real growth rates

D.1 Case 1: Sheared annular sheet with $G \neq 0$ and $\Gamma \neq 0$

The following equation governs small motions of the sheet:

$$D\nabla^4 H_t - \frac{S}{r^3}\left(\frac{H_\theta}{r} - H_{r\theta}\right) - \frac{\Gamma}{3}\nabla^2 H + \frac{1}{3}GH = 0. \tag{D.1}$$

Boundary conditions: at $r = R_o$ and $r = R_i$

$$H = 0 \tag{D.2}$$

and

$$H_r = 0. \tag{D.3}$$

The following proof follows a method inspired by similar analysis done by Southwell and Skan for the rectilinear problem [28]. Consider solutions to (D.1) of the form

$$H = (W + iW')e^{i\sigma t}, \tag{D.4}$$

where W and W' are arbitrary real functions, and σ is potentially complex. Consider two solutions,

$$H_1 = (W + iW')e^{i\sigma t} \tag{D.5}$$

and its complex conjugate

$$H_2 = (W - iW')e^{-i\sigma^* t}, \tag{D.6}$$

where the superscript * indicates conjugation.

If H_1 is a solution, then H_2 is also a solution because the real and imaginary parts

of the solution don't interact in a linear equation with real coefficients. Hence the real part of the equation governing H_1 is the same as the real part of the equation governing H_2, while the imaginary part of the equation governing H_1 is the negative of the imaginary part of the equation governing H_2, and thus if one is satisfied the other must be satisfied as well. Because the boundary conditions compare in the same fashion, the supposition must be true: if H_1 is a solution, then H_2 is also a solution.

Thus, it is true that

$$\iint \left[H_1 \left(D\nabla^4 H_{2t} - \frac{S}{r^3}\left(\frac{H_{2\theta}}{r} - H_{2r\theta}\right) - \frac{\Gamma}{3}\nabla^2 H_2 + \frac{1}{3}GH_2 \right) - H_2 \left(D\nabla^4 H_{1t} - \frac{S}{r^3}\left(\frac{H_{1\theta}}{r} - H_{1r\theta}\right) - \frac{\Gamma}{3}\nabla^2 H_1 + \frac{1}{3}GH_1 \right) \right] dA = 0, \tag{D.7}$$

where the integrals are over the whole sheet. Utilizing the known forms of H_1 and H_2, (D.5) and (D.6), yields

$$\begin{aligned} & iD \iint \left[\sigma H_2 \nabla^4 H_1 - \sigma^* H_1 \nabla^4 H_2 \right] dA \\ & -S \iint \left(\frac{H_2 H_{1\theta}}{r^3} - \frac{H_2 H_{1r\theta}}{r^2} - \frac{H_1 H_{2\theta}}{r^3} + \frac{H_1 H_{2r\theta}}{r^2} \right) dr d\theta - \\ & \frac{\Gamma}{3} \iint \left(H_1 \nabla^2 H_2 - H_2 \nabla^2 H_1 \right) dA = 0 \end{aligned} \tag{D.8}$$

which can be rewritten as

$$\begin{aligned} & iD \iint \left[\sigma \nabla \cdot \left(H_2 \nabla \left(\nabla^2 H_1 \right) \right) - \sigma \left(\nabla H_2 \right) \cdot \nabla \left(\nabla^2 H_1 \right) - \right. \\ & \left. \sigma^* \nabla \cdot \left(H_1 \nabla \left(\nabla^2 H_2 \right) \right) + \sigma^* \left(\nabla H_1 \right) \cdot \nabla \left(\nabla^2 H_2 \right) \right] dA \\ & -S \iint \left[\frac{\partial}{\partial \theta} \left(\frac{H_2 H_1}{r^3} - \frac{H_2 H_{1r}}{r^2} \right) - \right. \\ & \left. H_{2\theta} \left(\frac{H_1}{r^3} - \frac{H_{1r}}{r^2} \right) + \frac{\partial}{\partial r} \left(\frac{H_1 H_{2\theta}}{r^2} \right) + \frac{H_1 H_{2\theta}}{r^3} - \frac{H_{1r} H_{2\theta}}{r^2} \right] dr d\theta \\ & -\frac{\Gamma}{3} \iint \left[\nabla \cdot \left(H_1 \nabla H_2 \right) - \left(\nabla H_1 \right) \cdot \left(\nabla H_2 \right) - \right. \\ & \left. \nabla \cdot \left(H_2 \nabla H_1 \right) + \left(\nabla H_2 \right) \cdot \left(\nabla H_1 \right) \right] dA = 0. \end{aligned} \tag{D.9}$$

Using the divergence theorem and (D.2) to eliminate terms in the first and third integrals and canceling terms in the second and third integrals yields

$$\begin{aligned} & iD \iint \left[-\sigma \left(\nabla H_2 \right) \cdot \nabla \left(\nabla^2 H_1 \right) + \sigma^* \left(\nabla H_1 \right) \cdot \nabla \left(\nabla^2 H_2 \right) \right] dA \\ & -S \int \left[\frac{H_2 H_1}{r^3} - \frac{H_2 H_{1r}}{r^2} \right]_{\theta=0}^{2\pi} dr - S \int \left[\frac{H_1 H_{2\theta}}{r^2} \right]_{r=R_i}^{R_o} d\theta = 0. \end{aligned} \tag{D.10}$$

Rewriting the equation again noting that the integrand of the second integral vanishes due to periodicity and the integrand of the last integral vanishes due to the

homogeneous boundary conditions yields

$$iD\iint \left[\sigma\nabla^2 H_1\nabla^2 H_2 - \sigma\nabla\cdot\left(\nabla^2 H_1\nabla H_2\right) - \sigma^*\nabla^2 H_2\nabla^2 H_1 + \sigma^*\nabla\cdot\left(\nabla^2 H_2\nabla H_1\right)\right] dA = 0, \tag{D.11}$$

and applying the divergence theorem and (D.3) yields

$$iD(\sigma-\sigma^*)\iint \left[\nabla^2 H_1\nabla^2 H_2\right] dA = 0. \tag{D.12}$$

Substituting the forms of H_2 and H_1 from (D.5) and (D.6) yields

$$iD(\sigma-\sigma^*)e^{i(\sigma-\sigma^*)t}\iint \left[\left(\nabla^2 W\right)^2 + \left(\nabla^2 W'\right)^2\right] dA = 0. \tag{D.13}$$

In order for this expression to be true, it must be that

$$\sigma = \sigma^*, \tag{D.14}$$

implying that σ is strictly real and that there are thus no traveling waves or oscillations in the solution, just a growing or decaying mode shape.

D.2 Case 2: Sheared rectilinear sheet with $G \neq 0$ and $\Gamma \neq 0$

The following equation governs small motions of the sheet:

$$D\nabla^4 H_t - 2S\frac{\partial^2 H}{\partial x\partial y} - \frac{\Gamma}{3}\nabla^2 H + \frac{1}{3}GH = 0. \tag{D.15}$$

Boundary conditions: at $y = \pm B$

$$H = 0 \tag{D.16}$$

and

$$H_y = 0. \tag{D.17}$$

The following proof follows a method inspired by similar analysis done by Southwell and Skan [28]. Consider solutions to (D.15) of the form

$$H = (W + iW')e^{i\sigma t}, \tag{D.18}$$

where W and W' are arbitrary real functions, and σ is potentially complex. Consider two solutions,

$$H_1 = (W + iW')e^{i\sigma t} \tag{D.19}$$

and its complex conjugate

$$H_2 = (W - iW')e^{-i\sigma^* t}, \tag{D.20}$$

where the superscript * indicates conjugation. If H_1 is a solution, then H_2 is also a solution:

$$H_1 = H_r + iH_i \tag{D.21}$$

$$H_2 = H_r - iH_i. \tag{D.22}$$

Plugging H_1 into the governing differential equation and separating the real and imaginary parts of the equation yields

$$D\nabla^4 H_{rt} - 2S\frac{\partial^2 H_r}{\partial x \partial y} - \frac{\Gamma}{3}\nabla^2 H_r + \frac{1}{3}GH_r = 0 \tag{D.23}$$

$$D\nabla^4 H_{it} - 2S\frac{\partial^2 H_i}{\partial x \partial y} - \frac{\Gamma}{3}\nabla^2 H_i + \frac{1}{3}GH_i = 0. \tag{D.24}$$

Plugging H_2 into the same equation and separating the real and imaginary parts yields the same two equations which are true by assumption. The boundary conditions compare in the same fashion, and we find that the supposition is true, if H_1 is a solution, then H_2 is also a solution.

Thus, it is true that

$$\iint \left[H_1 \left(D\nabla^4 H_{2t} - 2S\frac{\partial^2 H_2}{\partial x \partial y} - \frac{\Gamma}{3}\nabla^2 H_2 + \frac{1}{3}GH_2 \right) - H_2 \left(D\nabla^4 H_{1t} - 2S\frac{\partial^2 H_1}{\partial x \partial y} - \frac{\Gamma}{3}\nabla^2 H_1 + \frac{1}{3}GH_1 \right) \right] dA = 0, \tag{D.25}$$

where the integrals are over the whole sheet. Utilizing the known forms of H_1 and H_2, (D.19) and (D.20), yields

$$iD\iint \left[\sigma H_2 \nabla^4 H_1 - \sigma^* H_1 \nabla^4 H_2\right] dA - 2S\iint \left(H_2 H_{1xy} - H_1 H_{2xy}\right) dA - \frac{\Gamma}{3}\iint \left(H_1 \nabla^2 H_2 - H_2 \nabla^2 H_1\right) dA = 0. \tag{D.26}$$

The second term can be rewritten as

$$-2S\iint \left[\frac{\partial}{\partial x}(H_2 H_{1y}) - \frac{\partial}{\partial y}(H_1 H_{2x})\right] dA \tag{D.27}$$

and eliminated using Green's theorem and (D.16). It immediately follows from the results of Section D.1 that

$$\sigma = \sigma^*, \tag{D.28}$$

implying that σ is strictly real and that there are thus no traveling waves or oscillations in the solution, just a growing or decaying mode shape.

Appendix E

Distinguished scalings for the nonlinear problem

E.1 Saturation at $H \sim h$

Consider the following scaling of the equations appropriate for saturated wrinkles with amplitudes of the order of the thickness of the sheet:

$$\begin{array}{llllll} u \sim U, & v \sim U, & w \sim \epsilon U, & & & \\ h \sim \epsilon L, & H \sim \epsilon L, & x \sim L, & y \sim L, & z \sim \epsilon L. & \end{array} \tag{E.1}$$

This scaling is the one used in lubrication theory. Time and pressure still require scalings, but let us examine the equations first to inform our assignment of their scales. Time appears explicitly only in the kinematic boundary condition:

$$w|_{z=H\pm\frac{1}{2}h} = \frac{D}{Dt}(H \pm \frac{1}{2}h) = H_t \pm \frac{1}{2}h_t + (H_x \pm \frac{1}{2}h_x)u + (H_y \pm \frac{1}{2}h_y)v. \tag{E.2}$$

All of the terms in the boundary condition are $O(\epsilon U)$ with the possible exception of $H_t \pm \frac{1}{2}h_t$. t can thus be no smaller than $O(L/U)$ because assigning it a smaller value would immediately imply a contradiction by requiring that H_t and h_t be zero so that nothing would change on that time scale. So let us take

$$t \sim \frac{L}{U}. \tag{E.3}$$

The largest term against which pressure is balanced is u_{zz} in the x-momentum equation (A.1). Let us take a conservative estimate of the magnitude of the pressure and scale it so that P_x can balance u_{zz},

$$P \sim \mu \frac{U}{\epsilon^2 L}. \tag{E.4}$$

Expand all of the variables as perturbation series in the small parameter ϵ (e.g. $u = u^{(0)} + \epsilon u^{(1)} + \epsilon^2 u^{(2)} + \cdots$). Substitute the perturbation series forms into the

Stokes equations and boundary conditions and scale each equation so that the largest terms are $O(\epsilon^0)$. Consider first the z-momentum equation

$$P_z = \mu(w_{xx} + w_{yy} + w_{zz}) \tag{E.5}$$

which to leading order states that

$$P_z^{(0)} = 0. \tag{E.6}$$

Now let us examine the z-direction dynamic boundary condition at $z = H \pm \frac{1}{2}h$

$$-(H_x \pm \frac{1}{2}h_x)\mu(u_z + w_x) - (H_y \pm \frac{1}{2}h_y)\mu(v_z + w_y) - P + 2\mu w_z = 0 \tag{E.7}$$

or to leading order

$$P^{(0)} = 0. \tag{E.8}$$

This in conjunction with (E.6) shows that $P^{(0)}(x, y, z, t) = 0$ and that the pressure is not $O(\epsilon^{-2})$. So let us now instead consider

$$P \sim \mu\frac{U}{\epsilon L}. \tag{E.9}$$

Once again, the leading order z-momentum equation states that

$$P_z^{(0)} = 0, \tag{E.10}$$

and the leading order z-direction dynamic boundary condition requires that at the surface

$$P^{(0)} = 0, \tag{E.11}$$

so that $P^{(0)}(x, y, z, t) = 0$ for this scaling as well. This finally leads us to the conclusion that the pressure will scale as the viscous stresses arising from the in-plane velocity gradients created by boundary motion,

$$P \sim \mu\frac{U}{L}. \tag{E.12}$$

The x and y momentum equations are to leading order

$$u_{zz}^{(0)} = 0 \tag{E.13}$$

$$v_{zz}^{(0)} = 0 \tag{E.14}$$

which upon integration give

$$u^{(0)} = \bar{u} + (H^{(0)} - z)f_1(x, y) \tag{E.15}$$

$$v^{(0)} = \bar{v} + (H^{(0)} - z)f_3(x, y) \tag{E.16}$$

Examining the x and y dynamic boundary conditions

$$-(H_x \pm \frac{1}{2}h_x)(-P + 2\mu u_x) - (H_y \pm \frac{1}{2}h_y)(u_y + v_x) + \mu(u_z + w_x) = 0 \tag{E.17}$$

$$-(H_x \pm \frac{1}{2}h_x)\mu(u_y + v_x) - (H_y \pm \frac{1}{2}h_y)(-P + 2\mu v_y) + \mu(v_z + w_y) = 0 \tag{E.18}$$

which to leading order require

$$u_z^{(0)} = 0 \tag{E.19}$$

$$v_z^{(0)} = 0 \tag{E.20}$$

shows that

$$f_1(x, y) = 0 \tag{E.21}$$

$$f_3(x, y) = 0 \tag{E.22}$$

and

$$u^{(0)} = \bar{u} \tag{E.23}$$

$$v^{(0)} = \bar{v}. \tag{E.24}$$

The leading order continuity equation states

$$w_z^{(0)} = -\bar{u}_x - \bar{v}_y. \tag{E.25}$$

The leading order z-momentum equation states

$$P_z^{(0)} = \mu w_{zz}^{(0)}. \tag{E.26}$$

Plugging in $w_z^{(0)}$ from (E.25) yields

$$P_z^{(0)} = 0. \tag{E.27}$$

The z dynamic boundary condition, (E.7), to leading order yields

$$P^{(0)} = -2\mu(\bar{u}_x - \bar{v}_y) \tag{E.28}$$

after utilizing known forms of $u^{(0)}$, $v^{(0)}$, and $w_z^{(0)}$ from (E.23), (E.24), and (E.25).

Let us now examine the balances of forces and moments on a depth-integrated infinitesimal section of the sheet. Selected leading order stresses in the sheet are

$$\sigma_{xx} = \mu(4\bar{u}_x + 2\bar{v}_y) \tag{E.29}$$

$$\sigma_{yy} = \mu(2\bar{u}_x + 4\bar{v}_y) \tag{E.30}$$

$$\sigma_{xy} = \mu(\bar{u}_y + \bar{v}_x) \tag{E.31}$$

and the depth-integrated stresses are

$$T_{11} \equiv \mu(4\bar{u}_x + 2\bar{v}_y)h^{(0)} \tag{E.32}$$

$$T_{22} \equiv \mu(4\bar{v}_y + 2\bar{u}_x)h^{(0)} \tag{E.33}$$

$$T_{12} \equiv \mu(\bar{u}_y + \bar{v}_x)h^{(0)}. \tag{E.34}$$

Balance of forces in the x and y directions requires

$$\frac{\partial T_{11}}{\partial x} + \frac{\partial T_{12}}{\partial y} = 0 \tag{E.35}$$

$$\frac{\partial T_{12}}{\partial x} + \frac{\partial T_{22}}{\partial y} = 0. \tag{E.36}$$

Balance of moments in the x and y directions requires

$$0 = \frac{\partial}{\partial x}\left[\int_{H-\frac{1}{2}h}^{H+\frac{1}{2}h} dzz\sigma_{xx}\right] + \frac{\partial}{\partial y}\left[\int_{H-\frac{1}{2}h}^{H+\frac{1}{2}h} dzz\sigma_{xy}\right] - Q_x \tag{E.37}$$

$$0 = \frac{\partial}{\partial x}\left[\int_{H-\frac{1}{2}h}^{H+\frac{1}{2}h} dzz\sigma_{xy}\right] + \frac{\partial}{\partial y}\left[\int_{H-\frac{1}{2}h}^{H+\frac{1}{2}h} dzz\sigma_{yy}\right] - Q_y \tag{E.38}$$

or

$$0 = \frac{\partial}{\partial x}\left[H^{(0)}h^{(0)}T_{11}\right] + \frac{\partial}{\partial y}\left[H^{(0)}h^{(0)}T_{12}\right] - Q_x \tag{E.39}$$

$$0 = \frac{\partial}{\partial x}\left[H^{(0)}h^{(0)}T_{12}\right] + \frac{\partial}{\partial y}\left[H^{(0)}h^{(0)}T_{22}\right] - Q_y \tag{E.40}$$

where

$$Q_x \equiv \int_{H-\frac{1}{2}h}^{H+\frac{1}{2}h} \sigma_{xz}dz \tag{E.41}$$

$$Q_y \equiv \int_{H-\frac{1}{2}h}^{H+\frac{1}{2}h} \sigma_{yz}dz. \tag{E.42}$$

Balance of forces in the z-direction requires

$$\frac{\partial Q_x}{\partial x} + \frac{\partial Q_y}{\partial y} - \rho g H^{(0)} = 0. \tag{E.43}$$

Substituting expressions from the balances of moments, (E.37) and (E.38), for Q_x and Q_y and applying the force balances, (E.35) and (E.36), to eliminate terms in the expanded derivatives yields

$$H_{xx}^{(0)}T_{11} + 2H_{xy}^{(0)}T_{12} + H_{yy}^{(0)}T_{22} = \rho g H^{(0)}, \tag{E.44}$$

where the bending term, $\nabla^4 H_t^{(0)}$, has vanished due to its time derivative which becomes very small on the lubrication theory time scale at saturation which is much longer than the folding time scale. Note that the time scale did not enter explicitly into the derivation of these equations, so even if the correct time scale turns out to be slower than that considered here, the resulting linearity of the equations would be unaffected.

E.2 A new scaling for the amplitude saturation

E.2.1 Curvilinear coordinate system

Let x', y', and z' be the sheet centered curvilinear coordinates, where $\vec{z}'$ points in the original $\vec{z}$ direction; $\vec{x}'$ points along the sheet center surface in the original $x-z$ plane; and $\vec{y}'$ points along the sheet center surface in the original $y-z$ plane (see Figure 5-1). Let the origin of the (x',y',z') system lie on the sheet center surface. The following relationships exist between the two coordinate systems:

$$\vec{x}' = \frac{\vec{x} + H_x\vec{z}}{\sqrt{1+H_x^2}} \tag{E.45}$$

$$\vec{y}' = \frac{\vec{y} + H_y\vec{z}}{\sqrt{1+H_y^2}} \tag{E.46}$$

$$\vec{z}' = \vec{z} \tag{E.47}$$

$$\vec{x} = \sqrt{1+H_x^2}\vec{x}' - H_x\vec{z}' \tag{E.48}$$

$$\vec{y} = \sqrt{1+H_y^2}\vec{y}' - H_y\vec{z}' \tag{E.49}$$

$$\vec{z} = \vec{z}' \tag{E.50}$$

Derivatives:

$$\frac{\partial}{\partial x} = \sqrt{1+H_x^2}\frac{\partial}{\partial x'} - H_x\frac{\partial}{\partial z'} \tag{E.51}$$

$$\frac{\partial}{\partial y} = \sqrt{1+H_y^2}\frac{\partial}{\partial y'} - H_y\frac{\partial}{\partial z'} \tag{E.52}$$

$$\frac{\partial}{\partial z} = \frac{\partial}{\partial z'} \tag{E.53}$$

$$\frac{\partial^2}{\partial x^2} = \frac{H_xH_{xx}}{\sqrt{1+H_x^2}}\frac{\partial}{\partial x'} - H_{xx}\frac{\partial}{\partial z'} + (1+H_x^2)\frac{\partial^2}{\partial x'^2} - 2H_x\sqrt{1+H_x^2}\frac{\partial^2}{\partial x'\partial z'} + H_x^2\frac{\partial^2}{\partial z'^2} \tag{E.54}$$

$$\frac{\partial^2}{\partial y^2} = \frac{H_yH_{yy}}{\sqrt{1+H_y^2}}\frac{\partial}{\partial y'} - H_{yy}\frac{\partial}{\partial z'} + (1+H_y^2)\frac{\partial^2}{\partial y'^2} - 2H_y\sqrt{1+H_y^2}\frac{\partial^2}{\partial y'\partial z'} + H_y^2\frac{\partial^2}{\partial z'^2} \tag{E.55}$$

$$\frac{\partial^2}{\partial z^2} = \frac{\partial^2}{\partial z'^2} \tag{E.56}$$

E.2.2 Scaling of equations

Time and pressure still require scalings, but, as before, let us examine the equations first to inform our assignment of their scales. The kinematic boundary condition on

w states:

$$w|_{z=H\pm\frac{1}{2}h} = \frac{D}{Dt}(H \pm \frac{1}{2}h) = H_t \pm \frac{1}{2}h_t + (H_x \pm \frac{1}{2}h_x)u + (H_y \pm \frac{1}{2}h_y)v \tag{E.57}$$

which at leading order reduces to

$$w^{(0)} = H_t^{(0)} + H_x^{(0)}u^{(0)} + H_y^{(0)}v^{(0)}. \tag{E.58}$$

All of the leading order terms in the boundary condition are $O(U)$ with the possible exception of H_t. t can thus be no smaller than $O(L/U)$ because assigning it a smaller value would immediately imply a contradiction by requiring that H_t be zero so that nothing would change on that time scale. So let us take

$$t \sim \frac{L}{U}. \tag{E.59}$$

Continuity and the Stokes equations remain

$$u_x + v_y + w_z = 0 \tag{E.60}$$

$$0 = -\nabla P + \mu\nabla^2\vec{u}. \tag{E.61}$$

The largest term against which pressure is balanced is $u_{z'z'}$ in the x-momentum equation. Let us take a conservative estimate of the magnitude of the pressure and scale it so that P_x can balance $u_{z'z'}$,

$$P \sim \mu\frac{U}{\epsilon^2 L}. \tag{E.62}$$

Consider first the z-momentum equation

$$P_z = \mu(w_{xx} + w_{yy} + w_{zz}) \tag{E.63}$$

which to leading order states that

$$P_{z'}^{(0)} = 0. \tag{E.64}$$

Now let us examine the z-direction dynamic boundary condition at $z = H \pm \frac{1}{2}h$,

$$-(H_x \pm \frac{1}{2}h_x)\mu(u_z + w_x) - (H_y \pm \frac{1}{2}h_y)\mu(v_z + w_y) - P + 2\mu w_z = 0 \tag{E.65}$$

or, to leading order,

$$P^{(0)} = 0. \tag{E.66}$$

This in conjunction with (E.64) shows that $P^{(0)}(x, y, z, t) = 0$ and that the pressure is not $O(\epsilon^{-2})$. So let us now instead consider

$$P \sim \mu\frac{U}{\epsilon L}. \tag{E.67}$$

Now the leading order momentum equations state that

$$P_{z'}^{(0)} = \mu(1 + H_x^{(0)^2} + H_y^{(0)^2})w_{z'z'}^{(0)} \tag{E.68}$$

$$-H_x^{(0)}P_{z'}^{(0)} = \mu(1 + H_x^{(0)^2} + H_y^{(0)^2})u_{z'z'}^{(0)} \tag{E.69}$$

$$-H_y^{(0)}P_{z'}^{(0)} = \mu(1 + H_x^{(0)^2} + H_y^{(0)^2})v_{z'z'}^{(0)}. \tag{E.70}$$

Using the (E.68) to eliminate $P_{z'}^{(0)}$ from (E.69) and (E.70) yields

$$u_{z'z'}^{(0)} = -H_x^{(0)}w_{z'z'}^{(0)} \tag{E.71}$$

$$v_{z'z'}^{(0)} = -H_y^{(0)}w_{z'z'}^{(0)}. \tag{E.72}$$

The leading order continuity equation states that

$$-H_x^{(0)}u_{z'}^{(0)} - H_y^{(0)}v_{z'}^{(0)} + w_{z'}^{(0)} = 0 \tag{E.73}$$

which, differentiated with respect to z', requires

$$w_{z'z'}^{(0)} = H_x^{(0)}u_{z'z'}^{(0)} + H_y^{(0)}v_{z'z'}^{(0)}. \tag{E.74}$$

Using (E.74) to eliminate $w_{z'z'}^{(0)}$ in (E.71) and (E.72) yields

$$(1 + H_x^{(0)^2})u_{z'z'}^{(0)} = -H_x^{(0)}H_y^{(0)}v_{z'z'}^{(0)} \tag{E.75}$$

$$(1 + H_y^{(0)^2})v_{z'z'}^{(0)} = -H_x^{(0)}H_y^{(0)}u_{z'z'}^{(0)} \tag{E.76}$$

which can be combined to form

$$(1 + H_x^{(0)^2} + H_y^{(0)^2})u_{z'z'}^{(0)} = 0 \tag{E.77}$$

so that

$$u_{z'z'}^{(0)} = 0 \tag{E.78}$$

and, similarly,

$$v_{z'z'}^{(0)} = 0. \tag{E.79}$$

When substituted into (E.74) these reveal that

$$w_{z'z'}^{(0)} = 0 \tag{E.80}$$

which, in conjunction with (E.68), shows that

$$P_z^{(0)} = 0. \tag{E.81}$$

Now the derivation below [(E.92) through (E.109)] can be followed leading to

$$\bar{u}_{z'} = f_1(x, y, t) \tag{E.82}$$

$$\bar{v}_{z'} = f_3(x, y, t) \tag{E.83}$$

$$\bar{w}_{z'} = H_x^{(0)} f_1 + H_y^{(0)} f_3. \tag{E.84}$$

At leading order the three dynamic boundary conditions reduce to

$$-H_x^{(0)} \frac{P^{(0)}}{\mu} = (1 + {H_x^{(0)}}^2 + {H_y^{(0)}}^2) f_1 \tag{E.85}$$

$$-H_y^{(0)} \frac{P^{(0)}}{\mu} = (1 + {H_x^{(0)}}^2 + {H_y^{(0)}}^2) f_3 \tag{E.86}$$

$$\frac{P}{\mu} = (1 + {H_x^{(0)}}^2 + {H_y^{(0)}}^2)(H_x^{(0)} f_1 + H_y^{(0)} f_3). \tag{E.87}$$

Using (E.85) and (E.86) to eliminate f_1 and f_3 from (E.87) yields

$$(1 + {H_x^{(0)}}^2 + {H_y^{(0)}}^2) \frac{P^{(0)}}{\mu} = 0 \tag{E.88}$$

so that

$$P^{(0)} = 0 \tag{E.89}$$

which together with (E.81) demonstrates that

$$P^{(0)}(x, y, z, t) = 0. \tag{E.90}$$

Thus, P cannot be $O(\epsilon^{-1})$, and

$$P \sim \mu \frac{U}{L} \tag{E.91}$$

remains. The pressure scales as the characteristic viscous stresses generated by the depth-averaged in-plane velocity gradients.

E.2.3 Derivation of expressions for significant field variables

To leading order continuity requires

$$-H_x^{(0)} u_{z'}^{(0)} - H_y^{(0)} v_{z'}^{(0)} + w_{z'}^{(0)} = 0. \tag{E.92}$$

The sheet is subject to the following kinematic boundary condition at $z' = \pm\frac{1}{2}h$:

$$w(x, y, H \pm \frac{1}{2}h, t) = \frac{D(H \pm \frac{1}{2}h)}{Dt} = H_t \pm \frac{1}{2}h_t + uH_x + vH_y \pm u\frac{1}{2}h_x \pm \frac{1}{2}vh_y \tag{E.93}$$

which at leading order requires

$$w^{(0)}(x, y, H \pm h/2, t) = H_t^{(0)} + u^{(0)} H_x^{(0)} + v^{(0)} H_y^{(0)}. \tag{E.94}$$

To leading order the x and y direction Stokes equations state

$$u^{(0)}_{z'z'} = 0 \tag{E.95}$$

$$v^{(0)}_{z'z'} = 0 \tag{E.96}$$

so, integrating,

$$u^{(0)} = \bar{u} + z' f_1(x,y,t) \tag{E.97}$$
$$v^{(0)} = \bar{v} + z' f_3(x,y,t). \tag{E.98}$$

Substituting these forms for the in-plane velocities into (E.92) yields

$$w^{(0)}_{z'} = H^{(0)}_x f_1 + H^{(0)}_y f_3 \tag{E.99}$$

which integrates to

$$w^{(0)} = (H^{(0)}_x f_1 + H^{(0)}_y f_3) z' + f_5(x,y,t). \tag{E.100}$$

Now utilizing (E.97), (E.98), and (E.100) in (E.94) yields

$$\pm(H^{(0)}_x f_1 + H^{(0)}_y f_3)\frac{h^{(0)}}{2} + f_5 = H^{(0)}_t + \bar{u}H^{(0)}_x + \bar{v}H^{(0)}_y \pm \frac{1}{2}h^{(0)} f_1 H^{(0)}_x \pm \frac{1}{2}h^{(0)} f_3 H^{(0)}_y. \tag{E.101}$$

Averaging the top and bottom boundary conditions reveals

$$f_5 = H^{(0)}_t + \bar{u}H^{(0)}_x + \bar{v}H^{(0)}_y. \tag{E.102}$$

Plugging this result into (E.100) gives

$$w^{(0)} = H^{(0)}_t + u^{(0)}H^{(0)}_x + v^{(0)}H^{(0)}_y. \tag{E.103}$$

In the absence of gravity and surface tension, the upper and lower surfaces of the sheet are free of traction as expressed by the dynamic boundary condition at $z = H \pm \frac{1}{2}h$:

$$\underline{\underline{\sigma}} \cdot \vec{n}^{\pm} = 0 \tag{E.104}$$

$$\vec{n}^{\pm} = \pm\frac{[-H_x, -H_y, 1]}{\sqrt{1 + H_x^2 + H_y^2}} \tag{E.105}$$

$$\underline{\underline{\sigma}} = \begin{pmatrix} -P + 2\mu u_x & \mu(u_y + v_x) & \mu(u_z + w_x) \\ \mu(u_y + v_x) & -P + 2\mu v_y & \mu(v_z + w_y) \\ \mu(u_z + w_x) & \mu(v_z + w_y) & -P + 2\mu w_z \end{pmatrix}, \tag{E.106}$$

where only the leading order terms have been included in $\vec{n}^{\pm}$. The three components of the dynamic boundary condition are

$$-H_x(-P + 2\mu u_x) - H_y\mu(u_y + v_x) + \mu(u_z + w_x) = 0 \tag{E.107}$$

$$-H_x\mu(u_y+v_x)-H_y(-P+2\mu v_y)+\mu(v_z+w_y)=0 \tag{E.108}$$
$$-H_x\mu(u_z+w_x)-H_y\mu(v_z+w_y)-P+2\mu w_z=0. \tag{E.109}$$

To leading order, at $z=H\pm\frac{1}{2}h$, (E.107) requires

$$-H_x^{(0)}(-2H_x^{(0)}f_1)-H_y^{(0)}(-H_y^{(0)}f_1-H_x^{(0)}f_3)+f_1-H_x^{(0)}(H_x^{(0)}f_1+H_y^{(0)}f_3)=0 \tag{E.110}$$

$$(1+{H_x^{(0)}}^2+{H_y^{(0)}}^2)f_1=0 \tag{E.111}$$
$$f_1=0, \tag{E.112}$$

and (E.108) by similar arguments requires

$$f_3=0, \tag{E.113}$$

so the in-plane velocities do not vary through the thickness of the sheet.

$$u^{(0)}=\bar{u} \tag{E.114}$$
$$v^{(0)}=\bar{v} \tag{E.115}$$
$$w^{(0)}=H_t^{(0)}+\bar{u}H_x^{(0)}+\bar{v}H_y^{(0)}. \tag{E.116}$$

At $O(\epsilon)$, continuity requires

$$w_{z'}^{(1)}-H_x^{(0)}u_{z'}^{(1)}-H_y^{(0)}v_{z'}^{(1)}+\bar{u}_x+\bar{v}_y=0. \tag{E.117}$$

Momentum conservation at $O(\epsilon)$ requires

$$P_{z'}^{(0)}=\mu({H_x^{(0)}}^2w_{z'z'}^{(1)}+{H_y^{(0)}}^2w_{z'z'}^{(1)}+w_{z'z'}^{(1)}) \tag{E.118}$$

or

$$P_{z'}^{(0)} = \mu(1+{H_x^{(0)}}^2+{H_y^{(0)}}^2)w_{z'z'}^{(1)} \tag{E.119}$$
$$0 = H_x^{(0)}P_{z'}^{(0)}+\mu(1+{H_x^{(0)}}^2+{H_y^{(0)}}^2)u_{z'z'}^{(1)} \tag{E.120}$$
$$0 = H_y^{(0)}P_{z'}^{(0)}+\mu(1+{H_x^{(0)}}^2+{H_y^{(0)}}^2)v_{z'z'}^{(1)} \tag{E.121}$$

which can be combined to show

$$u_{z'z'}^{(1)}=-H_x^{(0)}w_{z'z'}^{(1)} \tag{E.122}$$
$$v_{z'z'}^{(1)}=-H_y^{(0)}w_{z'z'}^{(1)}. \tag{E.123}$$

Differentiating (E.92) with respect to z' and utilizing (E.122) and (E.123) shows

$$(1+{H_x^{(0)}}^2+{H_y^{(0)}}^2)w_{z'z'}^{(1)}=0, \tag{E.124}$$

so

$$w^{(1)}_{z'z'} = 0. \tag{E.125}$$

$$P^{(0)}_{z'} = 0 \tag{E.126}$$

from (E.119),

$$u^{(1)}_{z'z'} = 0 \tag{E.127}$$

from (E.120), and

$$v^{(1)}_{z'z'} = 0 \tag{E.128}$$

from (E.121). Integrating (E.127) and (E.128) twice and utilizing the results in (E.117) yields

$$u^{(1)} = \bar{u}^{(1)} + z' f_6(x, y, t) \tag{E.129}$$

$$v^{(1)} = \bar{v}^{(1)} + z' f_7(x, y, t) \tag{E.130}$$

$$w^{(1)}_{z'} = H^{(0)}_x f_6 + H^{(0)}_y f_7 - \bar{u}_x - \bar{v}_y. \tag{E.131}$$

The dynamic boundary conditions at $O(\epsilon)$ require

$$\begin{aligned} -H^{(0)}_x(-P^{(0)} + 2\mu\bar{u}_x - 2\mu H^{(0)}_x f_6) - H^{(0)}_y \mu(\bar{u}_y - H^{(0)}_y f_6 + \bar{v}_x - H^{(0)}_x f_7) + \\ \mu(f_6 + w^{(0)}_x + H^{(0)}_x(\bar{u}_x + \bar{v}_y) - {H^{(0)}_x}^2 f_6 - H^{(0)}_x H^{(0)}_y f_7) = 0 \end{aligned} \tag{E.132}$$

$$\begin{aligned} -H^{(0)}_x \mu(\bar{u}_y - H^{(0)}_y f_6 + \bar{v}_x - H^{(0)}_x f_7) - H^{(0)}_y(-P^{(0)} + 2\mu\bar{v}_y - 2\mu H^{(0)}_y f_7) + \\ \mu(f_7 + w^{(0)}_y + H^{(0)}_y(\bar{u}_x + \bar{v}_y) - {H^{(0)}_y}^2 f_7 - H^{(0)}_x H^{(0)}_y f_6) = 0 \end{aligned} \tag{E.133}$$

$$\begin{aligned} -H^{(0)}_x \mu(f_6 + w^{(0)}_x + H^{(0)}_x(\bar{u}_x + \bar{v}_y) - {H^{(0)}_x}^2 f_6 - H^{(0)}_x H^{(0)}_y f_7) \\ -H^{(0)}_y \mu(f_7 + w^{(0)}_y + H^{(0)}_y(\bar{u}_x + \bar{v}_y) - {H^{(0)}_y}^2 f_7 - H^{(0)}_x H^{(0)}_y f_6) \\ -P^{(0)} + 2\mu(H^{(0)}_x f_6 + H^{(0)}_y f_7 - \bar{u}_x - \bar{v}_y) = 0. \end{aligned} \tag{E.134}$$

Rearranging (E.132) and (E.133) yields

$$\mu(1 + {H^{(0)}_x}^2 + {H^{(0)}_y}^2) f_6 = -H^{(0)}_x P^{(0)} + \mu\left[H^{(0)}_x \bar{u}_x - H^{(0)}_x \bar{v}_y + H^{(0)}_y(\bar{u}_y + \bar{v}_x) - w^{(0)}_x\right] \tag{E.135}$$

$$\mu(1 + {H^{(0)}_x}^2 + {H^{(0)}_y}^2) f_7 = -H^{(0)}_y P^{(0)} + \mu\left[H^{(0)}_y \bar{v}_y - H^{(0)}_y \bar{u}_x + H^{(0)}_x(\bar{u}_y + \bar{v}_x) - w^{(0)}_y\right], \tag{E.136}$$

and then plugging into (E.134) gives

$$P^{(0)} = 2\mu\left(\bar{u}_x + \bar{v}_y\right) - \mu\frac{D}{Dt}\left[\ln\left(1 + {H^{(0)}_x}^2 + {H^{(0)}_y}^2\right)\right]. \tag{E.137}$$

Plugging back into (E.135) and (E.136) yields

$$f_6 = \frac{H^{(0)}_x(2\bar{u}_x + \bar{v}_y) + H^{(0)}_y \bar{u}_y + H^{(0)}_x \frac{D}{Dt}\left[\ln\left(1 + {H^{(0)}_x}^2 + {H^{(0)}_y}^2\right)\right] - \frac{DH^{(0)}_x}{Dt}}{1 + {H^{(0)}_x}^2 + {H^{(0)}_y}^2} \tag{E.138}$$

$$f_7 = \frac{H_y^{(0)}(\bar{u}_x + 2\bar{v}_y) + H_x^{(0)}\bar{v}_x + H_y^{(0)}\frac{D}{Dt}\left[\ln\left(1 + {H_x^{(0)}}^2 + {H_y^{(0)}}^2\right)\right] - \frac{DH_y^{(0)}}{Dt}}{1 + {H_x^{(0)}}^2 + {H_y^{(0)}}^2}. \quad \text{(E.139)}$$

The kinematic boundary condition at $O(\epsilon)$ requires

$$w^{(1)}\Big|_{z'=H\pm\frac{1}{2}h} = H_t^{(1)} \pm \tfrac{1}{2}h_t^{(0)} + u^{(1)}H_x^{(0)} + u^{(0)}H_x^{(1)} + v^{(1)}H_y^{(0)} + v^{(0)}H_y^{(1)} \pm \tfrac{1}{2}u^{(0)}h_x^{(0)} \pm \tfrac{1}{2}v^{(0)}h_y^{(0)}. \quad \text{(E.140)}$$

Taking the difference between the upper and lower boundary conditions yields

$$h^{(0)}\left(H_x^{(0)}f_6 + H_y^{(0)}f_7 - \bar{u}_x - \bar{v}_y\right) = h_t^{(0)} + h^{(0)}f_6H_x^{(0)} + h^{(0)}f_7H_y^{(0)} + \bar{u}h_x^{(0)} + \bar{v}h_y^{(0)} \quad \text{(E.141)}$$

or

$$\frac{1}{h^{(0)}}\frac{Dh^{(0)}}{Dt} = -\bar{u}_x - \bar{v}_y = -\nabla\cdot\vec{\bar{u}}. \quad \text{(E.142)}$$

Henceforth, superscripts '(0)' will be dropped for convenience. All unspecified variable are assumed to be leading order. *In summary*:

$$u = \bar{u} \quad \text{(E.143)}$$

$$v = \bar{v} \quad \text{(E.144)}$$

$$w = H_t + \bar{u}H_x + \bar{v}H_y \quad \text{(E.145)}$$

$$P = 2\mu\left(\bar{u}_x + \bar{v}_y\right) - \mu\frac{D}{Dt}\left[\ln\left(1 + H_x^2 + H_y^2\right)\right] \quad \text{(E.146)}$$

$$u^{(1)} = \bar{u^{(1)}} + z'f_6(x,y,t) \quad \text{(E.147)}$$

$$v^{(1)} = \bar{v^{(1)}} + z'f_7(x,y,t) \quad \text{(E.148)}$$

$$f_6 = \frac{H_x(2\bar{u}_x + \bar{v}_y) + H_y\bar{u}_y + H_x\frac{D}{Dt}\left[\ln\left(1 + H_x^2 + H_y^2\right)\right] - \frac{DH_x}{Dt}}{1 + H_x^2 + H_y^2} \quad \text{(E.149)}$$

$$f_7 = \frac{H_y(\bar{u}_x + 2\bar{v}_y) + H_x\bar{v}_x + H_y\frac{D}{Dt}\left[\ln\left(1 + H_x^2 + H_y^2\right)\right] - \frac{DH_y}{Dt}}{1 + H_x^2 + H_y^2} \quad \text{(E.150)}$$

E.2.4 Depth-integrated force and moment equilibrium

Taking force and moment balances on depth-integrated unit of sheet as shown in Figure 2-1 yields

$$\sum F_z = 0 = Q_{x,x} + Q_{y,y} \quad \text{(E.151)}$$

$$\sum F_x = 0 = \frac{\partial}{\partial x}[h(2\mu\bar{u}_x - P - 2\mu H_x f_6)] + \frac{\partial}{\partial y}[h\mu(\bar{u}_y + \bar{v}_x - H_y f_6 - H_x f_7)] \quad \text{(E.152)}$$

$$\sum F_y = 0 = \frac{\partial}{\partial x}[h\mu(\bar{u}_y + \bar{v}_x - H_y f_6 - H_x f_7)] +$$
$$\frac{\partial}{\partial y}[h(2\mu\bar{v}_y - P - 2\mu H_y f_7)] \tag{E.153}$$
$$\sum M_y = 0 = -\frac{\partial}{\partial x}[Hh(2\mu\bar{u}_x - P - 2\mu H_x f_6)] -$$
$$\frac{\partial}{\partial y}[Hh\mu(\bar{u}_y + \bar{v}_x - H_y f_6 - H_x f_7)] + Q_x \tag{E.154}$$
$$\sum M_x = 0 = -\frac{\partial}{\partial x}[Hh\mu(\bar{u}_y + \bar{v}_x - H_y f_6 - H_x f_7)] -$$
$$\frac{\partial}{\partial y}[Hh(2\mu\bar{v}_y - P - 2\mu H_y f_7)] + Q_y. \tag{E.155}$$

Using (E.155) and (E.154) to provide expressions for Q_x and Q_y in the (E.152), (and using (E.152) and (E.152) to cancel terms) yields

$$H_{xx}T_{11} + 2H_{xy}T_{12} + H_{yy}T_{22} = 0. \tag{E.156}$$

(E.152) and (E.152) can be rewritten

$$\frac{\partial T_{11}}{\partial x} + \frac{\partial T_{12}}{\partial y} = 0 \tag{E.157}$$

$$\frac{\partial T_{12}}{\partial x} + \frac{\partial T_{22}}{\partial y} = 0, \tag{E.158}$$

where

$$T_{11} \equiv [2\mu\bar{u}_x - P - 2\mu H_x f_6]h \tag{E.159}$$
$$T_{22} \equiv [2\mu\bar{v}_y - P - 2\mu H_y f_7]h \tag{E.160}$$
$$T_{12} \equiv \mu[\bar{u}_y + \bar{v}_x - H_y f_6 - H_x f_7]h. \tag{E.161}$$

E.3 Gravity and surface tension effects

Now let us consider the effects of gravity and surface tension. To leading order, the traction on each surface due to surface tension is

$$\vec{T}_\gamma^{\pm} = 2\gamma^{\pm}\kappa\vec{n}^{+}, \tag{E.162}$$

the surface tension times twice the mean curvature acting in the direction of the upward normal to the center surface of the sheet,

$$2\kappa \equiv \frac{(1+H_y^2)H_{xx} - 2H_xH_yH_{xy} + (1+H_x^2)H_{yy}}{(1+H_x^2+H_y^2)^{3/2}}. \tag{E.163}$$

The traction due to gravity exerted on the lower surface is

$$\vec{T}_G = -\rho g H \vec{n}^+ \tag{E.164}$$

where $g > 0$. These tractions appear in the dynamic boundary conditions:

$$-H_x(-P + 2\mu u_x) - H_y\mu(u_y + v_x) + \mu(u_z + w_x) = \mp 2H_x\gamma^{\pm}\kappa + (\rho g H H_x)_- \tag{E.165}$$

$$-H_x\mu(u_y + v_x) - H_y(-P + 2\mu v_y) + \mu(v_z + w_y) = \mp 2H_y\gamma^{\pm}\kappa + (\rho g H H_y)_- \tag{E.166}$$

$$-H_x\mu(u_z + w_x) - H_y\mu(v_z + w_y) - P + 2\mu w_z = \mp 2\gamma^{\pm}\kappa + (\rho g H)_- \tag{E.167}$$

where the "$-$" subscript indicates that the gravity terms only appear in the boundary conditions on the lower surface.

Gravity is characterized by the dimensionless group

$$G \equiv \frac{3\rho g L^2}{\mu U}, \tag{E.168}$$

and surface tension is characterized by

$$\Gamma \equiv 3\frac{\gamma^+ + \gamma^-}{\mu U}. \tag{E.169}$$

Let us assume that both G and Γ are small compared to unity. In this case, the new gravity and surface tension terms in the dynamic boundary conditions do not contribute at leading or second order, and, as a result, the solutions above for the leading and second order velocities and the leading order pressure are unchanged. If G or Γ are smaller than $O(\epsilon)$, then they will not contribute to the above force or momentum balances either. Let us consider the case where they are $O(\epsilon)$. Gravity and surface tension will exert forces on the depth-integrated sheet unit equal to their traction times the exposed surface area of the sheet. To leading order, the exposed surface area of the sheet unit with length dx and width dy is given by

$$A = dxdy\sqrt{1 + H_x^2 + H_y^2}. \tag{E.170}$$

To leading order, the new force and moment balances are

$$\sum F_z = 0 = Q_{x,x} + Q_{y,y} - \rho g H + 2(\gamma^+ + \gamma^-)\kappa \tag{E.171}$$

$$\sum F_x = 0 = \frac{\partial T_{11}}{\partial x} + \frac{\partial T_{12}}{\partial y} + \rho g H H_x - 2H_x(\gamma^+ + \gamma^-)\kappa \tag{E.172}$$

$$\sum F_y = 0 = \frac{\partial T_{12}}{\partial x} + \frac{\partial T_{22}}{\partial y} + \rho g H H_y - 2H_y(\gamma^+ + \gamma^-)\kappa \tag{E.173}$$

$$\sum M_y = 0 = -\frac{\partial(HT_{11})}{\partial x} - \frac{\partial(HT_{12})}{\partial y} - \rho g H H_x + 2HH_x(\gamma^+ + \gamma^-)\kappa + Q_x \tag{E.174}$$

$$\sum M_x = 0 = -\frac{\partial(HT_{12})}{\partial x} - \frac{\partial(HT_{22})}{\partial y} - \rho g H H_y + 2HH_y(\gamma^+ + \gamma^-)\kappa + Q_y. \quad \text{(E.175)}$$

Once again using the in-plane force balances, (E.172) and (E.173), to cancel terms in the moment balances, (E.174) and (E.175), leads to

$$Q_x = H_x T_{11} + H_y T_{12} \quad \text{(E.176)}$$

$$Q_y = H_x T_{12} + H_y T_{22}. \quad \text{(E.177)}$$

Using (E.176) and (E.177) in (E.171) and canceling terms using (E.172) and (E.173) once more leads to

$$\frac{H_{xx}T_{11} + 2H_{xy}T_{12} + H_{yy}T_{22}}{1 + H_x^2 + H_y^2} - \rho g H + 2(\gamma^+ + \gamma^-)\kappa = 0. \quad \text{(E.178)}$$

E.3.1 Scaling argument for saturation amplitude

Let us expand (E.159), (E.160), and (E.161):

$$T_{11} = \frac{\mu h}{1 + H_x^2 + H_y^2}\Big[(1 + H_y^2)(4\bar{u}_x + 2\bar{v}_y) - 2H_x H_y \bar{u}_y + 2(1 + H_y^2)\frac{D}{Dt}\Big[\ln(1 + H_x^2 + H_y^2)\Big] - \frac{DH_y^2}{Dt}\Big] \quad \text{(E.179)}$$

$$T_{22} = \frac{\mu h}{1 + H_x^2 + H_y^2}\Big[(1 + H_x^2)(2\bar{u}_x + 4\bar{v}_y) - 2H_x H_y \bar{v}_x + 2(1 + H_x^2)\frac{D}{Dt}\Big[\ln(1 + H_x^2 + H_y^2)\Big] - \frac{DH_x^2}{Dt}\Big] \quad \text{(E.180)}$$

$$T_{12} = \frac{\mu h}{1 + H_x^2 + H_y^2}\Big[(1 + H_x^2)\bar{u}_y + (1 + H_y^2)\bar{v}_x - 2H_x H_y(\bar{u}_x + \bar{v}_y) - H_x H_y(\bar{u}_y + \bar{v}_x) + \frac{DH_x H_y}{Dt} - 2H_x H_y \frac{D}{Dt}\Big[\ln(1 + H_x^2 + H_y^2)\Big]\Big]. \quad \text{(E.181)}$$

Thinking about a rectilinear sheet being sheared by two parallel walls a distance $2L$ apart moving in opposite directions, each with speed U, let us now employ a new set of axes, x and y, oriented such that the x-axis lies parallel to the crests of the wrinkles, and the y-axis lies perpendicular to the crests of the wrinkles. In these coordinates, all four components of the velocity gradient will be of roughly the same order, $\dot{\gamma} \equiv U/L$. Call H the amplitude of the wrinkles and λ their wavelength. Utilizing this scaling,

$$H_{xx}T_{11} \sim \frac{\mu h H \dot{\gamma}}{L^2\left(1 + \frac{H^2}{L^2} + \frac{H^2}{\lambda^2}\right)}\left[\left(1 + \frac{H^2}{\lambda^2}\right) + \frac{H^2}{\lambda L} +\right.$$

$$\frac{1+\frac{H^2}{\lambda^2}}{1+\frac{H^2}{\lambda^2}+\frac{H^2}{L^2}}\left[\frac{H^2}{\lambda^3}+\frac{H^2}{\lambda^2 L}+\frac{H^2}{\lambda L^2}+\frac{H^2}{L^3}\right]L+L\left[\frac{H^2}{\lambda^3}+\frac{H^2}{\lambda^2 L}\right]\Bigg] \tag{E.182}$$

$$H_{yy}T_{22}\sim\frac{\mu h H\dot{\gamma}}{\lambda^2\left(1+\frac{H^2}{L^2}+\frac{H^2}{\lambda^2}\right)}\left[\left(1+\frac{H^2}{L^2}\right)+\frac{H^2}{\lambda L}+\right.$$
$$\left.\frac{1+\frac{H^2}{L^2}}{1+\frac{H^2}{\lambda^2}+\frac{H^2}{L^2}}\left[\frac{H^2}{\lambda^3}+\frac{H^2}{\lambda^2 L}+\frac{H^2}{\lambda L^2}+\frac{H^2}{L^3}\right]L+L\left[\frac{H^2}{L^3}+\frac{H^2}{L^2\lambda}\right]\right] \tag{E.183}$$

$$H_{xy}T_{12}\sim\frac{\mu h H\dot{\gamma}}{L\lambda\left(1+\frac{H^2}{L^2}+\frac{H^2}{\lambda^2}\right)}\left[1+\frac{H^2}{\lambda^2}+\frac{H^2}{L^2}\right.$$
$$\left.+\frac{H^2}{\lambda L}\left(1+\frac{\frac{H^2}{\lambda^3}+\frac{H^2}{\lambda^2 L}+\frac{H^2}{\lambda L^2}+\frac{H^2}{L^3}}{1+\frac{H^2}{L^2}+\frac{H^2}{\lambda^2}}L\right)+LH^2\left(\frac{1}{L\lambda^2}+\frac{1}{\lambda L^2}\right)\right]. \tag{E.184}$$

After noting that gravity has a much more significant effect than capillarity for reasonable experimental values of the parameters, the vertical force balance, (E.171), requires

$$\frac{H_{xx}T_{11}+H_{xy}T_{12}+H_{yy}T_{22}}{1+\frac{H^2}{L^2}+\frac{H^2}{\lambda^2}}\sim\rho g H. \tag{E.185}$$

For $H\sim\lambda\sim L$, the scaling reduces to the following:

$$\rho g H\sim\frac{\dot{\gamma}\mu h}{H} \tag{E.186}$$

or

$$H\sim\sqrt{\frac{\dot{\gamma}\mu h}{\rho g}} \tag{E.187}$$

so that for $\dot{\gamma}=U/L$

$$H\sim\sqrt[3]{\frac{\mu U h}{\rho g}}. \tag{E.188}$$

Appendix F

Numerical methods

This appendix describes in detail the numerical/computational methods employed in the solution of the equations of Chapter 3, Chapter 4, Chapter 6, and Appendix C. All calculations were done using Matlab.

F.1 Spectral collocation

Most computational schemes rely upon knowing the values of the field variables at only a finite number of points. In order to solve a differential equation, a numerical method requires a mechanism for measuring the derivative of the discretized field variables. Collocation methods approximate the derivative as the derivative of a function that interpolates the discrete values of the field variable. The collocation methods employed in this thesis utilize two types of interpolating functions, Fourier modes and Chebyshev polynomials. Fourier modes are well suited to periodic domains such as the azimuthal direction in the annular case and the longitudinal direction in the rectilinear case. Fourier modes are particularly well suited to these problems because the discretely represented functions are in fact Fourier wave forms of varying wavenumber. Chebyshev polynomial are employed in the radial direction in the annular case, in the cross-channel direction in the rectilinear case, and in the viscous catenary. The Chebyshev polynomials utilize a non-uniform distribution of discrete points biased toward the boundaries. Favoring the boundary region in distributing the discrete points allows the method to devote more resolution to the regions near the walls where in all three of these problems the geometry changes most rapidly. Representing the discrete valued field variable as a vector, the discrete derivatives can be applied as matrices multiplying the field variable vector so that for example

$$\frac{\partial f(x)}{\partial x} \rightarrow D_x \vec{f}, \tag{F.1}$$

where f is a function of x, $\vec{f}$ is the vector of discrete values of f, and D_x is the x-derivative matrix. The specific derivative matrices used here were calculated using the programs in Trefethen's book [32].

For time discretization, the numerical methods of this thesis utilize a finite-

difference method. Finite-difference methods approximate derivatives using truncated Taylor series. The particular finite-difference scheme used here is known as backward Euler or implicit Euler which is considered highly stable. Euler time stepping uses a two point finite-difference to represent time derivatives in the following fashion:

$$\frac{\partial f(t)}{\partial t} = \frac{f(t+\Delta t) - f(t)}{\Delta t}, \tag{F.2}$$

where f is a function with time dependence, and Δt is the discrete time step. Backward Euler specifies that, of the two times present in the discrete time derivative, all terms in the equation not subject to time differentiation be evaluated at the later time, $t + \Delta t$.

F.2 Annular sheet

The spatially discrete version of (3.13) is

$$\frac{12A}{h^2}\left(\frac{D_\theta \vec{H}}{r^4} - \frac{D_\theta D_r \vec{H}}{r^3}\right) + \frac{3G\vec{H}}{\epsilon^2 h^3} + \frac{3\Gamma\left(\frac{1}{r}D_r + D_r^2 + \frac{1}{r^2}D_\theta^2\right)\vec{H}}{\epsilon^2 h^3} =$$
$$\left(D_r^4 + \frac{2}{r}D_r^3 + \frac{2}{r^2}D_r^2 D_\theta^2 + \frac{1}{r^3}D_r + \frac{4}{r^4}D_\theta^2 + \frac{1}{r^4}D_\theta^4 - \frac{1}{r^2}D_r^2 - \frac{2}{r^3}D_r D_\theta^2\right)\vec{H}_t. \tag{F.3}$$

The homogeneous Dirichlet boundary conditions are imposed by simply eliminating from the equation the elements of the matrices and vectors corresponding to boundary points. Periodicity is implicitly contained within the derivative matrices. The homogeneous Neumann boundary conditions are imposed by replacing D_r^4 by the special operator

$$D_r^4 \to \frac{1}{1-r^2}\left((1-r^2)D_r^4 - 8rD_r^3 - 12D_r^2\right) \tag{F.4}$$

suggested by Trefethen which effectively treats the Chebyshev polynomial interpolant as if it were two polynomial orders higher but restricted to have a slope of zero at its endpoints.

To simulate the evolution of the sheet, in (F.3) $\vec{H}_t$ is replaced by $\frac{\vec{H}(t+\Delta t)-\vec{H}(t)}{\Delta t}$, all the other terms are evaluated at $t = t + \Delta t$, and the resulting linear equation is solved for $\vec{H}(t+\Delta t)$. In this fashion, the shape of the sheet at $t + \Delta t$ can be found given the shape of the sheet at t. For given initial conditions, the shape of the sheet at $t = n\Delta t$ can be found by solving the equation n times to evolve the sheet through n time steps. The maximally growing azimuthal wavenumber disturbance for a given set of conditions can be discerned by setting the initial condition to equally contain all representable azimuthal wavenumbers and stepping through time until a single mode dominates the rest. The mode asserting itself is that with the highest growth rate.

The threshold of stability was located using a bisection method on the shear rate. If all modes decay, the shear rate is below the threshold. If any mode grows, the shear

rate is above the threshold. By choosing two limiting shear rates, one above and one below the threshold, and progressively halving the gap between them by simulating the shear rate midway between them such that the threshold value is sandwiched between an ever narrowing set of shear rates, the threshold value was located.

An alternative to the simulation method is the eigenvalue method. Every step of discretization introduces some error inherent in the difference between the continuous reality and the discrete representation. The eigenvalue method operates on the spatially discrete and temporally continuous representation thus eliminating time discretization and its concomitant error. The eigenvalue method extracts the mode shapes and their growth rates directly out of the discrete spatial operator. The eigenmodes are mode shapes, H, for which $H_t = \sigma H$ or in the discrete representation $\vec{H}_t = \sigma \vec{H}$ where σ, the eigenvalue, is the growth rate. For a given set of conditions, the eigenmode with the highest eigenvalue is the fastest growing, and, therefore, the most unstable. (F.3) can be written as just $A\vec{H}_t = B\vec{H}$ where A and B are matrices. The Matlab `eig` function calculates all of the eigenmodes and their eigenvectors for the pair of operators A and B. The same bisection method employed in the simulation method was used to locate the threshold of stability using the eigenvalue method and confirmed the results of the simulation method. All results presented in Chapter 3 were calculated using the eigenvalue method.

For the case when surface tension and gravity are absent presented in Appendix C, (C.6) and (C.8) can be solved for each aspect ratio and wavenumber using Matlab's minimization routine. In general, the roots of (C.6) and therefore the components of (C.8) are complex, so a simple zero finding routine is insufficient. Matlab's minimization routine was used to find S that minimizes the absolute value of the determinant. In this fashion, the growth rates of each mode for each aspect ratio were determined. These results are presented in Appendix C. The simulation and eigenvalue methods were also used to calculate the growth rates in the absence of gravity and surface tension and produced results matching those in Appendix C providing support for their results in the more general case where gravity and surface tension were included.

F.3 Rectilinear sheet

The rectilinear problem was solved using the eigenvalue approach as described for the annular problem. Because in the rectilinear problem there are no factors of r in the linear stability equation, (4.11), even with gravity and surface tension, the problem can be approached directly through the simultaneous solution of (4.14) and (4.18). However, due to the difficulty of filtering out inadmissible roots of (4.14) (such as double roots which change the form of the solutions to (4.11) and therefore change the entries in (4.18)), the eigenvalue approach provides a more tractable way of dealing with the stability problem. The semi-discrete version of (4.5) is

$$\left(D_x^4 + 2D_x^2 D_y^2 + D_y^4\right)\vec{H}_t = \Gamma\left(D_x^2 + D_y^2\right)\vec{H} - G\vec{H} + 6D_x D_y \vec{H} \qquad \text{(F.5)}$$

subject to periodic boundary conditions in the x-direction and homogeneous Dirichlet and Neumann boundary conditions in the y-direction. The boundary conditions are imposed exactly as above. Periodicity is implicit in the construction of the derivative matrices in the x-direction for the Fourier modes. The homogeneous Dirichlet conditions are imposed by eliminating matrix and vector entries corresponding to points on the walls. The homogeneous Neumann conditions are imposed by utilizing the special form of D_y^4

$$D_y^4 \to \frac{1}{1-y^2}\left((1-y^2)D_y^4 - 8yD_y^3 - 12D_y^2\right) \tag{F.6}$$

F.4 Viscous catenary

The viscous catenary problem only contains one independent spatial variable, x. The evolution of the catenary is calculated using the simulation method described above. In this case, in addition to differentiation, integration of the discrete function is required. The quadrature scheme utilized is a Clenshaw-Curtis scheme suggested by Trefethen [32] which provides optimal accuracy for use with Chebyshev polynomials and their evaluation points as used here and takes the form of an inner product

$$\int f(x)dx \to \vec{w}^T\vec{f}. \tag{F.7}$$

where $\vec{w}$ is a vector of quadrature weights calculated using Trefethen's program `clencurt.m`, and the superscript T indicates transposition. The discrete version of (6.32) is

$$\frac{1}{32}\epsilon^3 D_x^2\left(\frac{\vec{\theta}(t+\Delta t)-\vec{\theta}(t)}{\Delta t}\right) - \frac{1}{2}\epsilon\vec{\theta}(t+\Delta t)\vec{w}^T\left(\frac{\vec{\theta}^2(t+\Delta t)-\vec{\theta}^2(t)}{\Delta t}\right) + \vec{x} = 0. \tag{F.8}$$

In this case, the discrete equation (F.8) is nonlinear and cannot be solved simply by Gaussian elimination as in the previous cases. Instead, $\vec{\theta}(t+\Delta t)$ is found using the Newton method for systems of nonlinear equations. The Newton method is an iterative method which starts from an initial guess of $\vec{\theta}(t+\Delta t)$ which in this case is $\vec{\theta}(t)$ and makes progressively better guesses by using a linear approximation to the equation. Specifically,

$$\vec{\theta}(t+\Delta t)^{n+1} = \vec{\theta}(t+\Delta t)^n - J^{-1}\vec{R}^n, \tag{F.9}$$

where the superscripts n and $n+1$ indicate the number of the guess in the iterative process, $\vec{\theta}(t+\Delta t)^0 = \vec{\theta}(t)$, $\vec{R}^n$ is the residual for guess n,

$$\vec{R}^n = \frac{1}{32}\epsilon^3 D_x^2\left(\frac{\vec{\theta}(t+\Delta t)^n-\vec{\theta}(t)}{\Delta t}\right) - \frac{1}{2}\epsilon\vec{\theta}(t+\Delta t)^n\vec{w}^T\left(\frac{\vec{\theta}^2(t+\Delta t)^n-\vec{\theta}^2(t)}{\Delta t}\right) + \vec{x}, \tag{F.10}$$

and J is the Jacobian of $\vec{R}^n$,

$$J = \frac{1}{32\Delta t}\epsilon^3 D_x^2 - \frac{1}{2}\epsilon\vec{w}^T\left(\frac{\vec{\theta}^2(t+\Delta t)^n - \vec{\theta}^2(t)}{\Delta t}\right) I - \epsilon\vec{\theta}(t+\Delta t)^n \frac{\vec{w\theta}^T(t+\Delta t)^n}{\Delta t}, \quad \text{(F.11)}$$

where I is the identity matrix, and $\vec{w\theta}$ is a vector with each component equal to the product of the corresponding components of $\vec{w}$ and $\vec{\theta}$. The iteration process is continued until $\vec{R}^n$ is smaller than a prescribed tolerance at which point $\vec{\theta}(t+\Delta t)$ is set equal to $\vec{\theta}(t+\Delta t)^n$.

The three contributions to the discrete equation, (F.8), can be evaluated separately to examine the relative importance of bending and stretching in each region. The forcing contribution from gravity is just $\vec{x}$. The bending resistance is

$$\frac{1}{32}\epsilon^3 D_x^2\left(\frac{\vec{\theta}(t+\Delta t) - \vec{\theta}(t)}{\Delta t}\right). \quad \text{(F.12)}$$

The stretching resistance is

$$-\frac{1}{2}\epsilon\vec{\theta}(t+\Delta t)\vec{w}^T\left(\frac{\vec{\theta}^2(t+\Delta t) - \vec{\theta}^2(t)}{\Delta t}\right). \quad \text{(F.13)}$$

At each point the two resistances must exactly balance the forcing, so the fraction of resistance due to bending as a function of position can be written

$$\frac{\frac{1}{32}\epsilon^3 D_x^2\left(\frac{\vec{\theta}(t+\Delta t)-\vec{\theta}(t)}{\Delta t}\right)}{\vec{x}} \quad \text{(F.14)}$$

where the fraction is intended to represent an element by element division. This is the method used to trace the evolution of the bending boundary layer.

Appendix G

Viscous tension field theory

E. Reissner developed a generalized tension field theory to describe how an effectively anisotropic medium reacts to imposed stresses in its plane [23]. In particular, he considers a linearly elastic medium in which everywhere the stiffness in one local direction is zero. This model accurately represents the reaction of a membrane subjected to shearing because shearing is equivalent to compression along one direction and tension in the orthogonal direction. The membrane will behave as an anisotropic medium because though the membrane has a finite tensile stiffness, the compressive stiffness and the bending stiffness of the membrane are zero, so the membrane effectively has a finite stiffness in the tensile direction and zero stiffness in the orthogonal compressive direction. The same model effectively approximates the behavior of a thin buckled sheet far from onset where the stresses applied to the sheet are resisted principally through tension since the bending and compressive stiffnesses of the material in the direction of buckling are compromised. Here the same approach is used to model the behavior of a thin viscous sheet buckled by applied shear loading.

Let us introduce an orthogonal curvilinear coordinate system set in the thin sheet with axes ξ and η corresponding to the principal plane stress axes and subscripts 1 and 2 to refer to quantities associated with them. Let h_1 and h_2 quantify the spacing of lines of constant ξ and lines of constant η respectively so that infinitesimal distances in the plane, ds, relate to the local coordinates through the following relation:

$$ds^2 = h_1^2 d\xi^2 + h_2^2 d\eta^2. \tag{G.1}$$

The orthogonality of the coordinate system requires satisfaction of the following constraint:

$$\frac{\partial}{\partial \eta}\left(\frac{1}{h_2}\frac{\partial h_1}{\partial \eta}\right) + \frac{\partial}{\partial \xi}\left(\frac{1}{h_1}\frac{\partial h_2}{\partial \xi}\right) = 0. \tag{G.2}$$

This constraint can be thought of as requiring that the sum of the angles in any closed coordinate quadrilateral be 2π.

Stress equilibrium in the medium can then be expressed as

$$\frac{\partial h_2 \sigma_1}{\partial \xi} - \sigma_2 \frac{\partial h_2}{\partial \xi} = 0 \tag{G.3}$$

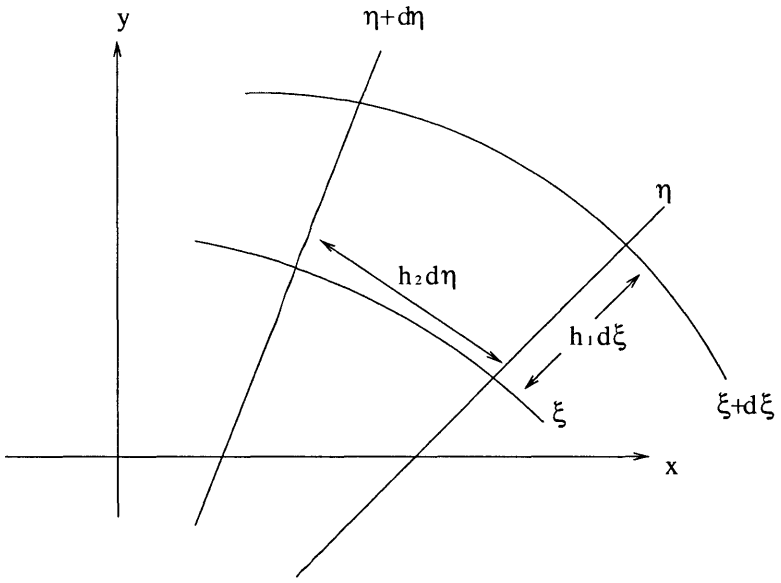

Figure G-1: Principle coordinates ξ and η

and

$$\frac{\partial h_1 \sigma_2}{\partial \eta} - \sigma_1 \frac{\partial h_1}{\partial \eta} = 0, \tag{G.4}$$

where σ_1 and σ_2 are the principal stresses. The strain-displacement relation and constitutive equations can be written as

$$\dot{\epsilon}_1 \equiv \frac{1}{h_1}\left(\frac{\partial u}{\partial \xi} + \frac{v}{h_2}\frac{\partial h_1}{\partial \eta}\right) = \frac{\tau_{11}}{E_1} = \frac{\sigma_1}{E_1}, \tag{G.5}$$

$$\dot{\epsilon}_2 \equiv \frac{1}{h_2}\left(\frac{\partial v}{\partial \eta} + \frac{u}{h_1}\frac{\partial h_2}{\partial \xi}\right) = \frac{\tau_{22}}{E_2} = \frac{\sigma_2}{E_2} \tag{G.6}$$

and

$$\dot{\gamma} \equiv h_1^2 \frac{\partial}{\partial \eta}\left(\frac{u}{h_1}\right) + h_2^2 \frac{\partial}{\partial \xi}\left(\frac{v}{h_2}\right) = 0. \tag{G.7}$$

where u and v are the velocities in the ξ and η directions, $\dot{\epsilon}$ is the strain rate, E is the stiffness, τ is the plane stress, and $\dot{\gamma}$ is the shear strain rate which must be 0 because the chosen axes are the principal axes.

Let us now consider the scenario of a sheared viscous annular sheet beyond the buckling threshold once the out-of-plane displacements have become large so that resistance to bending and compression in the compressive direction becomes small compared to the resistance to stretching in the tensile direction. Call η the compressive principal stress direction and ξ the tensile principal stress direction. At this late stage of wrinkling $E_1 >> E_2$, so let us write $E_2 = 0$. It follows that $\sigma_2 = 0$. Let us now write $E \equiv E_1$.

In this limit, equilibrium under deformation can only be supported by tension, hence "tension field theory." Working from the equilibrium equations, (G.3) and

(G.4), $\sigma_2 = 0$ implies

$$\frac{\partial h_2 \sigma_1}{\partial \xi} = 0 \tag{G.8}$$

so

$$\sigma_1 = \frac{g(\eta)}{h_2}, \tag{G.9}$$

and

$$\frac{\partial h_1}{\partial \eta} = 0 \tag{G.10}$$

so $h_1 = h_1(\xi)$.

Without affecting the directional properties of the (ξ, η) system, the scaling of the system can be changed such that $h_1 = 1$ everywhere. This makes lines of constant η straight because $h_1 = C$ implies that lines of constant ξ are locally parallel, so to maintain orthogonality, a line of constant η crossing a line of constant ξ must continue straight across to the next line of constant η. The orthogonality relation, (G.2), now reduces to

$$\frac{\partial}{\partial \xi}\left(\frac{\partial h_2}{\partial \xi}\right) = 0 \tag{G.11}$$

so

$$h_2 = \xi f_1(\eta) + f_2(\eta). \tag{G.12}$$

For our particular problem of the annulus, because of axisymmetry, the lines of constant η cannot be parallel, so $f_1(\eta) \neq 0$. Again a scale can be chosen without changing the characteristics of the (ξ, η) system such that $f_1(\eta) = 1$:

$$h_2 = \xi + f_2(\eta). \tag{G.13}$$

Utilizing (G.13) in (G.9) results in

$$\sigma_1 = \frac{g(\eta)}{\xi + f_2(\eta)} \tag{G.14}$$

which, in conjunction with the constitutive and strain-displacement relations, (G.5) and (G.6), yields

$$\frac{g(\eta)}{E(\xi + f_2(\eta))} = \frac{\partial u}{\partial \xi}, \tag{G.15}$$

so

$$u = \frac{g(\eta)}{E} \ln(\xi + f_2(\eta)) + \frac{h(\eta)}{E} \tag{G.16}$$

and

$$\frac{1}{\xi + f_2(\eta)} \frac{\partial v}{\partial \eta} = -\frac{g(\eta)}{E} \ln(\xi + f_2(\eta)) - \frac{h(\eta)}{E}. \tag{G.17}$$

The shear strain rate equation, (G.7), now reduces to

$$\frac{\partial u}{\partial \eta} = -h_2^2 \frac{\partial}{\partial \xi}\left(\frac{v}{h_2}\right) \tag{G.18}$$

or

$$\frac{\partial}{\partial \xi}\left(\frac{v}{h_2}\right) = -\frac{1}{(\xi + f_2(\eta))^2 E}\left(g'(\eta)\ln(\xi + f_2(\eta)) + \frac{g(\eta)f_2'(\eta)}{\xi + f_2(\eta)} + h'(\eta)\right). \tag{G.19}$$

Integrating,

$$\frac{v}{h_2} = \frac{1}{E}\left[k(\eta) + \frac{h'(\eta)}{h_2} + \frac{g(\eta)f_2'(\eta)}{2h_2^2} + g'(\eta)\left(\frac{\ln(\xi + f_2(\eta)}{h_2} + \frac{1}{h_2}\right)\right] \tag{G.20}$$

$$v = \frac{1}{E}\left[k(\eta)(\xi + f_2(\eta)) + h'(\eta) + \frac{g(\eta)f_2'(\eta)}{2(\xi + f_2(\eta)} + g'(\eta)\left[1 + \ln(\xi + f_2(\eta))\right]\right]. \tag{G.21}$$

Let us consider the relationship between the curvilinear coordinates and the fixed (r, θ) coordinates. We can write $r(\xi, \eta)$, $\theta(\xi, \eta)$, $\xi(r, \theta)$, and $\eta(r, \theta)$.

$$ds^2 = dx^2 + dy^2 \tag{G.22}$$

$$dx = d\xi\frac{\partial x}{\partial \xi} + d\eta\frac{\partial x}{\partial \eta} \tag{G.23}$$

$$dy = d\xi\frac{\partial y}{\partial \xi} + d\eta\frac{\partial y}{\partial \eta} \tag{G.24}$$

Along a line of constant η, $d\eta = 0$, so

$$ds^2 = d\xi^2\left(\frac{\partial x}{\partial \xi}\right)^2 + d\xi^2\left(\frac{\partial y}{\partial \xi}\right)^2 = h_1^2 d\xi^2 \tag{G.25}$$

$$\left(\frac{\partial x}{\partial \xi}\right)^2 + \left(\frac{\partial y}{\partial \xi}\right)^2 = 1. \tag{G.26}$$

Similarly,

$$\left(\frac{\partial x}{\partial \eta}\right)^2 + \left(\frac{\partial y}{\partial \eta}\right)^2 = (\xi + f_2(\eta))^2. \tag{G.27}$$

The slope of a line of constant η is

$$\frac{\frac{\partial y}{\partial \xi}}{\frac{\partial x}{\partial \xi}}, \tag{G.28}$$

and the slope of a line of constant ξ is

$$\frac{\frac{\partial y}{\partial \eta}}{\frac{\partial x}{\partial \eta}}. \tag{G.29}$$

Orthogonality requires these two slopes to be negative reciprocals:

$$\frac{\frac{\partial y}{\partial \xi}}{\frac{\partial x}{\partial \xi}} = -\frac{\frac{\partial x}{\partial \eta}}{\frac{\partial y}{\partial \eta}} \tag{G.30}$$

$$\frac{\partial x}{\partial \xi}\frac{\partial x}{\partial \eta} + \frac{\partial y}{\partial \xi}\frac{\partial y}{\partial \eta} = 0. \tag{G.31}$$

In polar coordinates

$$ds^2 = r^2 d\theta^2 + dr^2 \tag{G.32}$$

$$dr = d\xi \frac{\partial r}{\partial \xi} + d\eta \frac{\partial r}{\partial \eta} \tag{G.33}$$

$$d\theta = d\xi \frac{\partial \theta}{\partial \xi} + d\eta \frac{\partial \theta}{\partial \eta}. \tag{G.34}$$

Along a line of constant η, $d\eta = 0$, so

$$ds^2 = r^2 d\xi^2 \left(\frac{\partial \theta}{\partial \xi}\right)^2 + d\xi^2 \left(\frac{\partial r}{\partial \xi}\right)^2 = h_1^2 d\xi^2, \tag{G.35}$$

$$r^2 \left(\frac{\partial \theta}{\partial \xi}\right)^2 + \left(\frac{\partial r}{\partial \xi}\right)^2 = 1. \tag{G.36}$$

Similarly,

$$r^2 \left(\frac{\partial \theta}{\partial \eta}\right)^2 + \left(\frac{\partial r}{\partial \eta}\right)^2 = (\xi + f_2(\eta))^2, \tag{G.37}$$

$$x = r\cos\theta, \tag{G.38}$$

$$y = r\sin\theta. \tag{G.39}$$

Substituting into the Cartesian orthogonality relation, (G.31), yields

$$\frac{\partial r}{\partial \xi}\frac{\partial r}{\partial \eta} + r^2 \frac{\partial \theta}{\partial \xi}\frac{\partial \theta}{\partial \eta} = 0. \tag{G.40}$$

Lines of constant η are straight, so in the (r, θ) system they must take the form

$$r\sin\theta = m(\eta) r\cos\theta + b(\eta) \tag{G.41}$$

or

$$y = m(\eta)x + b(\eta). \tag{G.42}$$

On any line of constant η, $\Delta\xi$ is the distance along the line.

$$d\eta \frac{\partial h_2}{\partial \xi} = d\eta \tag{G.43}$$

is the angle between lines. If we choose $\eta = 0$ at a horizontal line, then η represents the angle of inclination of a line with respect to the horizontal. In this case

$$x = \xi\cos\eta + x_0(\eta), \tag{G.44}$$

$$y = \xi\sin\eta + y_0(\eta). \tag{G.45}$$

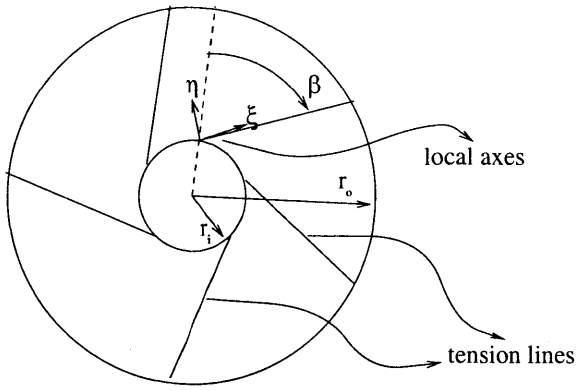

Figure G-2: Annular geometry

(G.44) and (G.45) already satisfy

$$\left(\frac{\partial x}{\partial \xi}\right)^2 + \left(\frac{\partial y}{\partial \xi}\right)^2 = 1. \tag{G.46}$$

Substituting (G.44) and (G.45) into

$$\left(\frac{\partial x}{\partial \eta}\right)^2 + \left(\frac{\partial y}{\partial \eta}\right)^2 = (\xi + f_2(\eta))^2 \tag{G.47}$$

yields

$$(-\xi \sin\eta + x_0'(\eta))^2 + (\xi \cos\eta + y_0'(\eta))^2 = (\xi + f_2(\eta))^2 . \tag{G.48}$$

Separately equating terms in equal powers of ξ,

$$x_0'^2 + y_0'^2 = f_2(\eta)^2, \tag{G.49}$$

and

$$-x_0' \sin\eta + y_0' \cos\eta = f_2(\eta). \tag{G.50}$$

Substituting (G.44) and G.45) into the orthogonality relation, (G.31), gives

$$x_0' \cos\eta + y_0' \sin\eta = 0 \tag{G.51}$$

or

$$x_0' = -y_0' \tan\eta. \tag{G.52}$$

Combining (G.52) with the (G.50) yields

$$y_0' = f_2(\eta) \cos\eta, \tag{G.53}$$

so

$$x_0' = -f_2(\eta) \sin\eta. \tag{G.54}$$

Now consider the annular geometry shown in Figure G-2. Every point on the

inner boundary must lie on a tension line, and, by symmetry, all of these tension lines must leave the inner boundary at the same angle β to the normal. Since these lines fill the space, and lines of constant η cannot intersect (except perhaps at a singular point), these are all of the tension lines.

The equations for $x(\xi,\eta)$ and $y(\xi,\eta)$ make lines of constant η of angle η to the x-axis passing through (x_0, y_0) with distance along the line from (x_0, y_0) parameterized by ξ. Each line must intersect the inner circle at an angle β to the radius (Figure G-2).

A point P on the inner boundary of the annulus will have Cartesian coordinates $(r_i\cos(\eta+\beta), r_i\sin(\eta+\beta))$ and curvilinear coordinates (ξ_0,η). Using the known form of the correlation between the two coordinate systems, (G.44) and (G.45),

$$r_i\cos(\eta+\beta) = x(\xi_0,\eta) = \xi_0(\eta)\cos\eta + x_0(\eta) \tag{G.55}$$

or

$$x_0(\eta) = r_i\cos\beta\cos\eta - r_i\sin\beta\sin\eta - \xi_0(\eta)\cos\eta. \tag{G.56}$$

Similarly

$$r_i\sin(\eta+\beta) = y(\xi_0,\eta) = \xi_0(\eta)\sin\eta + y_0(\eta) \tag{G.57}$$

or

$$y_0(\eta) = r_i\sin\beta\cos\eta + r_i\cos\beta\sin\eta - \xi_0(\eta)\sin\eta. \tag{G.58}$$

Differentiating,

$$x_0' = -r_i\cos\beta\sin\eta - r_i\sin\beta\cos\eta - \xi_0'(\eta)\cos\eta + \xi_0(\eta)\sin\eta = -f_2(\eta)\sin\eta, \tag{G.59}$$

so

$$f_2(\eta) = r_i\cos\beta + r_i\sin\beta\cot\eta + \xi_0'(\eta)\cot\eta - \xi_0(\eta), \tag{G.60}$$

and

$$y_0' = -r_i\sin\beta\sin\eta + r_i\cos\beta\cos\eta - \xi_0'(\eta)\sin\eta - \xi_0(\eta)\cos\eta = f_2(\eta)\cos\eta, \tag{G.61}$$

so

$$f_2(\eta) = r_i\cos\beta - r_i\sin\beta\tan\eta - \xi_0'(\eta)\tan\eta - \xi_0(\eta). \tag{G.62}$$

Equating the two expressions for $f_2(\eta)$, (G.60) and (G.62), results in

$$\xi_0'(\eta) = -r_i\sin\beta. \tag{G.63}$$

Integrating yields

$$\xi_0(\eta) = -\eta r_i\sin\beta + K, \tag{G.64}$$

so

$$f_2(\eta) = r_i\cos\beta + \eta r_i\sin\beta - K \tag{G.65}$$

$$x_0(\eta) = -r_i\sin\beta\sin\eta + f_2(\eta)\cos\eta \tag{G.66}$$

$$y_0(\eta) = r_i\sin\beta\cos\eta + f_2(\eta)\sin\eta \tag{G.67}$$

$$R_0 \equiv r_i\sin\beta \tag{G.68}$$

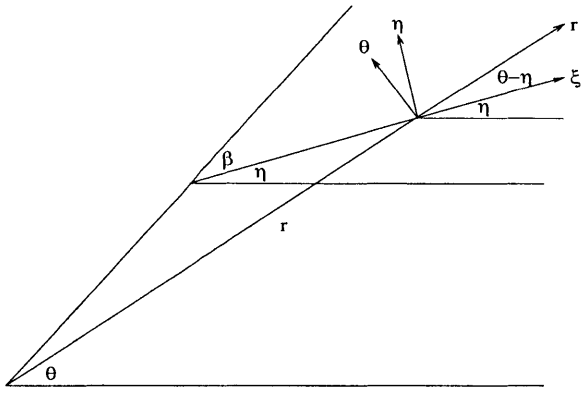

Figure G-3: Relation between (r, θ) and (ξ, η)

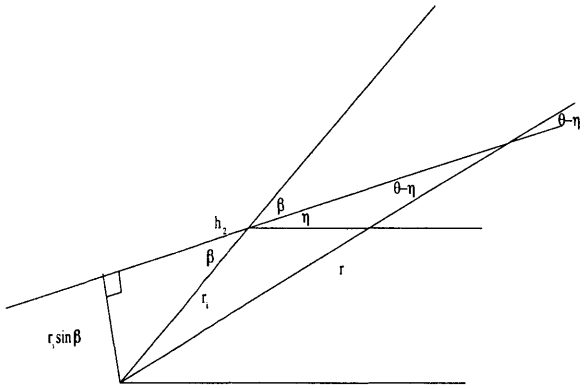

Figure G-4: Relation between $\theta - \eta$, r, R_o, and h_2

$$r^2 = x^2 + y^2 = \xi^2 + x_0^2 + y_0^2 + 2x_0\xi\cos\eta + 2y_0\xi\sin\eta = \\ \xi^2 + f_2(\eta)^2 + R_0^2 + 2\xi f_2(\eta) = (\xi + f_2(\eta))^2 + R_0^2 = h_2^2 + r_0^2 \tag{G.69}$$

$$h_2^2 = r^2 - R_0^2. \tag{G.70}$$

Returning to the velocities,

$$u = \frac{g(\eta)}{E}\ln h_2 + \frac{h(\eta)}{E} \tag{G.71}$$

$$v = \frac{1}{E}\left[k(\eta)h_2 + h'(\eta) + \frac{g(\eta)f_2'(\eta)}{2h_2} + g'(\eta)\left[1 + \ln h_2\right]\right]. \tag{G.72}$$

Figure G-3 illustrates the relationship between the two coordinate frames. In the (r, θ) frame of reference, the velocities in the r and θ directions, u_r and u_θ, are

$$u_r = v\sin(\theta - \eta) + u\cos(\theta - \eta) \tag{G.73}$$

$$u_\theta = v\cos(\theta - \eta) - u\sin(\theta - \eta). \tag{G.74}$$

From Figure G-4,

$$\sin(\theta - \eta) = \frac{R_0}{r} \tag{G.75}$$

$$\cos(\theta - \eta) = \frac{h_2}{r}. \tag{G.76}$$

$$Eu_r = k(\eta)\frac{h_2 R_0}{r} + h'(\eta)\frac{R_0}{r} + \frac{g(\eta)R_0^2}{2h_2 r} + g'(\eta)(1 + \ln h_2)\frac{R_0}{r} + g(\eta)(\ln h_2)\frac{h_2}{r} + h(\eta)\frac{h_2}{r} \tag{G.77}$$

$$Eu_\theta = k(\eta)\frac{h_2^2}{r} + h'(\eta)\frac{h_2}{r} + \frac{g(\eta)R_0}{2r} + g'(\eta)(1 + \ln h_2)\frac{h_2}{r} - g(\eta)(\ln h_2)\frac{R_0}{r} - h(\eta)\frac{R_0}{r} \tag{G.78}$$

We have in this scenario an axisymmetric state of stress, $\sigma_1 = f(r)$. The current stress relation states

$$\sigma_1 = \frac{g(\eta)}{h_2}, \tag{G.79}$$

so it must be the case that $g(\eta) = g_0$.

$$rEu_r = k(\eta)h_2 R_0 + h'(\eta)R_0 + \frac{g_0 R_0^2}{2h_2} + g_0(\ln h_2)h_2 + h(\eta)h_2 \tag{G.80}$$

$$rEu_\theta = k(\eta)h_2^2 + h'(\eta)h_2 + \frac{g_0 R_0}{2} - g_0(\ln h_2)R_0 - h(\eta)R_0 \tag{G.81}$$

The displacements must also be axisymmetric:

$$\frac{\partial u_r(r,\eta)}{\partial \eta} = 0 \tag{G.82}$$

so

$$k'(\eta)h_2 R_0 + h''(\eta)R_0 + h'(\eta)h_2 = 0, \tag{G.83}$$

and

$$\frac{\partial u_\theta(r,\eta)}{\partial \eta} = 0 \tag{G.84}$$

so

$$k'(\eta)h_2^2 + h''(\eta)h_2 - h'(\eta)R_0 = 0. \tag{G.85}$$

Multiplying (G.85) by R_0/h_2 and subtracting it from (G.83) demonstrates that $h'(\eta) = 0$, so $h(\eta) = h_0$, $k'(\eta) = 0$, and $k(\eta) = k_0$.

$$u_r = \frac{1}{Er}\left[k_0 h_2 R_0 + \frac{g_0 R_0^2}{2h_2} + g_0(\ln h_2)h_2 + h_0 h_2\right] \tag{G.86}$$

$$u_\theta = \frac{1}{Er}\left[k_0 h_2^2 + \frac{g_0 R_0}{2} - g_0(\ln h_2)R_0 - h_0 R_0\right] \tag{G.87}$$

If the sheet is sheared by rotating the inner boundary of the annulus, then the

boundary conditions on the velocities of the sheet are

$$u_r(r_i) = u_r(r_o) = u_\theta(r_o) = 0 \tag{G.88}$$

and

$$u_\theta(r_i) = \Omega r_i; \tag{G.89}$$

or

$$k_0 h_2(r_i) R_0 + g_0 \left(\frac{R_0^2}{2h_2(r_i)} + (\ln h_2(r_i)) h_2(r_i) \right) + h_0 h_2(r_i) = 0 \tag{G.90}$$

$$k_0 h_2(r_o) R_0 + g_0 \left(\frac{R_0^2}{2h_2(r_o)} + (\ln h_2(r_o)) h_2(r_o) \right) + h_0 h_2(r_o) = 0 \tag{G.91}$$

$$k_0 h_2^2(r_o) + g_0 \left(\frac{R_0}{2} - (\ln h_2(r_o)) R_0 \right) - h_0 R_0 = 0 \tag{G.92}$$

$$k_0 h_2^2(r_i) + g_0 \left(\frac{R_0}{2} - (\ln h_2(r_i)) R_0 \right) - h_0 R_0 = \Omega E r_i^2. \tag{G.93}$$

Since (G.90), (G.91), and (G.92) are homogeneous and linear in k_0, g_0, and h_0, in order to have nontrivial solutions, the determinant of the system of these three equations must be zero:

$$\begin{vmatrix} h_2(r_i) R_0 & \frac{R_0^2}{2h_2(r_i)} + (\ln h_2(r_i)) h_2(r_i) & h_2(r_i) \\ h_2(r_o) R_0 & \frac{R_0^2}{2h_2(r_o)} + (\ln h_2(r_o)) h_2(r_o) & h_2(r_o) \\ h_2^2(r_o) & \frac{R_0}{2} - (\ln h_2(r_o)) R_0 & -R_0 \end{vmatrix} = 0 \tag{G.94}$$

$$\begin{vmatrix} R_0 & \frac{R_0^2}{2h_2^2(r_i)} + \ln h_2(r_i) & 1 \\ R_0 & \frac{R_0^2}{2h_2^2(r_o)} + \ln h_2(r_o) & 1 \\ R_0^2 + h_2^2(r_o) & \frac{R_0^3}{2h_2^2(r_o)} \frac{R_0}{2} & 0 \end{vmatrix} = 0 \tag{G.95}$$

$$\begin{vmatrix} R_0 & \frac{R_0^2}{2h_2^2(r_i)} + \ln h_2(r_i) & 1 \\ 0 & \frac{R_0^2}{2} \left(\frac{1}{h_2^2(r_o)} - \frac{1}{h_2^2(r_i)} \right) + \ln \left(\frac{h_2(r_o)}{h_2(r_i)} \right) & 0 \\ R_0^2 + h_2^2(r_o) & \frac{R_0^3}{2h_2^2(r_o)} \frac{R_0}{2} & 0 \end{vmatrix} = 0 \tag{G.96}$$

$$\left(R_0^2 + h_2^2(r_o) \right) \left(\frac{R_0^2}{2} \left(\frac{1}{h_2^2(r_o)} - \frac{1}{h_2^2(r_i)} \right) + \ln \left(\frac{h_2(r_o)}{h_2(r_i)} \right) \right) = 0. \tag{G.97}$$

Utilizing $h_2^2 = r^2 - R_0^2$

$$\frac{R_0^2}{2} \left(\frac{1}{r_o^2 - R_0^2} - \frac{1}{r_i^2 - R_0^2} \right) + \frac{1}{2} \ln \left(\frac{r_o^2 - R_0^2}{r_i^2 - R_0^2} \right) = 0. \tag{G.98}$$

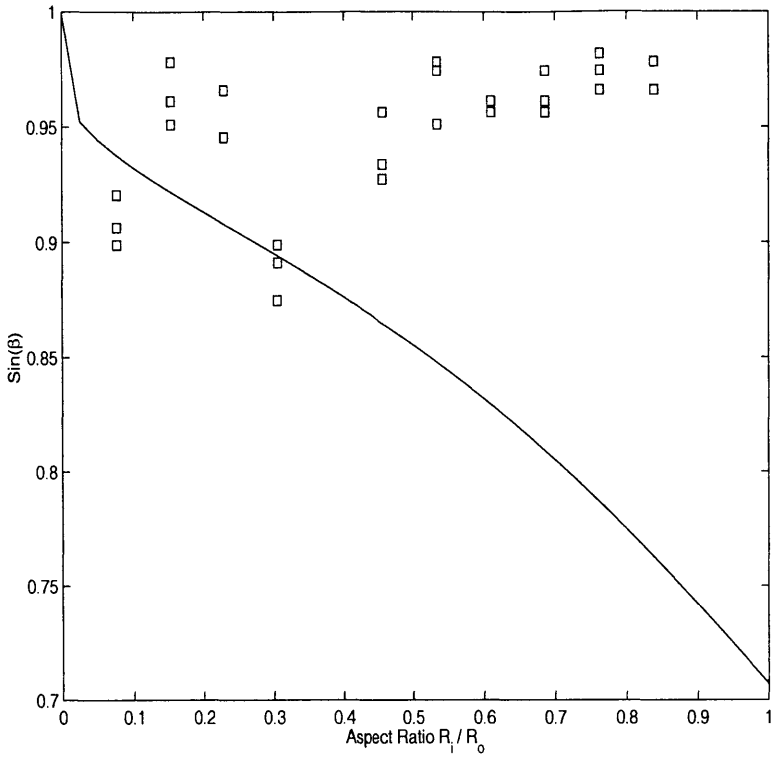

Figure G-5: Tension field theory results

Define $\rho \equiv r_i/r_o$ and $\alpha \equiv \sin\beta$, so $R_0 = r_i\alpha$.

$$\frac{\alpha^2}{1-\alpha^2}\left(1 - \frac{1-\alpha^2}{\frac{1}{\rho^2}-\alpha^2}\right) + \ln\left(\frac{1-\alpha^2}{\frac{1}{\rho^2}-\alpha^2}\right) = 0, \tag{G.99}$$

so $\beta = f(r_i/r_o)$. (G.99) can be solved numerically (in this case using Matlab's zero-finding routine). The results of such a solution are plotted if Figure G-5.

One might expect that in the experiments described in Chapter 3, far from onset, the wrinkles in the viscous sheet might have the arrangement predicted by tension field theory. If this were to be the case, we would expect the crests of the wrinkles to follow tension lines because the primary direction of buckling would always be along the direction of the principal compressive stress which is normal to the tension lines everywhere. The squares in Figure G-5 show the angles at which the wrinkles in the experiments emanate from the inner cylinder. There does not appear to be any correlation between the results of tension field theory and our experiments. This suggests that even at saturation in our experiments, tensile stresses do not play the sole important role in determining the behavior of the sheet.

The Bernoulli spiral provides an alternative promising candidate for the shape of the ripples at saturation. The Bernoulli spiral ($r = e^{\theta}$) intersects radial lines at the same angle everywhere. In an isotropic medium, the principal stress axes and the principal strain axes correspond to Bernoulli spirals with winding angles of $\pi/4$

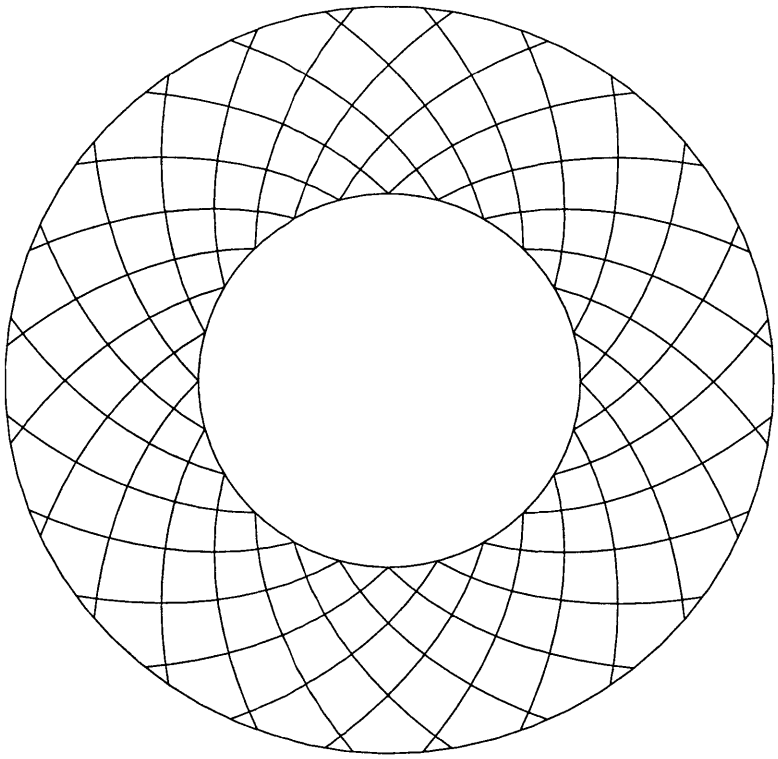

Figure G-6: Isotropic medium principal axes: Bernoulli spirals

(Figure G-6). In our experiments, the wrinkles are well matched by Bernoulli spirals with varying winding angles. For example, for an inner radius of 1" and an outer radius of 3.28", Figure G-8 shows the shapes of the experimentally recorded ripples as solid lines and the Bernoulli spirals as dashed lines with '+' signs.

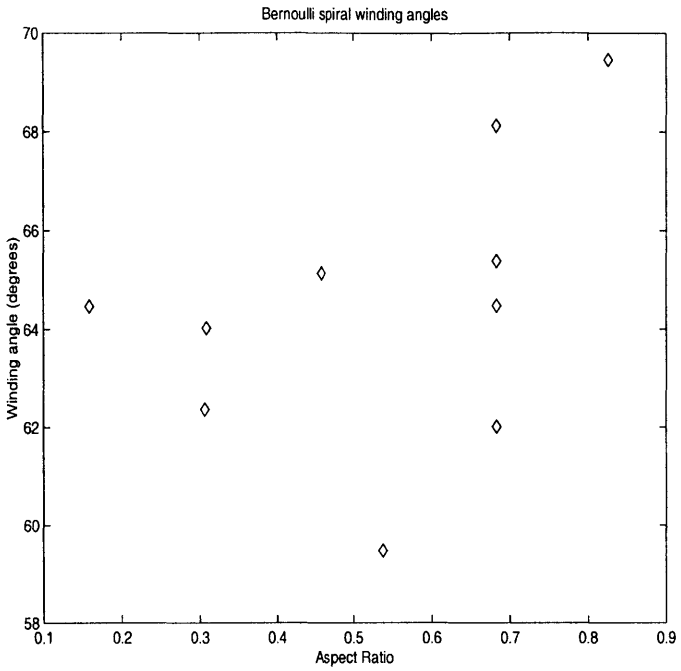

Figure G-7: Bernoulli spiral winding angles in experiments

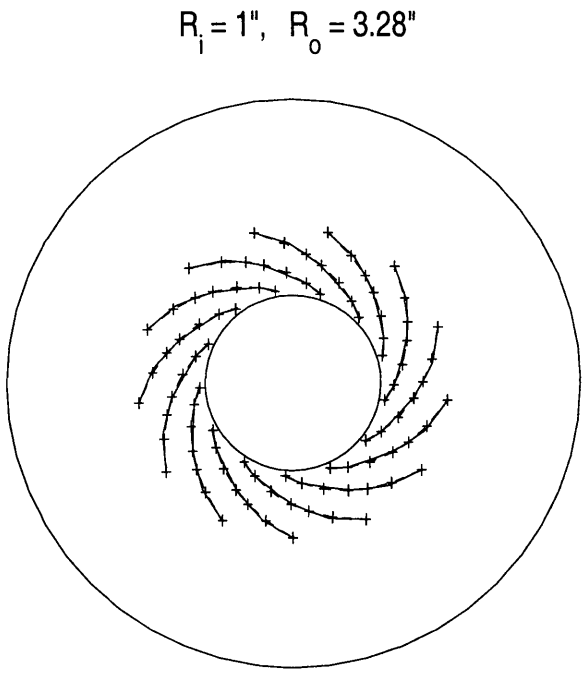

Figure G-8: Bernoulli spirals fit to experimentally measured ripples using Matlab to obtain a least squares fit. Solid lines are experimental ripples. Dashed lines with '+' signs are Bernoulli spirals.

Bibliography

[1] Arthur W. Adamson. *Physical Chemistry of Surfaces.* John Wiley & Sons, Inc., third edition, 1976. pp. 106-107.

[2] Adrian Bejan. Buckling flows: A new frontier in fluid mechanics. *Annual Review of Numerical Fluid Mechanics and Heat Transfer*, pages 262–304, 1987.

[3] T.B. Benjamin and T. Mullin. Buckling instabilities in layers of viscous liquid subjected to shearing. *Journal of Fluid Mechanics*, 195:523–540, 1988.

[4] M. A. Biot. Folding instability of a layered viscoelastic medium under compression. *Proceedings of the Royal Society, Series A*, 242(1231):444–454, 1957.

[5] M. A. Biot. The influence of gravity on the folding of a layered viscoelastic medium under compression. *Journal of the Franklin Institute*, 267(3):211–228, March 1959.

[6] M. A. Biot. Theory of folding of stratified viscoelastic media and its implications in tectonics and orogenesis. *Geological Society of America Bulletin*, 72(11):1595–1620, November 1961.

[7] J.D. Buckmaster and A. Nachman. The buckling and stretching of a viscida II. Effects of surface tension. *Quarterly Journal of Applied Mathematics*, XXXI(2):157–168, 1978.

[8] J.D. Buckmaster, A. Nachman, and L. Ting. The buckling and stretching of a viscida. *Journal of Fluid Mechanics*, 69:1–20, 1975.

[9] William M. Chapple. A mathematical theory of finite-amplitude rock-folding. *Geological Society of America Bulletin*, 79:47–68, 1968.

[10] S. Crandall, N. Dahl, and T. Lardner. *An Introduction to the Mechanics of Solids.* McGraw-Hill Book Company, Inc., 2nd edition with SI units edition, 1999. pp. 220,221,285.

[11] W.R. Dean. The elastic stability of an annular plate. *Proceedings of the Royal Society, Series A*, 106:268–284, 1924.

[12] P.D. Howell. Models for thin viscous sheets. *European Journal of Applied Mathematics*, 7:321–343, 1996.

[13] H. Max Irvine. *Cable Structures.* MIT Press, Cambridge, Massachusetts, 1981. p. 1.

[14] Arvid M. Johnson and Raymond C. Fletcher. *Folding of Viscous Layers.* Columbia University Press, 1994.

[15] Arun K. Kumar and Michael D. Graham. Buckling instabilities in models of viscoelastic free surface flows. *Journal of Non-Newtonian Fluid Mechanics*, 89(3):337–351, March 2000.

[16] James Lighthill. *Waves in Fluids.* Cambridge University Press, Cambridge, England, 1978. Ch. 3.

[17] A.E.H. Love. *A Treatise on the Mathematical Theory of Elasticity.* Dover, 4th edition, 1944. sections 273A,329,335E.

[18] L. Mahadevan, W.S. Ryu, and A.D.T. Samuel. Fluid 'rope trick' investigated. *Nature*, 392:140, March 1998. Addendum and correction, 2000.

[19] James Clerk Maxwell. *Theory of Heat.* Greenwood Press, third edition, 1970. p. 276.

[20] John J. O'Conner and Edmund F. Robertson. The MacTutor History of Mathematics Archive: Catenary. http://www-history.mcs.st-andrews.ac.uk/history/Curves/Catenary.html, School of Mathematics and Statistics, University of St. Andrews Scotland, January 1997. (May 2002).

[21] Hans Ramberg. Fluid dynamics of viscous buckling applicable to folding of layered rocks. *Bulletin of the American Association of Petroleum Geologists*, 47(3):484–505, March 1963.

[22] Hans Ramberg and Ove Stephansson. Compression of floating elastic and viscous plates affected by gravity, a basis for discussing crustal buckling. *Tectonophysics*, 1:101–120, 1964.

[23] Eric Reissner. On tension field theory. In *Proceedings of the 5th International Congress of Applied Mechanics*, pages 88–92, 1938.

[24] N. M. Ribe. Bending and stretching of thin viscous sheets. *Journal of Fluid Mechanics*, 433:135–160, 2001.

[25] Jo-Ann Sherwin and W. M. Chapple. Wavelengths of single layer folds: A comparison between theory and observation. *American Journal of Science*, 266(3):167–179, March 1968.

[26] R. Silveira, S. Chaieb, and L. Mahadevan. Rippling instability of a collapsing bubble. *Science*, 287:1468–1471, February 2000.

[27] M. Skorobogatiy and L. Mahadevan. Folding of viscous sheets and filaments. *Europhysics Letters*, 52:532, 2000.

[28] R.V. Southwell and Sylvia W. Skan. On the stability under shearing forces of a flat elastic strip. *Proceedings of the Royal Society, Series A*, 105(733):582–607, 1924.

[29] J.W. (Lord Rayleigh) Strutt. *Theory of Sound*, volume II. Dover Publications, 1945. pp. 313-314.

[30] G.I. Taylor. Instability of jets, threads, and sheets of viscous fluid. In *Proceedings of the 12th International Congress of Applied Mechanics*, pages 382–388. Springer-Verlag, 1969.

[31] S. Timoshenko and S. Woinowsky-Krieger. *Theory of Plates and Shells.* McGraw-Hill Book Company, Inc., 2nd edition, 1959. pp. 5,378.

[32] Lloyd N. Trefethen. *Spectral Methods in MATLAB.* Society for Industrial and Applied Mathematics, 2000.

[33] Fred T. Trouton. On the coefficient of viscous traction and its relation to that of viscosity. *Proceedings of the Royal Society, Series A*, 77(519):426–440, 1906.

[34] E.O. Tuck, Y.M. Stokes, and L.W. Schwartz. Slow slumping of a very viscous liquid bridge. *Journal of Engineering Mathematics*, 32:27–40, 1997.

[35] Stokes Y.M., E.O. Tuck, and L.W. Schwartz. Extensional fall of a very viscous fluid drop. *Q. J. Mech. Appl. Math.*, 53(4):565–582, 2000.

Biographical note

The author grew up in Silver Spring, Maryland with his parents, Bob and Lois, and his brother, Daniel. He attended the Hebrew Academy of Greater Washington from elementary school until the end of eleventh grade when he left without graduating to attend Yale University in New Haven, Connecticut in September of 1992. During his four years at Yale, he double-majored in Mechanical Engineering and Computer Science and dabbled in philosophy. In his junior year, he was inducted into Tau Beta Pi, the engineering honor society. Upon graduation from Yale in May of 1996 with a Bachelor of Science, he received the Becton Prize and the American Society of Mechanical Engineers award for the most outstanding graduate in Yale's Mechanical Engineering Department. While in high school and college, he worked summers as a computer programmer at the Naval Surface Warfare Center in White Oak, Maryland, as a mechanical engineering research intern at the Institute for Systems Research at the University of Maryland, College Park, and as a research and development team member at Enig Associates, Incorporated, a small military contractor. In the fall of 1996, he relocated to Cambridge, Massachusetts to begin his graduate work in the Fluid Mechanics Laboratory at the Massachusetts Institute of Technology sponsored by a National Science Foundation Graduate Fellowship. He completed his Master's degree working with Professor Anthony Patera on theory of the finite element method in June of 1998 and continued with doctoral work on the subject through the summer of 1999. In July of 1999, he moved within the Fluid Mechanics Laboratory to the research group of Professor L. Mahadevan and commenced this thesis work. After receiving his Ph.D. in June of 2002, he plans to work in industry as an engineering consultant.